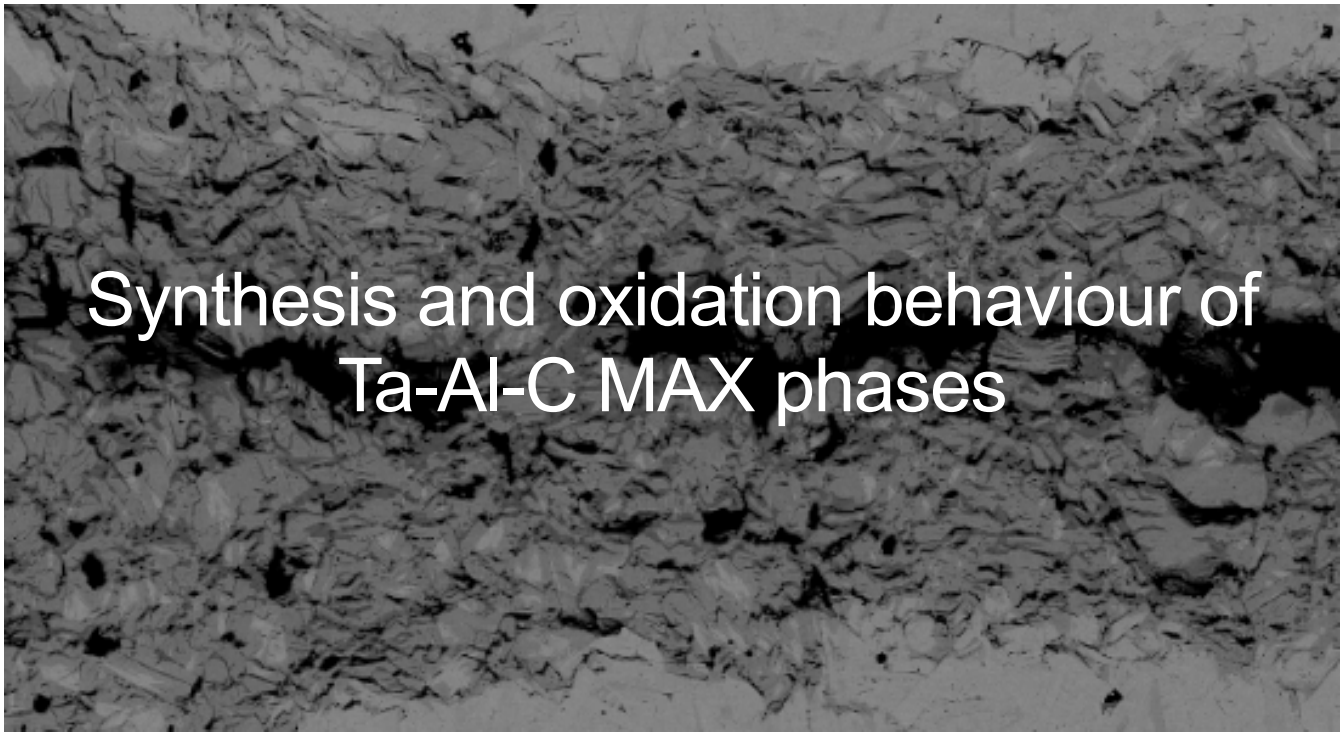

Synthesis and oxidation behaviour of Ta-Al-C MAX phases

Master of Science Thesis

Julia Stikkelman

18/07/2016

MSc Material Science and Engineering

Supervisor:	Dr. Ir. W. G. Sloof	TU Delft
Thesis committee:	Dr. Ir. J.M.C. Mol	TU Delft
	M.Eng. A.M. Farle (daily supervisor)	TU Delft

Department of Material Science and Engineering
Faculty of Mechanical, Maritime and Materials Engineering
Delft University of Technology

TU Delft

Abstract

MAX-phase materials, a class of ternary carbides and nitrides that combine favorable properties of metals (conductivity and toughness) and ceramics (high temperature strength) have been shown to autonomously heal micro-cracks by high temperature oxidation. The investigation of Ta and Al containing MAX phases (Ta_2AlC & Ta_4AlC_3) could render self-healing materials at lower temperatures. Mixed (Ta_2AlC and Ta_4AlC_3) and pure dense bulk Ta_2AlC MAX phase was synthesized by spark plasma sintering (SPS) of elemental powders. The oxidation reactions of Ta-Al-C MAX phase powders were studied with differential thermal analysis (DTA). The oxidation kinetics of dense bulk Ta-Al-C MAX phase was studied by thermal gravimetric analysis (TGA). The microstructure and composition of the MAX phase materials and its oxides was characterized by X-ray diffractometry (XRD), scanning electron microscopy (SEM) with energy dispersive spectroscopy (EDS), X-ray microanalysis with electron probe microanalysis (EPMA), and X-ray photoelectron spectroscopy (XPS).

Linear oxidation kinetics, inward oxide growth and formation of mainly porous Ta-oxides were observed for isothermal oxidation of dense bulk Ta_2AlC and mixed MAX phase. Based on the results obtained in this work, the oxides scales formed in the 600 – 800 °C temperature range are believed to consist of various metastable and/or amorphous oxides. Full oxidation of the MAX phase above 900 °C results in the formation of Ta_2O_5 and ternary $TaAlO_4$. It was found that Ta-Al-C MAX phases cannot self-heal microcracks by formation of a protective oxide scale at elevated temperatures.

Key words: Ta_2AlC, Ta_4AlC_3, MAX phase, synthesis, oxidation, self-healing

Acknowledgements

I would like to thank Wim Sloof for being my supervisor throughout this thesis project, for his insight, general help, and for allowing me to make use of the equipment in the laboratory of the Surface and Interface Engineering group of the Material Science and Engineering department. It has made this work possible. A big thanks to Ann-Sophie Farle, who has been my daily supervisor, and showed great support in helping me to get experiments started, providing advice, and giving feedback to my work. Furthermore, I am very thankful to Kees Kwakernaak, Hans Brouwer, Ruud Hendrikx, Niek van der Pers, and Richard Huizenga for everything they have contributed to this work, by performing various measurements for me, the interesting discussions I have had with them on the interpretation of results, and keeping things running smoothly in the laboratory. I would like to thank Arjan Mol for being part of the thesis committee. I would like to thank the PhD's, fellow MSc students, and some staff members of the Material Science department for their companionship, pep talks, and good times.

I'm very grateful for the presence of some of my friends and family who have provided me with support in various ways throughout this project. And Wessel, I am happy to be with you.

List of Abbreviations

CTE	coefficient of thermal expansion
DC	direct current
DTA	differential thermal analysis
EDS	energy dispersive spectroscopy
EPMA	electron probe microanalysis
HIP	hot isostatic press
HP	hot press
MA	mechanical alloying
PBR	Pilling-Bedworth ratio
PLS	pressure-less sintering
PSHS	pressured-assisted self-propagating high-temperature synthesis
RVE	relative volume expansion
SEM	scanning electron microscopy
SH	self-healing
SHS	self-propagating high-temperature synthesis
SPS	spark plasma sintering
TEM	transmission electron microscopy
TGA	thermo-gravimetric analysis
TMD	theoretical maximum density
VH	Vickers hardness
WDS	wavelength dispersive spectrometry
XPS	X-ray photo-electron Spectroscopy
XRD	X-ray diffraction

Table of Contents

1. Introduction

The interest in self-healing structural materials has strongly grown in the recent past, as can be seen from the vast increase of scientific publications on the topic, for a wide variety of materials. Self-healing materials provide an alternative way to cope with the ever hasher environments in which structural materials have to function during their desired lifetime [1]. If a structural material possesses the ability to self-heal microcracks that form during operation, mechanical failure due to further growth of these microcracks can be avoided.

The world energy demand is expected to continue to rise in the near future, while scarcity of traditional sources is looming. One approach to increase the lifetime of traditional energy sources such as natural gas and oil is to change the conditions during energy generation such that the process can be more efficient. An example is to increase the temperature within the combustion chamber of an internal combustion engine, which increases the energy efficiency while decreasing CO_2 emissions. In order to achieve this in a safe and sustainable manner, all structural components within the combustion chamber must be able to withstand higher temperatures during operation during a prolonged period of time, without failure. Another scenario is the use of sustainable energy sources, which bring on their own challenges as energy generation from sustainable sources often has to take place in remote areas, where maintenance is costly and difficult [2]. Hence, all materials used for the equipment must have a sufficiently long lifetime to allow profitable operation. These demanding material requirements have often made improvements or new solutions unfeasible. The possibility to use materials with self-healing capabilities – often required at elevated process temperatures – could be a piece of the big puzzle that needs to be completed to solve these problems.

One family of materials that is currently investigated because some members are likely to have self-healing capabilities at elevated temperatures, is the so called 'MAX phase family'. $M_{n+1}AX_n$ phase ceramics are layered ternary carbides or nitrides, where the M denotes a transition metal, the A denotes an A-group element from the periodic table, and X stands for carbon or nitrogen [3]. Over 70 different MAX phases have yet been reported [4]. Its unique layered crystallographic structure of alternating layers of carbide/nitride and monatomic metallic A-elements renders a unique combination of metallic and ceramic properties [5]. Additionally, two MAX phases – Ti_2AlC and Cr_2AlC – have been shown to form protective oxides upon oxidation at elevated temperatures, which can fill microcracks. Farle *et al.* [6] has recently investigated the self-healing potential of the other members of the MAX phase family, based on six criteria (described in section 2.3). Ta_2AlC MAX phase was identified as a potential candidate for self-healing.

The goal of this work is to 1) find a synthesis route to synthesize dense bulk predominantly single-phase Ta_2AlC MAX phase, and 2) analyse its oxidation behaviour to find out if it indeed has self-healing potential. For analysis of the oxidation behaviour of Ta-Al-C MAX phase, the following questions are of interest: what oxidation products form, and what does its microstructure look like? What is the oxidation mechanism? Are the oxides protective? What kind of oxidation kinetics takes place? By answering these questions, the potential self-healing behaviour can be verified. Successful synthesis and a successful oxidation study also provide the means to design an experiment to test self-healing behaviour.

In Chapter 2, a theoretical background on the general topic of self-healing, and on MAX phases and self-healing in MAX phases is given. In addition, a literature review of synthesis of MAX phases, MAX phase properties, and oxidation behaviour of Ta_2AlC, Ta, TaC and Ta_2C is provided. In Chapter 3 all methods used for this work are described, and an overview of the relevant experimental details is given. In Chapter 4 the results of the synthesis, oxidation, and crack-healing experiments are given, and a discussion of these results can be found in Chapter 5. Finally, the conclusions and recommendations based on the research conducted for this work are given in Chapter 6.

2. Theoretical Background

2.1 Relevance & concept of self-healing in structural materials

In industry and science, the demand for stronger materials is mainly met by the focus on development of materials with microstructures that prevent the formation or extension of micro-cracks. Currently, industries are facing many challenges because the requirements for materials to be used become ever higher, due to more extreme process conditions and environments, such as high temperatures or remote locations [1]. 'Classical structural materials' might not always be able to meet these requirements. In this light, several societal needs have been identified by van der Zwaag [1], which are expected to drive the development of materials which are able to 'manage damage' by self-healing, in the near future. These societal needs include the fact that industrial installations more often make use of components which are very costly to repair, but need to be very reliable at the same time, such as for example in off-shore energy facilities. Also there are capital intensive applications which are required to have a relatively long lifetime (> 40 years), like highways and tunnels. Furthermore, certain applications require an extremely high reliability, such as aircrafts, as failure would be at the expense of lives. Lastly, for many products (cars, planes, etc.) a high surface quality during the entire time of use is required or desired.

The concept of self-healing in structural materials can be illustrated by comparing the schematic diagrams of damage development in Figure 1 and Figure 2. Damage development in three different classical structural materials, A, B, and C versus load or time is shown in Figure 1. Material A represents the reference material to be improved. The damage keeps increasing until it reaches the damage level '1' at which point it fails. Material B is an improvement from material A as it starts to form damage at a higher load/after a longer time. However, once damage formation starts, the damage level increases much more quickly until failure. For practical purposes material B could be a drawback because the increase of damage until failure cannot be monitored easily as it happens very fast. Material C represents the best classically engineered option, based on the premise of damage prevention; damage formation starts substantially later (at a higher load), and further damage increase happens at a slower rate, compared to material A and B.

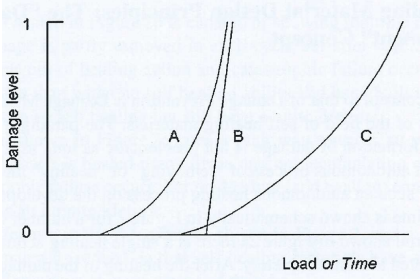

Figure 1: "Schematic diagram of the damage level in classical materials as a function of time or applied load" [1].

The schematic damage development in three grades of self-healing materials, with increasing self-healing capabilities is shown in Figure 2a to c. The essential difference between a classical

structural material and a self-healing structural material, is the ability of the latter to reduce its damage level. Figure 2a shows only one healing cycle; i.e. damage forms, increases, and after a certain time starts to decrease until a certain damage level, after which it increases again until ultimate failure. Figure 2b shows improvement with multiple healing cycles, but eventually the material still fails due to the damage. Only the self-healing material shown in Figure 2c represents the ideal situation, with an infinite amount of healing cycles, such that failure never takes place after damage formation.

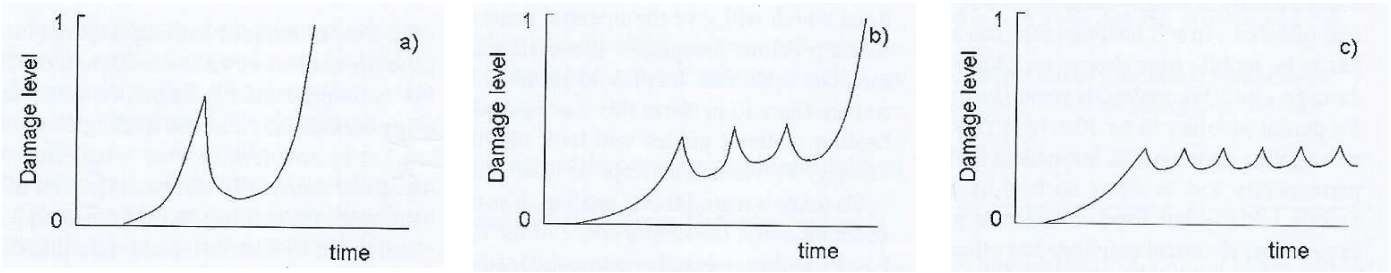

Figure 2: "Schematic diagram of the damage development in three grades of self-healing materials" [1], for a) a self-healing material with one healing cycle, b) multiple healing cycles, c) an infinite amount of healing cycles.

First and foremost, the self-healing material must be able to perform to the standards of a classical structural material for a certain mechanical function. On an atomistic level this means that chemical bonds and atom density need to provide for the right mechanical properties (strength, stiffness, etc.). Furthermore, in addition to a classical structural material, a self-healing material should sense and repair damage, like microcracks or micro voids. This means that formation of microcracks should initiate mobile atoms or a healing agent to 'flow' towards the crack and rearrange themselves in such a way that crack filling and mechanical repair can take place.

Van der Zwaag [1] mentions two additional criteria for successful self-healing, which are related to external factors. For most cases a reduction of externally applied load is necessary, in order to allow crack healing to take place. On that notion, self-healing seems most suitable for situations in which cyclic loading takes place. Furthermore, the two crack surfaces should not be too far apart, and hence self-healing works best for partial cracks (e.g. two sides of the crack are held together by a non-cracked part in front of the crack tip).

In recent years a strong increase of research on self-healing has taken place in all material classes – polymers, ceramics, metals –, and it has been shown that there are many different mechanisms by which self-healing can take place. For polymers, different chemical routes have been researched, such as; fracture and reformation of the molecular chain or intermolecular bonds [7]; self-organizing polymers based on non-covalent hydrogen-bond interactions [8]; thermosetting epoxy with dissolved linear polymer chains which can 'meander' towards cracks to fill them [9]. In metals, it has been shown that the addition of certain solid solution elements can favour dynamic precipitation within microcracks, voids, and grain boundary cavities, at elevated temperatures. An example is the addition of alloying elements gold and copper to steel [10, 11]. For ceramics, self-healing is to be achieved by the formation of protective oxides, like Al_2O_3, SiO_2, and Cr_2O_3, to fill up microcracks [12]. A distinction between intrinsic and extrinsic self-healing materials can be made. For ceramics, in the case of extrinsic self-healing, micro capsules with a healing agent are incorporated in the ceramic matrix. Upon the formation of microcracks, the

healing agent ‘flows’ out of the capsule and into the crack, where it oxidizes and fills it. An example is the use of Al_2O_3/SiC composites at elevated temperatures; SiC particles are encapsulated in alumina, and when a microcrack reaches a SiC particle, SiC reacts with O_2 to form protective SiO_2 which fills the microcrack [13]. In the case of intrinsic self-healing ceramics, the addition of microcapsules with healing agent is not required, but instead microcracks can be filled by oxidation of the original matrix material [14]. Some types of MAX phase ceramics have already been shown to fall in this category [15, 16].

2.2 Introduction to MAX phases

The name ‘MAX phase’ was given to a family of ternary carbides and nitrides [3], in reference to its formula, $M_{n+1}AX_n$, where M strands for ‘transition metal, A is an A-group element (mainly group IIIA and VIA), and X stands for carbon or nitrogen. ‘n’ only takes the value of integer numbers, and has been reported to go up to 6 [17, 18]. All M, A, and X elements are highlighted in the periodic table in Figure 3; over 70 different combinations of these elements are known to form different MAX phases [5].

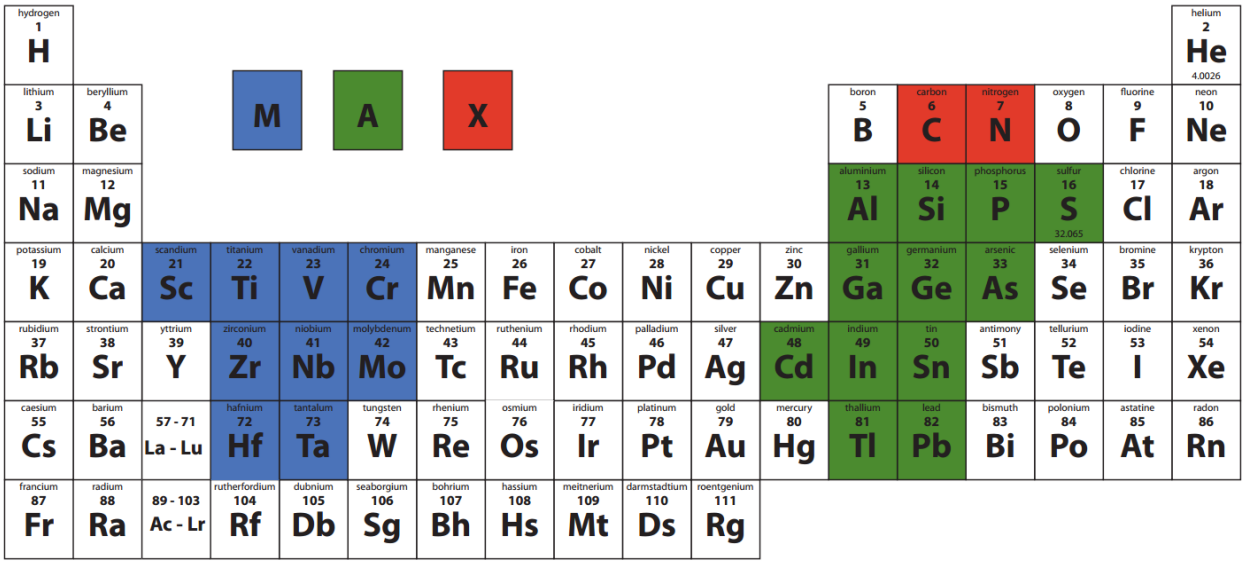

Figure 3: Periodic table with M-, A-, and X-elements highlighted [6].

Resulting from its characteristic stoichiometry, it is the layered hexagonal crystal structure and chemical bonding that give MAX phases their unique combination of properties. MAX phases can be described as nanolaminates consisting of layers of MX binary carbides or nitrides, alternating with monatomic layers of pure A-elements. Depending on the value of ‘n’, the A-element layers are separated by 2 (n=1) to 6 (n=5) M-layers. Carbon or nitrogen (X-elements) are located between the M-atoms, at the octahedral sites of the MX structure. A schematic of the alternating MX and A layers, and the crystal structure for different ‘n’ values is shown in Figure 4 [19].

In multiple works, density functional theory (DFT) approaches are used to characterize the chemical bonding types in MAX phases [20-26]. It was shown that chemical bonding between the M- and X-elements is relatively strong, mainly covalent and strongly directional, while the bonding

between M- and A-elements is weaker for most MAX phases. Overall, "*MAX phase bonding is a combination of metallic, covalent, and ionic bonds*" [3], p.3.

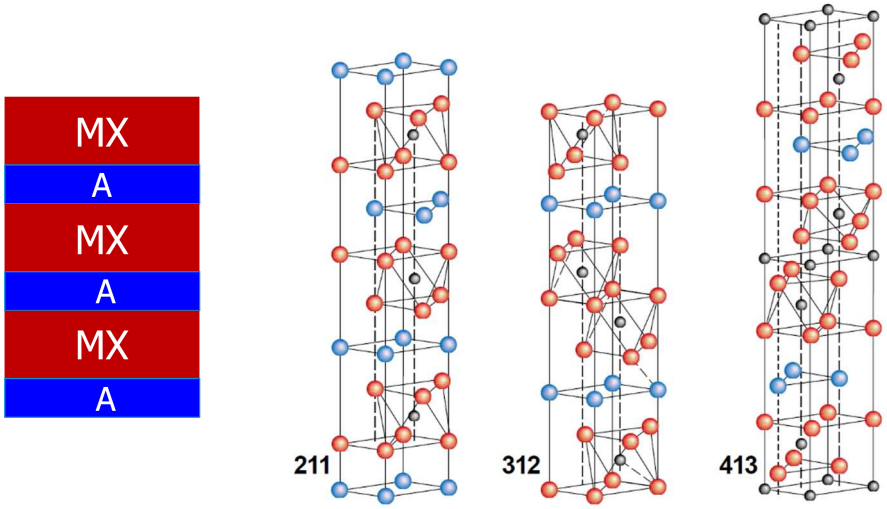

Figure 4: Schematic of alternating MX and A layers, and schematic of the hexagonal layered crystal structure of MAX phases for n = 1, 2, 3 [19].

It is the combination of very strong M-X bonds with relatively weak M-A bonds – each with a different bonding type –, incorporated within the layered hexagonal crystal structure, that give MAX phases their unique mix of typical ceramic as well as metallic properties. Like ceramic binary carbides and nitrides, MAX phases are elastically stiff, have a high melting point, and low thermal expansion coefficients. Some members of the MAX phase family are also relatively resistant to creep, corrosion, and to chemical attack in general [5]. However, like metals, they also have good thermal and electrical conductivity, a high thermal shock resistivity and damage tolerance, and are relatively soft and easy to machine [5].

The values of some material properties, that are known from research on MAX phases are summarized in Table 2Table 1.

Table 1: Several material properties of MAX phases and their value range, as stated by Radovic et al.[3].

Material property	Value range	Additional remarks
Electrical resistivity	0.2 – 0.7 μΩ·m at T_{room} [27, 28]	For most MAX phases; Increases with increasing temperature
Thermal conductivity	12 – 60 W/(m·K) at T_{room} [29]	
CTE	5 – 10 μK^{-1} [3]	Some exceptions in 12 – 14 μK^{-1} range
Young's modulus	178 – 362 GPa at T_{room} [30, 31]	Near-isotropic
Shear modulus	80 – 142 GPa at T_{room} [30, 31]	Near isotropic
Ultimate compressive strength	300 MPa – 2GPa at T_{room} [30-32]	depends strongly on composition and grain size; flexural & tensile strength < compressive strength
Vickers hardness	2 – 8 GPa [32]	For polycrystalline MAX phases
Fracture toughness	5 – 20 $MPa \cdot m^{1/2}$ at T_{room} [3]	R-curve behaviour
Brittle to plastic transition temperature (BPT)	1000 – 1100 C [33]	For most MAX phases

The relatively ductile behaviour of MAX phases is explained further by Radovic *et al.* [3] to originate from mobile dislocations in the basal planes of the hexagonal structure, which allows plastic deformation. When a high enough external load is applied, initially only the grains with a favourable orientation of their basal planes for easy slip deform. This causes incipient kink bands (IKB) to form in grains with other orientations towards external loading, which are spontaneous and still fully reversible. In case loading continues, the IKB's facilitate the formation of mobile dislocation walls (MDW), which ultimately results in permanent kink bands (KB). It is these KB's which eventually lead to delamination of the MAX phase at a microscale, and allow for considerable plastic deformation. Examples of the typical nanolayered MAX phase microstructure with kink bands and delamination are shown in Figure 5.

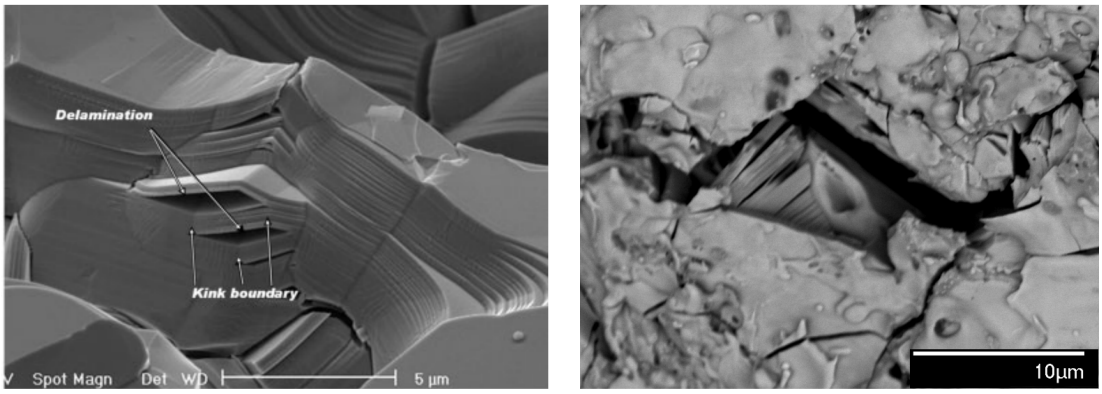

(a) (b)

Figure 5: Examples of a typical MAX phase nanolayerd microstructure, a) fracture surface of Ti_3SiC_2, including kink boundaries and delamination [31],b) side-view of microcrack (SEM backscatter) in mixed Ta_2AlC and Ta_4AlC_3 (this work).

The unique combination of metallic and ceramic properties makes MAX phases very interesting for future application in (cyclic) high temperature and/or electrical applications, where for example a combination of high temperature stability, fatigue resistance, good electrical conductivity, and non-brittle behaviour is desired [5]. As well as machinability, because for many applications complex shapes are required. In addition to all properties mentioned, some members of the MAX phase family have shown potential for intrinsic autonomous self-healing at high temperature [6].

2.3 Self-healing in MAX phases at elevated temperatures

In 2008 Song *et al.* [34] reported oxidation-induced crack healing in Ti_3AlC_2 MAX phase ceramics. After oxidation of a partially pre-cracked bulk Ti_3AlC_2 sample in air for 2 hours at 1100 °C, the crack – about 7 μm long, and with an average width of 5 μm – was found to be completely filled with primarily α-Al_2O_3 and some additional rutile (TiO_2). The hardness and indentation modulus of the crack-healed zone were found to be even slightly higher than that of the bulk Ti_3AlC_2. Reasons stated for the good strength recovery after healing are the fact that the coefficient of thermal expansion (CTE) of Ti_3AlC_2, α-Al_2O_3, and TiO_2 do not differ much (so only small misfit stresses arise after cooling), and that both oxide products adhere well to bulk Ti_3AlC_2. The oxidation mechanism of Ti_3AlC_2 was reported to be preferential oxidation of aluminium, due to relatively easy diffusion of Al atoms along the grain boundaries of the grains on the crack surface. The following reaction is proposed for the formation of protective α-Al_2O_3 [35]:

$$Ti_3AlC_2 + \frac{3}{2}\,y \cdot O_2 \rightarrow Ti_3Al_{1-y}C_2 + \frac{1}{2}\,y \cdot Al_2O_3$$

Further research into the early stages of oxidation of bulk Ti_3AlC_2 MAX phase showed that in the first few minutes nanosized α-Al_2O_3 oxide nuclei start to form, predominantly on the ledges of the fracture surface of the lamellar Ti_3AlC_2 [36] (see Figure 6). After further oxidation these nuclei also grow over the 0001 basal plane terraces to form a continuous initial α-Al_2O_3 oxide scale. After initial oxidation, thickening of the oxide scale takes place in the inward as well as outward direction. Further oxidation caused by inward diffusion of oxygen via grain boundaries in the Al_2O_3 scale, consumes more of the original bulk Ti_3AlC_2 inwards [35]. At the same time Ti atoms diffuse outward through the oxide scale to form TiO_2 on the surface of the α-Al_2O_3 oxide scale. Underneath the α-Al_2O_3 oxide scale, a porous layer can form, in case the formation of Al_2O_3 does not compensate the volume of Ti_3AlC_2 that is lost due to oxidation [36]. Wang *et al.* reports on slight relaxation of the Ti_3AlC_2 structure right beneath the oxide scale, due to the formation of Al vacancies [35]. With increasing oxidation, the oxide scale grows thicker, and this is stated to cause sub-parabolic oxidation kinetics.

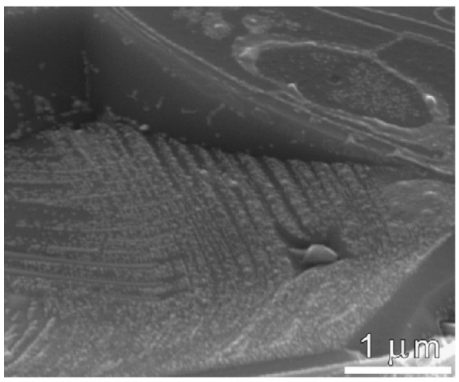

Figure 6: Fracture surface of Ti_3AlC_2 oxidized at 1100 °C for 60 seconds [36].

Multiple crack healing was reported for the first time in another member of the Ti-Al-C MAX phase system – Ti_2AlC – by Li *et al.* [15]. Seven healing cycles were achieved with dense bulk predominantly single-phased Ti_2AlC (minor Ti_3AlC_2 and $Ti_{1.25}Al_{2.75}$ impurities). Initial cracks were produced by Knoop indentation in combination with fatigue cycling. Re-cracking after each healing cycle was achieved by bending. For each healing cycle, Ti_2AlC was oxidized in air for 2 hours at 1200 °C. The flexural strength in the healed zone of 152-224 MPa was measured to slightly exceed the initial strength of 211 MPa [15], which might be due to the 'healing' of porosities in the virginal material. The fracture toughness recovery was measured to be in the range of 3-6.7 MPa $\cdot$ $m^{1/2}$. The same oxidation products were found as for Ti_3AlC_2; well-adhering α-Al_2O_3, and rutile TiO_2.

Very recently self-healing in fine-grained bulk Cr_2AlC was investigated for oxidation in the range of 900 – 1200 °C, and holding times of maximal 100 hours [37]. Cr_2AlC was found to show good healing behaviour due to the formation of a dense, thin, and well-adhering oxide scale of predominantly α-Al_2O_3. Cracks with an opening between 0.1 and 2 µm, and a length between 0.3 and 2.5 µm were filled completely with α-Al_2O_3 oxide. Strength recovery after healing was quantified via three-point bending tests, and was shown to be a function of healing time and initial crack length. The higher the initial crack length, the lower the residual strength. The longer the healing time, the higher the recovered strength after healing. In case of a very small initial crack, the healed sample might even have a higher strength than the un-cracked virgin sample. The composition of the oxides that form within the crack zone were shown to change over time; initially a mix of Cr_2AlC, α-Al_2O_3, and $(Cr,Al)_2O_3$ was found, and for longer oxidation times only α-Al_2O_3 remains.

Yang *et al.* has examined oxide scale growth on the surface of dense bulk predominantly single-phased Cr_2AlC after repeated annealing at 1100 °C [16]. It was concluded that further growth of oxide scale during repeated annealing is dominated by outward diffusion of Al ions via grain boundaries of the columnar grains within the prior oxide scale. The diffusion flux of Al ions is inversely proportional to the oxide scale thickness, and hence the healing rate becomes lower if the oxide scale becomes thicker. Cracks with a very small width are therefore desirable, as a thinner columnar oxide scale is required to form to fill the crack, and healing happens much faster.

Criteria for self-healing in MAX phases

Apart from the Ti-Al-C and Cr-Al-C system, crack healing in other MAX phases has not yet been reported. In order to identify similar intrinsic autonomous self-healing potential in other members of the MAX phase family, Farle *et al.* [6] have postulated four primary, and two secondary general criteria for high temperature self-healing in MAX phases, which are discussed below. The primary criteria are first discussed (1-4), and the secondary criteria are discussed after (5 and 6).

1. Based on the oxidation mechanism that causes crack healing in Ti-Al-C and Cr-Al-C MAX phases, preferential oxidation of the A-element is desired. Comparing the Gibbs free energy of formation ΔG° of the M- and A-oxides is proposed as means to predict selective A-oxidation. The element with the most negative ΔG° of oxide formation forms the most thermodynamically stable oxide, and hence "*may be selectively oxidized*" [6]. It is proposed to select MAX phase systems in which A-oxide formation is favoured. If the difference in ΔG° of oxide formation between the A- and M-element is small, different alternating oxides might be formed due to competing oxidation of both element, which could in turn also cause growth of ternary oxides. It should be noted that certain oxides only form at high temperatures, such as Al_2O_3 and TiO_2.

2. Apart from the thermodynamic requirement for preferential formation of the A-oxide, kinetics should be fast enough to allow healing of cracks within a reasonable time. During initial selective oxidation, the diffusion of the A-element trough the MAX phase matrix should be dominant. The diffusion rate should be reasonably high, as the oxidation kinetics of the formation of the initial oxide scale is determined by the flux of A-element that reaches the surface, after which it can react with oxygen. MAX phases generally have a higher mobility of the A-elements, as the M-A bonds are weak compared to the MX bonds. The atom mobility parallel and perpendicular to the basal plane was observed to be different. The anisotropy is assumed to be caused by the hexagonal layered structure. Not much experimental work on diffusion of M- and A- elements within MAX phases has been done. Therefore, Farle *et al.* only reports on the comparison of the diffusivity of M- and A-elements parallel to the basal plane, because this situation can be simplified by looking at the diffusion rates of M-element in their carbides versus the self-diffusivity of A-elements. After an initial oxide scale is formed, the oxidation kinetics could be governed by a different process; the diffusion rate of oxygen through the oxide scale towards the MAX phase surface. Furthermore, the oxidation kinetics are then dependent on the rate-limiting process of oxygen diffusion which is different depending on the type of oxide formed (protective versus non-protective).

3. In order for full healing of microcracks to take place, they should be completely filled with oxide. This only happens in case of sufficient volume expansion upon oxidation. If all constituents of the MAX phase oxidize, the general oxidation reaction and relative volume expansion (RVE) are:

$$\mathrm{M_{n+1}AX_n} \rightarrow \mathrm{M_{n+1}A_{1-x}X_n} + \mathrm{xAO_v}$$

$$\mathrm{RVE} = \frac{\mathrm{V_{M_{n+1}A_{1-x}X_n}} + \mathrm{xV_{AO_v}}}{\mathrm{V_{M_{n+1}AX_n}}} \approx 1 + \frac{\mathrm{xV_{AO_v}}}{\mathrm{V_{M_{n+1}AX_n}}}$$

For selective oxidation of the A-element, the reactions and RVE are:

$$M_{n+1}AX_n \rightarrow (n+1)MO_{v_M} + AO_{v_A} + nXO_{V_x}$$

$$RVE = \frac{(n+1)MO_{v_M} + V_{AO_{v_A}}}{V_{M_{n+1}AX_n}}$$

For good healing quality it is also important that the MAX phase remains stable close to the crack-zone, where it is depleted of A-element. For both cases (full- and selective oxidation) and for all MAX phases, RVE is greater than 1.

4. In addition to full crack filling, the formed oxide(s) should adhere well to the crack surfaces in order to restore the strength of the un-cracked MAX phase. This means that "*the energy required to separate the healing oxide from the MAX phase should be comparable or larger than the cohesion of the MAX phase*" [6] p. 5. This criterion is quantified by Farle *et al.* by the 'work of adhesion', which is defined as:

$$W_{ad} = -(\gamma_{MAX}^{surf} + \gamma_{oxide}^{surf}) + \gamma_{MAX/oxide}^{surf}$$

Where γ_{MAX}^{surf} and γ_{oxide}^{surf} are the surface energies of the MAX phase and the oxide, and $\gamma_{MAX/oxide}^{surf}$ is the interface energy. All can be calculated; the surface energies from the surface enthalpies, and the interaction energy from solution enthalpies. The calculation was made for several MAX phases for their A-oxides, and for all cases cohesion of the oxide is stronger than the cohesion of the MAX phase.

5. The thermal expansion coefficient (CTE) of the MAX phase and the oxide(s) in the crack should not differ too much, otherwise large thermal stresses would be induced in the healed zone when the temperature changes. This can cause formation of new cracks, especially in the case of tensile stresses in the oxide upon cooling ($CTE_{oxide} > CTE_{MAX}$).

6. The Young's modulus of the oxide should not be too high compared to that of the Young's modulus of the MAX phase, as this also induce stresses in the healed zone upon external loading. Generally, the oxides are stiffer than the MAX phase, i.e. have a higher Young's modulus. A relative difference of not more than 30% between the Young's modulus of the oxide and bulk material is advised [6].

Conclusion: MAX phases with self-healing potential

All criteria correctly identify Ti_2AlC, Ti_3AlC_2 as self-healing MAX phases. Cr_2AlC only meets the primary criteria, as there is a CTE mismatch. An overview of MAX phases that meet the primary criteria and the secondary criteria, respectively, is shown in Table 2. For some compounds data on diffusion is not available, so it is unknown whether dominant and fast A-element diffusion will take place upon oxidation.

Nevertheless, based on this analysis, Ta_2AlC is one of the MAX phase compounds with high self-healing potential.

Table 2: Overview of MAX phases that meet primary and secondary criteria for self-healing.

MAX phase compounds that meet primary criteria	V_2AlC, V_3AlC_2, Nb_2AlC, Zr_2AlC, Zr_2AlN, Ti_3SiC_2 Diffusion data missing: Mo_2GaC, Cr_2AlC, Cr_3AlC_2, Ti_2AlN, Ti_3AlN_2, Ta_2AlC, Ta_3AlC_2
MAX phase compounds that also meet secondary criteria	Ta_2AlC,Ti_3SiC_2, Ti_2AlC

2.4 Synthesis of MAX phases

Various sintering methods can be used to synthesize dense bulk MAX phases. A general distinction can be made between one-, and two-step routes. For two-step routes, MAX phase powder is first synthesized by reactive sintering. Densification of the MAX phase powder to form bulk material takes place afterwards by conventional non-reactive sintering. For one-step routes, reactive sintering and densification take place at once. All known sintering methods for synthesis of MAX phases are briefly described in section 2.4.1. A literature review on synthesis details for Ta-Al-C MAX phases is given in section 2.4.2

2.4.1 Synthesis methods for MAX phase synthesis

MAX phase can be synthesized from a powder mix consisting of elemental powders and/or carbides. Powder constituents are usually dry mixed an cold pre-pressed to a powder compact, prior to sintering. The powder compact is commonly referred to as 'green body'.

Sintering methods for synthesis of MAX phase powders

Pressure-less sintering (PLS) is a conventional sintering method in powder metallurgy, where the green body is heated by external heating elements in a furnace, without applying external pressure. In all cases reported for PLS of MAX phase, sintering takes place in vacuum or in a flowing argon atmosphere, to avoid oxidation during sintering [38]. The released heat caused by the exothermic reactions in the powder compact during sintering makes the green compact expand, and was found to cause pore forming in the final product after synthesis [38]. Therefore, PLS MAX phase samples are generally porous. The porous sample can powdered and densified to bulk MAX phase by further sintering under pressure by other methods. Furthermore, it was found that for the use of Si and Al, a part of the A-element easily evaporates at the required sintering temperature for MAX phase formation (> 1300 °C). Hence, the use of excess A-element is reported for PLS [38]. It is reported by Zhou *et al.* [38] that sintering methods with pressure assistance increase the cost, compared to sintering with PLS. Compared to pressure-assisted synthesis methods, PLS is relatively less costly than pressured sintering methods.

Zhou *et al.* [38] and Qian *et al.* [39] mention several successful synthesis routes for Ti-Si-C and Ti-Al-C MAX phase with PLS in their review on synthesis of MAX phases. Pietzka and Schuster [40] report that it is hard to synthesize pure Ti_3AlC_2 and Ti_2AlC because of the weak bonding of the Al atoms with TiC in the MAX phase, which causes the Al atoms to easily migrate

and evaporate causing the resulting MAX phase to be carbon deficient. 97 wt.% phase-pure Ti_3AlC_2 was PLSed by Peng *et al.* [41] by sintering of a powder mix of TiC, Ti, and Al (ratio 2 : 1 : 1) between 1300 and 1400 °C in flowing argon for 15-30 minutes. They propose that melting of Al (above 660 °C) enhances the reaction process. Sun *et al.* [42] reports the necessity for the use of 10 at.% excess Si to synthesize Ti_3SiC_2 from Ti, Si, and TiC powder, to compensate for evaporation of Si during PLS. Li *et al.* [43] also reports on the use of excess Si for synthesis of Ti_3SiC_2 by PLS from elemental starting powders.

Mechanical alloying (MA) induces reactive sintering of the solid-state powder constituents by ball milling of the powder mixture in a high-energy ball mill, causing fracturing of the powder constituents and cold welding. Several attempts to synthesize Ti_3SiC_2 MAX phase with MA are reported in literature. Li *et al.* [44] observed that MA of elemental Ti, Al, and C powder with large balls (20.6 mm diameter) leads to the formation of a significant fraction of Ti_3SiC_2, whereas the use of small balls (12.7 mm diameter) does not result in any MAX phase. Jin *et al.* [45] found that adding a small amount of Al to the powder mix increases the relative amount of Ti_3AlC_2 MAX phase formed upon MA. Zhai *et al.* [46] report that MA of an elemental powder mix with excess Si results in TiC, Ti_3SiC_2, and silicide powder. As MA only transforms a small fraction of the starting powders into MAX phase, the powder is usually further annealed or sintered with PLS after MA. It was found that MA promotes PLS sintering and densification of Ti_3SiC_2, and can result in 95.8 vol.% MAX phase [47].

For self-propagating high-temperature synthesis (SHS), or combustion synthesis, the required heat to induce reactive sintering of the powder constituents is delivered to the green body by the exothermic reactions taking place when MAX phase forms. The reaction is ignited by point-heating of a small spot on the green body, after which the exothermic reaction becomes self-sustaining, and travels through the remaining unreacted green body as a reaction front [38]. A clear advantage of SHS is the lack of extra energy needed to form MAX phase, after the initial reaction has been ignited. A drawback resulting from the self-sustaining reaction is the lack of control over the sinter-time and the temperature profile in the powder compact [39].

SHS has been used to synthesize Ti_2AlC, Ti_3AlC_2, and Ti_3SiC_2 MAX phase. Attempts to synthesize Ti-Al-C MAX phases from elemental powders did not always result in phase-pure powders [48], and carbon deficient Ti_2AlC_{1-x} was also reported [49]. Addition of Sn was found to enhance the reaction to Ti_2AlC [50], and the carbon content was reported to greatly influence the amount of Ti_3AlC_2 formed by SHS [51]. For Ti_3AlC_2, the mechanism proposed for MAX phase formation by SHS is solution-precipitation of TiC particles which dissolve in the Ti-Al melt and cause precipitation the MAX phase [52]. Additionally the use of TiAl [53], TiC, and Al_4C_3 as starting powder constituents were investigated. TiC lowers the reaction temperature, and Al_4C_3 increased the mass fraction of Ti_3AlC_2 in the final product [54]. Synthesis of Ti_3SiC_2 by SHS from elemental powders was reported to also consist of TiC impurities [55]. Gauthier *et al.* [56] have proposed that Ti_3SiC_2 forms by a reaction between molten Ti-Si and solid TiC_x. Replacing Si with SiC in the starting powder mix is assumed to result in a reaction without any liquid phase [57]. Huang & Cheng [58] have combined SHS with additional heat treating after SHS (15 seconds) to synthesize 90 % phase pure Ti_3SiC_2. Again, the use of TiC or SiC in the starting powder mix

results in a lower reaction temperature, and hence a lower flame-front propagation velocity, which makes SHS more controllable [54].

Sintering & synthesis of dense bulk MAX phase in one step

With Hot Pressing (HP) and Hot Isostatic Pressing (HIP) the green body is heated by external heating elements and external pressure is applied during sintering. During HP, the external pressure on the green body is applied with graphite punches and is in the order of 40 MPa [38]. During HIP, the green body is fully encapsulated in glass, and pressure of approximately 200 MPa can be applied via surrounding argon atmosphere in the HIP equipment [38]. A schematic of the HP and HIP equipment is shown in Figure 7. With HIP, a higher and more uniform pressure can be applied to the green body during reactive sintering. Also, loss of A-element (reported for Al and Si) due to evaporation or melting can be better avoided with HIP than with HP, due to full encapsulation of the powder compact [38]. Advantages of HP in comparison to HIP are that it is less costly and time consuming, and can be used for production of relatively large-scale samples [39].

The first ever made dense bulk MAX phase was synthesized by Barsoum *et al.* [59] by hot pressing Ti, SiC, and C (ratio 3 : 1 : 1) at 1600 °C and 40 MPa for 4 hours, which resulted in dense bulk Ti_3SiC_2 with 2 vol.% SiC and TiC. Various other MAX phases have since been fabricated by HP of various starting powders (elemental, carbides, nitrides). Zhou *et al.* [38] mention Ti_2AlC, Ti_3AlC_3, Ti_2AlN, Ti_2GeC, Ti_3GeC_2, and Cr_2GeC in a review on MAX phase synthesis. Similarly, Qian *et al.* [39] additionally mention Ti_3AlC_3, Ti_2SnC, Cr_2AlC, Ta_2AlC, Nb_2AlC, Ta_4AlC_3, and Nb_4AlC_3. It is mentioned that a HP is based on a solid-liquid reaction at elevated temperatures between the powder constituents [39].

Barsoum *et al.* [59] has also synthesised Ti_3SiC_2 with 1 vol.% SiC and TiC with HIP at 1600 °C for 4 hours, using the same powder mix as used for HP. HIP resulted in higher purity of the MAX phase. Additionally, it was found that a lower sintering temperature (1450 °C) resulted in a different grain size [60]. Li *et al.* [61] synthesized Ti_3SiC_2 from elemental powders with HIP at 1500 °C, 200 MPa, for 2 hours. Other MAX phases that were successfully synthesized by HIP from elemental, carbide, or nitride powders are Ti_3AlC, Ti_4AlN_3, Ta_2AlC, Ti_2InC, Zr_2InC, Hf_2PbC, Zr_2PbC, V_2AlC [39], and Ti_3AlC_2, Ti_2AlN, $Ti_2AlC_{0.5}N_{0.5}$ [38].

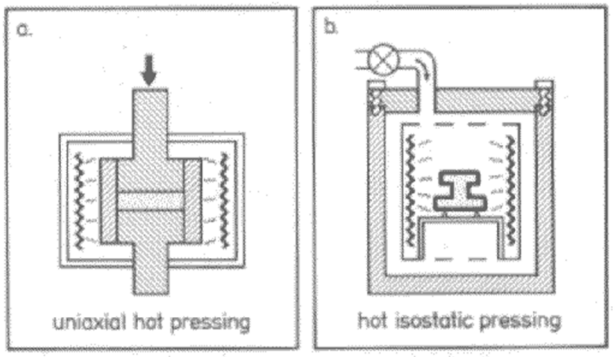

Figure 7: Schematic of a) the hot pressing (HP), and b) hot isostatic pressing (HIP) sintering method [62]

For Spark Plasma Sintering (SPS) no heating elements are needed. Instead, Joule heating takes place by passing a pulsed direct current through graphite mould and punches, and green body. Pressure in the order of 50 MPa can be applied via graphite punches during sintering. Advantages of SPS in comparison to HP and HIP are the high heating and cooling rates that can be reached through Joule heating [38]. The powder compact is heated relatively homogeneously. SPS is currently relatively costly, can only be used to fabricate small amounts of dense bulk MAX phase, and is hence used on laboratory scale [38].

Ti_3SiC_2, Ti_3AlC_2, Ti_2AlC, Cr_2AlC, Ti_2AlN have been synthesized in dense bulk form by SPS from elemental and carbide powder precursors by Zhou *et al.* [38] and Qian *et al.* [39]. Zhu *et al.* [63] found that Al addition enhances the formation of Ti_3SiC_2 during SPS, and accelerates its crystal growth. Yang *et al.* [42] reports on the use of mechanically alloyed powders for SPS (1050 °C, 10-20 min), which resulted in Ti_3AlC_2 with less than 1 wt.% TiC impurity.

Pressured-assisted self-propagating high-temperature synthesis (PSHS) works via the same principle as SHS (reactive sintering via a self-sustaining reaction front), but additionally pressure is applied on the green body during sintering. The drawbacks of this method are also similar to SHS; very short sinter time, and no control over the heating process during reaction sintering [38]. Almost single-phased Ti_3AlC_2 from elemental powders with excess Al has been fabricated with PSHS [64]. Bai *et al.* [65] reported that for synthesis of Ti_3SiC_2 and Ti_2AlC by PSHS, the Ti/C mol ratio strongly influences the purity of the final product, with an optimal Ti/C ratio stated to be Ti:C = 3 : 2 for Ti_3SiC_2.

2.4.2 Synthesis of Ta-Al-C MAX phases

The syntheses of bulk Ta_2AlC seems to have been attempted only a few times (all in recent years), judging from the amount of scientific publications available on the topic. Syntheses of bulk Ta_2AlC from elemental powders (tantalum, aluminium, carbon) is reported [66-71], but in other cases pre-ordered powder precursor of Ta_2AlC is used [72-76].

Synthesis of dense bulk Ta-Al-C MAX phase from Ta_2AlC powder precursor

Powder precursor of Ta_2AlC can be obtained from the company 3-ONE-2, located in Voorhees, USA. The method used by 3-ONE-2 to synthesize the Ta_2AlC powder precursor is patented, and hence no details can be found in literature. Also, the particle size distribution is said to be 'rather broad', giving a value range of 5-15 µm [76]. In another publication the purity of the Ta_2AlC powder precursor is said to be >92 % [74].

Synthesis of Ta-Al-C MAX phase from elemental powders

Mixing compositions and mixing methods

Two different optimal compositions have been found, which are used for different synthesis methods. An overview is given Table 3. From the details Table 3 it becomes clear that the synthesis method used in Xiang's research [67] is the same as the synthesis method described

in Hu's paper [66]. Note that for the 2:1.6 :1 composition, two different synthesis methods are described in the two publications cited.

It stands out that all of the optimal compositions given in literature are off-stoichiometric. Yeh *et al.* [68] propose that the excess amount of Al is needed to compensate for the amount of Al that will evaporate as the synthesis temperature during combustion synthesis (and also during the synthesis processes via other methods) is higher than the melting point of Al. This is in accordance with the known loss of Al and Si in other MAX phase synthesis attempts [38, 39], see section 2.4.1.

Table 3: Overview of detail on mixing compositions of Ta, Al, and C for synthesis of Ta_2AlC, as reported in literature.

Reference	Year of publication	Optimal composition	Syntheses method used
[66]	2008	Ta:Al:C = 2:1.2:0.9	Hot pressing (HP)
[68]	2009	Ta:Al:C = 2:1.6 :1	Combustion synthesis
[71]	2012	Ta:Al:C = 2:1.6 :1	Pressure-less sintering*
[67]	2014	Ta:Al:C = 2:1.2:0.9	Hot pressing (HP)

* It is not clear whether the samples synthesized in this research consist of dense or porous bulk Ta_2AlC

The mixing method of ball-milling is stated in several papers, with some difference in mixing time and extra details on the mixing process mentioned. Table 4 summarizes all information found on mixing method.

Table 4: Overview of detail on mixing methods of Ta, Al, and C for synthesis of Ta2AlC, as reported in literature.

Reference	Year of publication	Ball milling time (hours)	Extra information
[69]	2006	10	-
[66]	2008	12	Mixing in agate jar; Afterwards sieving with 100-mesh screen
[68]	2009	-	Dry mixing
[71]	2012	12	-

Cold pre-pressing of powder constituents

After the elemental powders are proposedly uniformly mixed by ball milling, a subsequent cold pressing step, in order to produce the green body is required [66, 68]. The cold pressed green body is then used as the starting product for the following synthesis steps. Table 5 summarizes all the details on the cold pressing steps known. Note the relatively large difference in pressures for cold pressing (5 MPa versus 500 MPa). The samples that were pressed with 500 MPa are used to synthesise bulk Ta_2AlC via pressure-less sintering. The lack of elevated pressure during PLS (compared to all other sintering methods) could explain the relatively high pressure used during cold pre-pressing.

Table 5: Overview of details on cold pre-pressing of powder constituents for MAX phase synthesis, as reported in literature.

Reference	Year of publication	Pressure (MPa)	Extra information
[66]	2008	5	Uniaxial pressing BN-coated graphite die
[68]	2009	-	Dimensions of tables: diameter = 7 mm, height = 12 mm Compact density = 45% (relative to the theoretical density)
[71]	2012	500	Uniaxial pressing

Details on sintering of Ta_2AlC

The use of hot pressing to synthesize Ta_2AlC is briefly mentioned by Lin *et al.* [69], and a very similar HP process is discussed by Hu *et al.* [66], but with more details. In all cases, HP takes place under Argon atmosphere. Table 6 summarizes the parameters for the different heat treatment steps of HP, as described by Hu *et al.* No details are stated on the cooling rate from the first holding step to the second holding step. In comparison, Lin *et al.* [69] states a holding time for the first holding step, of 1 hour instead of 30 minutes. After HP, contamination is removed from the sample surface with a high-speed running grinding wheel [66].

Table 6: Process parameters from Hu et al. for Hot Pressing of Ta_2AlC [66]

Parameter	Details
Heating	15 °C/min till T = 1550 °C
1st holding step	old at 1550 °C for 30 min under pressure of 30 MPa
2nd holding step	Anneal at 1400 °C for 60 min (no information about pressure given)
Cooling	Cool down to T_{room} by natural furnace cooling

Hu *et al.* [66] claim to have produced dense bulk single-phased Ta_2AlC, with a density of 11.46 g/cm, which is very close to the theoretical density of 11.52 g/cm.

About the microstructure of the samples, it is stated that "T*he average size of plate-like grains of Ta_2AlC is 15 μm in length and 3 μm in width (Fig. 2(a))"* [66]. Lin *et al.* [69] also report on the microstructure of the bulk Ta_2AlC samples after HP, giving a range for the grain dimensions, instead of an average value, i.e. *2 to 25 μm in length and 50–400 nm in*.

In several publications, the use of HIP is mentioned to synthesize dense bulk Ta_2AlC [72, 74, 75, 77], and in all these cases Ta_2AlC powder precursor from 3-ONE-2 is used as starting product. Research has been conducted on Ta2AlC and Cr2AlC Ag-based composites, where a mixture of Ta_2AlC and Ag powder is used for HIPing [72]. Some details on the process parameters during HIPing [74, 75], are summarized in Table 7.

Table 7: Summary of process parameters for HIPing of Ta_2AlC powder precursor

Publication/Parameter	Temperature	Pressure	Holding time
Gupta et al., 2008 [75]	1100 °C	70 MPa	0.3 hour
Drulis et al., 2008 [74]	1600 °C	70 MPa	8 hours

It is interesting to note the big differences in temperature and holding time shown in Table 7. Both publications claim that the final products are 'predominantly single phased'.

Synthesis of bulk Ta_2AlC via 'self-propagating high-temperature synthesis' (SHS) or 'combustion synthesis' has been attempted by Yeh *et al.* [68]. Based on the formation of TaC and Ta_2C by SHS [78], in which the combustion reaction was *"characterized by a high reaction temperature of about 1700 ◦C and a fast reaction front was readily achievable in the elemental powder compacts composed of Ta:C = 1:1 and 2:1."* [68]. The effect of an addition of aluminium to the powder mixture is discussed for various mixing compositions, it is presumed that the chemical reaction that enables the synthesis of bulk Ta_2AlC via SHS is still "*the elemental reaction of Ta with C, which subsequently triggers the reactions involving other elements and/or intermediates to complete the SHS process."* [68].

It is important to note that the best achievable final product by SHS is porous bulk Ta_2AlC, with a density of 48,6% relative to dense Ta_2AlC. The authors state that "*the synthesized product is suitable to be utilized as precursors for powders*" [68]. In this way, the process of SHS could give some insight on the synthesis of Ta_2AlC powder precursor (which is patented by 3-ONE-2 [79], and hence not publically available).

Lane *et al.* [71] describe research on first-order Raman scattering of various MAX phases, and compares theoretically calculated results (based on first principle calculations using density functional theory) with experimental results. To obtain these experimental results, bulk Ta_2AlC samples are used, made from cold-pressed green bodies of elemental powders, which were then sintered *pressure-less* in an alumina tube furnace. The details of the cold-pressing- and sintering step is given in Table 8. The composition (single phase, or other phases present), density (relative to the theoretical density) and purity of the bulk Ta_2AlC is after pressure-less sintering is not stated.

Table 8: Parameters for pressure-less sintering [71]

Parameter	**Details**
Cold pressing pressure	500 MPa
Heating rate	10 °C/min
Holding temperature	1500 °C
Holding time	1 hour
Atmosphere	Flowing argon

2.5 Material properties of Ta-Al-C MAX Phases

An overview of different MAX phase compounds from the Ta-Al-C system and their material properties is given in this section. A distinction is made between experimentally determined values, and values based on first principle calculations. It is reported in literature that experimental Raman spectra of Ta_4AlC_3 "*are reasonably accurately predicted by ab initio calculations*" [71], p.5. Hence it is assumed that experimental as well as first principle values found in literature can provide useful information for comparison with the samples synthesised in this work.

Different Ta-Al-C MAX phase compounds

In 2006 Lin *et al.* separately identified the microstructures of Ta_6AlC_5, intergrown Ta_2AlC and Ta_4AlC_3, and intergrown Ta_4AlC_3 and Ta_6AlC_5, via transmission electron microscopy (TEM). A general crystallographic orientation relationship between binary cubic TaC and ternary Ta-Al-C carbides is proposed [80].
The theoretical density of Ta_2AlC is reported to be 11.52 g/cm^3 [26], based on *ab initio* total energy calculations. The calculated theoretical density of Ta_4AlC_3 is 12.919 g/cm^3 [81].

Several publications report on the lattice parameters of different Ta-Al-C MAX phase compounds. An overview is given in Table 9, where the lattice parameter a and c are shown per compound. The lattice parameters have been determined via a variety of experimental and theoretical methods.

Table 9: Overview of lattice parameters from literature, for several Ta-Al-C MAX phase compounds.

Experimental or calculation	Compound	Values (Å)
Exp.	Ta_2AlC	a = 3.075, 3.079 [80]; 3.086 ± 0.006 [73]; 3.079 [66]; 3.086 ± 0.006 [82]; 3.086 [77] c = 13.830, 13.860 [80]; 13.85 ± 0.04 [73]; 13.854 [66]; 13.85 ± 0.04 [82]; 13.85 [77]
Calc.	Ta_2AlC	a = 3.074 [80]; 3.070 [73]; 3.15 [70]; 3.08 [82]; 3.07 – 3.12 [77] c = 13.500 [80]; 13.598 [73]; 13.95 [70]; 13.90 [82]; 13.72 – 14.02 [77]
Calc.	Ta_3AlC_2	a = 3.072 [80] c = 18.750 [80]
Exp.	Ta_4AlC_3	a = 3.092 [80, 83] c = 23.708 [80, 83]
Calc.	Ta_4AlC_3	a = 3.070 [80, 83] c = 24.198 [80, 83]
Calc.	Ta_6AlC_5	a = 3.078 [80] c = 34.681 [80]

Electrical & thermal properties

An overview of the values of the electrical and thermal properties of several MAX phase compounds from the Ta-Al-C system is shown in Table 10. Based on the experimental and calculated properties, it can be concluded that MAX phase compounds from the Ta-Al-C system are indeed electrical and thermal conductors.

Table 10: Overview of electrical and thermal properties from literature, for several Ta-Al-C MAX phase compounds.

Property	Experimental or calculated	Compound	Value	Reference
Electrical conductivity (· $10^6\ \Omega^{-1} \cdot m^{-1}$)	Exp.	Ta_4AlC_3 Ta_2AlC	2.59 3.91	[83] [66]
Temperature coefficient of resistivity (K^{-1})	Exp.	Ta_4AlC_3 Ta_2AlC	0.0035 0.0042	[83] [66]
CTE (· $10^{-6}\ K^{-1}$)	Exp.	Ta_4AlC_3 Ta_2AlC	8.2 ± 0.3 8.0	[83]
Heat capacity ($J\cdot(mol\cdot K)^{-1}$)	Exp., at 298 K	Ta_4AlC_3 Ta_2AlC	185 93.6	[83] [66]
Thermal conductivity ($W\cdot(m\cdot K)^{-1}$)	Exp., at 25 °C	Ta_4AlC_3 Ta_2AlC	38.4 28.4	[83] [66]
Debye temperature (K)	Exp.	Ta_2AlC	281	[74]

Mechanical properties

shows an overview of the values of the mechanical properties of several MAX phase compounds from the Ta-Al-C system, as reported in literature.

Theoretical calculations of the bulk modulus of the various compounds of Ta-Al-C MAX phases show that it is related to the atomic arrangement in the various compounds. The resistance of a material to a volume change is quantified with the bulk modulus, and is directly related to the chemical bonding within a material. As the atomic fraction of Ta- and C increases, the bulk modulus also increases, as can be seen in Table 11. This is assumed to be related to the fact that the "*Ta-C bonds are much stronger than the Ta-Al bonds*" [80], p. 5.

Table 11: Overview of mechanical properties from literature, for several Ta-Al-C MAX phase compounds.

Property	Experimental or calculated	Compound	Value	Reference
Vickers hardness (GPa)	Exp.	Ta_4AlC_3 Ta_2AlC	5.1 ± 0.1 4.4 ± 0.1	[83] [66]
Compressive strength (MPa)	Exp.	Ta_4AlC_3 Ta_2AlC	821 ± 97 804	[83] [66]
Shear strength (MPa)	Exp.	Ta_4AlC_3 Ta_2AlC	254 ± 19 112 ± 24	[83] [66]
Flexural strength (MPa)	Exp.	Ta_4AlC_3 Ta_2AlC	372 ± 20 306 ± 19	[83] [66]
Fracture toughness (MPa · $m^{1/2}$)	Exp.	Ta_4AlC_3 Ta_2AlC	7.7 ± 0.5 7.7 ± 0.2	[83] [66]
Young's modulus (GPa)	Exp.	Ta_4AlC_3 Ta_2AlC	324 292	[83] [66]
Shear modulus (GPa)	Exp.	Ta_4AlC_3 Ta_2AlC	132 121	[83] [66]
Bulk modulus (GPa)	Calc. Calc. Exp.	Ta_2AlC Ta_3AlC_2 Ta_4AlC_3 Ta_6AlC_5 Ta_2AlC Ta_2AlC	210 238 259 285 206 251 ± 3	[80] [82]
Specific wear rate (SWR) (mm^3 / (N · m))	Exp., at 550 °C, 3N load, in air, against Al_2O_3	Ta_2AlC	≤ · 10^{-6}	[75]
Coefficient of friction μ_s	Exp., at 550 °C, 3N load, in air, against Al_2O_3	Ta_2AlC	0.92 ± 0.01	[75]

2.6 Oxidation behaviour of $Ta_{n+1}AlC_n$, Ta, Tantalum-carbides

Self-healing potential of MAX phases is determined by its oxidation behaviour. It was found that the oxidation behaviour of Ta_2AlC and mixed Ta_2AlC and Ta_4AlC_3 seems to be mainly governed by the presence of tantalum in the MAX Phase.

2.6.1 Oxidation behaviour of $Ta_{n+1}AlC_n$

Gupta *et al.* [84] performed isothermal oxidation experiments on hot-isostatically pressed (HIPed) dense (11.82 g/cm^3; >98 % theoretical density) Ta_2AlC samples with minor Ta_4AlC_3 as an impurity phase, in the temperature range of 600 to 900 °C for 20 to 40 hours in air. A clear difference in oxidation behaviour was found for temperatures below 600 °C versus temperatures above 700 °C.

At 600 °C a thin (< 10 µm) oxide layer is formed, and the weight gain caused by oxidation is too low for detection (by microbalance). The oxide layer is initially protective, which is verified by the fact that the thickness does not increase further after more than 40 hours of isothermal

oxidation. XRD analysis shows weak and broadened peaks corresponding to Ta_2O_5 and $TaAlO_4$. EDS analysis shows a stoichiometry in the oxide scale of Ta:Al:O ≈ 2:1:6.5, which corresponds to oxidation states Ta^{5+} and Al^{3+}. Based on these results the oxide scale formed at 600 °C is assumed to be largely X-ray amorphous. Furthermore, the oxide scale was found to not be resistant to thermal cycling.

Above 700 °C the oxide scale shows no phase separation or well-formed grains on micrometre scale, and is porous and highly cracked. XRD analysis shows crystalline phases Ta_2O_5 and $TaAlO_4$, and an amorphous phase. Noticeable peak broadening is assumed to denote small oxide grains. According to EDS analysis the oxide layer is fully oxidized and maintains the same Ta/Al ratio as the original bulk Ta_2AlC sample. Within the entire 700 – 900 °C range the oxidation kinetics are found to be linear, and with increasing temperature the reaction rate constant increases almost linearly. Based on XRD analysis, the volume fraction of $TaAlO_4$ increases for higher isothermal oxidation temperatures.

It is reported that the linear oxidation kinetics of Ta_2AlC suggests a reaction at the oxide/carbide interface as the rate-limiting process for oxidation. The lack of parabolic-type oxidation kinetics is explained by the presence of the pores and cracks in the oxide scale, which facilitate easy access of oxygen to the reaction interface. Additionally, easy outward diffusion of CO_2 gas can take place. Pores and cracks are assumed to form as a result of stresses within the oxide scale, for which two main causes are put forward. One cause is the difference in thermal expansion between Ta_2O_5 and Ta_2AlC, which are $4 \cdot 10^{-6}\,K^{-1}$ and $5.7 \cdot 10^{-6}\,K^{-1}$ respectively. Second cause described is the relative volume change upon oxidation, which is stated to be 50%. The proposed oxidation reaction for Ta_2AlC is a two-step reaction:

$$Ta_2AlC + O_2 \rightarrow 2Ta_2O_5/Al_2O_3 + 2CO_2 \quad (1)$$
$$2Ta_2O_5/Al_2O_3 \rightarrow 2TaAlO_4 + Ta_2O_5 \quad (2)$$

Where Ta_2O_5/Al_2O_3 denotes a possibly multiphased or amorphous reaction product. It stands out that no Al_2O_3 was observed. Carbon is assumed to be fully converted upon oxidation, as it was not accumulated on the oxide/MAX phase interface. Reaction 2 is assumed to be favoured at higher temperatures. It is stated that this reaction scheme is similar to the reaction scheme for oxidation of Nb_2AlC in air.

2.6.2 Oxidation behaviour of pure Ta

The assessed Ta-O phase diagram has been stated by Garg *et al.* [85], and is shown in Figure 8. The solubility of O in Ta is lower than 5 at.% up to 1200 °C, and for the temperature range of 600 to 1550 °C is stated to be best represented by:

$$\log C_s = (1.25 \pm 0.04) - (1036 \pm 40)/T$$

Above approximately 71 at.% oxygen β-Ta_2O_5 forms up to 1360 °C. At higher temperatures β-Ta_2O_5 converts to α-Ta_2O_5. The phase transformations at even higher temperatures are not relevant for this work. Garg *et al.* [85] also provides a literature review of many metastable Ta-O phases reported in other works, of which an overview is given in Table 12. On the presence of these metastable Ta-O phases Garg *et al.* notes that none have been isolated in pure form, "*and*

reported methods of their synthesis have generally poor reproducibility" [85] p.1. Furthermore, many different mechanisms have been proposed for their formation, and that they probably happen "*by kinetically influenced transformations*" [85] p.1. Stabilisation happens "*either under thin film conditions or by the presence of impurities*" [85] p.1. The composition is not well defined for all metastable phases.

Garg *et al.* state various values for the enthalpy of formation and free energy of formation of Ta_2O_5, and recommends respectively -2046.0 ± 2 kJ/mole (at 25 °C) and -1429.7 kJ/mole (at 1156.7 °C) as most precise [85].

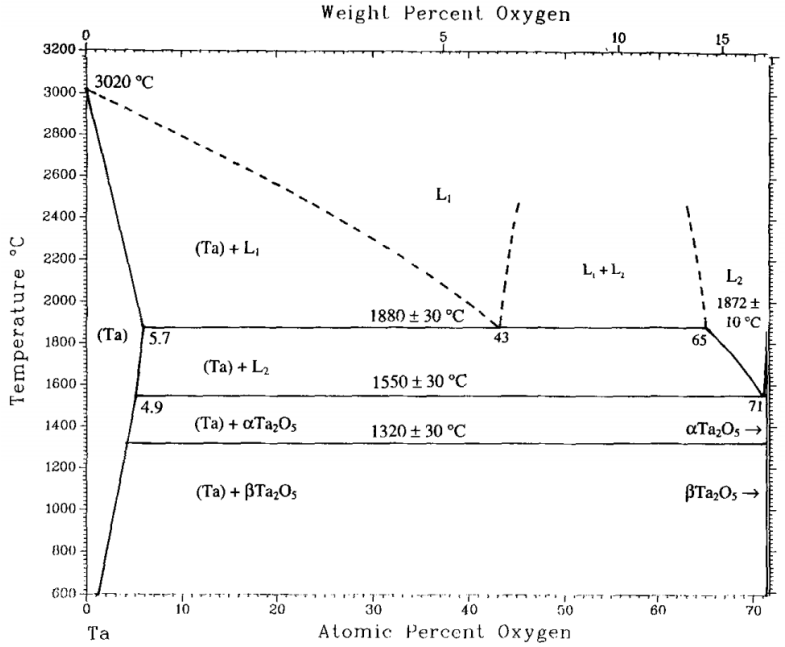

Figure 8: Ta-O phase diagram as assessed by Garg et al. [85].

Table 12: Ta-O crystal structure data for the metastable phases [85].

Phase	Composition, at.% O	Pearson symbol	Space group	Strukturbericht designation	Prototype	Reference
TaO_x	14.3	Tetragonal	...	...	Nb_6O	[58Bra, 62Bra]
	...	Tetragonal	...	...	...	[67Ste]
	7.7	Tetragonal	...	...	...	[78Mil]
TaO_y	20.0	*oP*5	*Pmmm*	D_{2h}^1	...	[54Sch]
	...	*o***	...	...	...	[62Bra, 68Way]
TaO_z	33.3	*t***	...	...	...	[62Bra, 62Nor1,66Nie, 67Ter, 79Hor]
	...	*c***	...	*C*3	Cu_2O	[65Ste]
	...	Orthorhombic	...	...		[65Ste]
	46.8 to 50.0	Cubic	...	...	...	[73Har]
TaO_w	(a)	...	...	...	...	[64Kof]
$\alpha_1Ta_{16}O$	5.9	Tetragonal	...	...	...	[69Usi, 79Hor]
α'_1Ta_4O	20	Tetragonal	...	...	...	[69Usi, 79Hor]
α_2Ta_4O	20	Tetragonal	...	...	...	[69Usi, 79Hor]
α'_2Ta_2O	33.3	Tetragonal	...	...	...	[69Usi, 79Hor]
TaO	50	fcc	$Fm\bar{3}m$	*B*1	NaCl	[54Sch, 72Fer]
	50	*cF*8	$Fm\bar{3}m$	*B*1	NaCl	[68Kle]
	50	*cF*16	$Fm\bar{3}m$	$D0_3$	BiF_3	[68Kle]
Ta_2O_3	Amorphous	...	...	...	...	[69Ala, 77Nis]
TaO_2	66.67	*tP*6	$P4_2/mnm$	C_4	TiO_2	[54Sch]
	66.67	...	...	D_{4h}^{14}	...	[57Kra]
	66.45 to 67.34	...	...	...	TiO_2	[83Syo]
	66.67	...	...	...	...	[89Mir]
$\alpha''Ta_2O_5$	...	Monoclinic	...	...	...	[64Lav]
$\alpha'Ta_2O_5$	...	Monoclinic	...	...	...	[64Lav]
αTa_2O_5 (metastable)	71.43	Triclinic	...	...	...	[68War]
$\alpha'Ta_2O_5$	71.43	Monoclinic	...	...	...	[68War]
εTa_2O_5	...	*m***	...	...	βNb_2O_5	[79Izu]
Ta_3O_9	75	Monoclinic	...	C_{2h}^5	...	[76Khi]
$TaO_{0.72}$	41.9	*cF*8	...	...	...	[66Khi]
$TaO_{0.82}$	45	*cF*8	...	...	...	[66Khi]
$TaO_{1.25}$	55.6	*cF*8	...	...	...	[66Khi]
$32(TaO_{2-x})\ 0 \le x < 1$	...	bct	$I4_1/a$	...	Cu_2AlMn	[68Khi]
$TaO_{0.03}$	2.91	*cF*8	*Pmmm*	...	Perovskite	[66Khi, 70Khi]
$TaO_{1.7}$	63	*cF*8	*Pmmm*	...	Perovskite	[66Khi, 70Khi]
$TaO_{0.95}$	48.7	Cubic	*P*4/*mmm*	D_{4h}^1	...	[82Khi]
$TaO_{1.62}$	61.8	Cubic	*P*4/*mmm*	...	...	[82Khi]
	(b)	*oP**	*Pmmm*	...	...	[72Khi]
	(b)	Cubic	*Pbca*	...	...	[80Khi]
	(b)	Hexagonal	...	...	...	[54Sim, 55Fre, 67Ter, 79Aly, 80Khi]
	(b)	*hP*48	*P*6/*mmm*	...	...	[81Khi]

(a) Crystal structure data not reported. (b) Composition undefined.

Per Kofstad has studied the oxidation behaviour of tantalum in the temperature range of 300° – 1300 °C [86-89], for different O_2 pressures ranging from 1 atm to 0.001 Torr. Visual inspection of cross-sections of the oxidized tantalum samples showed internal oxidation and increasingly uneven oxidation of the sample surfaces over time. The edges of the sample are rounded off over time, and "*this preferred oxidation is believed to reflect that oxide formation takes place at the metal/oxide interface following a saturation of an outer layer of the metal with oxygen. The very edges become saturated faster with oxygen due to the simultaneous diffusion from the intersecting surfaces, and this causes a faster oxidation at such places*" [88] p. 5.

Comparison of an annealed and un-annealed (e.g. elongated grains in rolling direction) sample shows that internal oxidation happens preferentially along grain boundaries.

Kofstad shows that the mechanism of oxidation of tantalum is characterized by the formation of a thin suboxide on the metal/oxide interface, which precedes the formation of the main oxidation product β-Ta_2O_5. The following general steps are related to oxidation of tantalum:

1) During the first step, oxygen dissolution – which is the predominant process – and diffusion within the bulk metal takes place. This results in oversaturated solid-solution. Thermodynamically the formation of Ta-O solid solution has a higher free energy than oxide formation. Kofstad has called this step the 'incubation period', which becomes longer at lower oxygen pressure for each temperature between 300 and 1300 °C [87].
2) Formation of a thin suboxide on what will become the metal/oxide interface
3) Formation of the final oxidation product – β-Ta_2O_5 – on the suboxide

The weight gain over time due to oxygen dissolution is negligible compared to the weight gain caused by the final formation of the β-Ta_2O_5 oxide scale.

Three different possible suboxides are identified, which correspond to different oxidation mechanisms with different kinetics. Which mechanism takes place depends on temperature.

Below 500 °C the orthorhombic metallic suboxide TaO_y forms [86]. Below 800 °C the tetragonal metallic suboxide TaO_z forms [86], corresponding to an equilibrium oxygen concentration in solid solution in tantalum of 5-7 at.%. Springer *et al.* [90] proved the existence of suboxide plates at oxidation temperatures of 800 and 925 °C by observation of fine pore lines, which were demonstrated to be produced when suboxide plates are oxidized for longer times. They have also shown that the calculated tantalum-atom density in the suboxide is compatible with the tetragonal structure of TaO_z within the temperature range of 450 – 950 °C. Notably, this is a larger temperature range for the formation of TaO_z than that proposed by Kofstad *et al.* [88].

The β-Ta_2O_5 that forms on TaO_z is very porous from the beginning as relatively isolated β-Ta_2O_5 nuclei form, which subsequently grow into an uneven and discontinuous oxide scale [87]. The rate-determining reaction for oxidation is the nucleation and growth of β-Ta_2O_5, which is an approximately linear process over time. For oxidation below 750 °C, the activation energy for the linear oxidation is said to be approximately 28 kJ/mole for low O_2 pressure and/or higher temperatures, and approximately 297 kJ/mole for lower temperatures and/or high O_2 pressure.

From 800 °C onwards TaO forms, on a solid-solution with a concentration of 2.2-3.0 at.% of oxygen. The very initial oxidation kinetics follow parabolic behaviour, because β-Ta_2O_5 initially forms as a compact scale. According to Kofstad this probably reflects a Wagner-type oxidation mechanism, where the rate-determining reaction is the diffusion of oxygen ions through the compact β-Ta_2O_5 scale. The activation energy for initial parabolic oxidation (determined from the parabolic rate constant) was found to be approximately 188 kJ/mole at approximately 13 and 1333 Pa O_2 pressure (0.1 and 10 Torr) [88], and is assumed to correspond to the activation energy for vacancy diffusion. A comparable activation energy for initial parabolic oxidation at 900 – 1000 °C of 183 ± 8 kJ/mole was found by Voitovich [91], and it is stated that the apparent activation energy for oxygen diffusion in Ta_2O_5 is 179,3 kJ/mole.

Initial parabolic oxidation behaviour is followed after a relatively short time by linear behaviour up to 1050 °C. Two possible reasons for the transition to linear kinetics are given by Kofstad: 1)

the protective β-Ta_2O_5 cracks down to the oxide/metal interface due to internal stresses after which linear nucleation and growth of β-Ta_2O_5 is the rate-limiting reaction also above 800 °C [87] and 2) "*a linear depletion of a compact barrier layer into an outer porous layer*" [88] p. 9, [92]. Separate research on stress development due to oxidation of tantalum has been performed by Pawel *et al.* [93]. The curvature of rectangular polycrystalline specimens after one sided oxidation was used to calculate bending stresses resulting from the oxidation. A model which assumes surface stresses to be proportional to the oxygen concentration in tantalum was shown to be most consistent with experimental data on the oxidation rate. According to this model the surface stress rises a lot during the first minutes of oxidation – to approximately 345 MPa – after which almost no further increase of surface stress takes place. These observations made by Pawel *et al.* correspond best to the Kofstad's second possible reason for the transition to linear kinetics; the presence of a compact barrier layer on the oxide/MAX phase interphase. If a steady-state amount of oxygen is present in this compact barrier layer after initial oxidation, the oxidation stress will remain constant over time.

At 1100 – 1200 °C the oxidation kinetics decrease with time due to increased sintering and plastic properties of the scale. At 1200 – 1300 °C α-Ta_2O_5 starts to form instead of β-Ta_2O_5, after which the reaction rate of oxidation starts to increase with time. Furthermore it is stated that "*the activation energy of the linear oxidation above 800* °C *increases with temperature*." [88], p.10.

Kofstad states two possible reasons for the formation of an initially compact β-Ta_2O_5 above 800 °C, namely i) the fact that the suboxide "*TaO facilitates the formation of a more continuous, compact layer of* Ta_2O_5" than TaO_z, and ii) "*Higher temperature results in increased sintering of the oxide layer*" [88].

The following two reaction equations are proposed by Kofstad for the oxidation of pure tantalum, depending on temperature:

$$Ta + O_{chem.} \rightarrow O\ sol.sol'n \rightarrow TaO_y \rightarrow TaO_z \rightarrow Ta_2O_5 \qquad \text{(for oxidation ≤ 700 °C)}$$
$$Ta \rightarrow O\ sol.sol'n \rightarrow TaO \rightarrow Ta_2O_5 \qquad \text{(for oxidation ≥ 800 °C)}$$

Effect of tantalum purity on tantalum oxidation

Voitovich *et al.* [91] has also researched the oxidation behaviour of tantalum – Voitovich's findings on the general oxidation of tantalum coincide with those of the works of Kofstad – and has additionally looked into the effect of impurity on the oxidation of tantalum. An overview of chemical composition and microstructure type of the samples used is shown in Figure 9. It was shown that the mechanism of suboxide formation determines the effect of purity on tantalum oxidation.

Production method	Impurity content (wt.%)							
	C	N	O	Cu	Al	Si	Ti	Zr
Single crystal	0.003	0.003	0.008	—	—	0.004	0.002	—
Zone melting	0.008	0.006	0.025	0.001	0.001	0.005	0.002	0.001
Remelting of powder	0.030	0.025	0.220	0.003	0.030	0.030	0.008	0.004
	Impurity content (wt.%)							
	Cr	Mo	W	Mn	Fe	Ni	Nb	
Single crystal	—	0.005	0.003	—	0.001	—	0.020	
Zone melting	0.001	0.005	0.005	0.001	0.020	0.003	0.150	
Remelting of powder	0.010	0.020	0.020	0.007	0.055	0.008	0.430	

*0.002% Mg.

Figure 9: Chemical composition of tantalum specimens as shown in Voitovich's work [91].

The main findings regarding the effect of Ta impurity on oxidation are summarized. In the 600 – 800 °C temperature range, most impurity elements have low solubility in tantalum and inhibit oxygen dissolution. Hence diffusion of oxygen is also inhibited, and the thickness of the diffusion zone becomes smaller. This results in faster formation of a saturated solid-solution of oxygen in tantalum, which causes a more rapid formation of TaO_z suboxide platelets and a higher plate density of TaO_z. This subsequently intensifies formation of β-Ta_2O_5, thus causing faster oxidation of tantalum for higher impurity of the metal. Oxidation above 900 °C results in the formation of TaO as suboxide instead of TaO_z. The least-pure tantalum sample has the slowest oxidation during the initial parabolic oxidation. At O_2 pressures close to atmospheric, the concentration of anion vacancies in β-Ta_2O is determined by impurity.

Additionally, the grain boundary density in relation to tantalum impurity was shown to have an effect on oxidation kinetics. Polycrystalline tantalum has a higher oxidation rate due to oxygen diffusion along grain boundaries versus only volume diffusion in single crystal tantalum. However, polycrystalline tantalum melted from powder, which has a significantly higher level of impurity than the single crystal and zone melted samples, shows least oxidation above 900 °C. A possible reason as stated by Voitovich is that most impurity elements at these temperatures do not dissolve but are concentrated along the GB's. This may prevent oxygen diffusion along GB's and hence oxygen dissolution in the bulk metal. If no solid-solution of oxygen in tantalum can form, no suboxide will form either.

2.6.3 Oxidation behaviour of tantalum-carbides

Desmaison-Brut *et al.* [94] compared the oxidation behaviour of dense (> 98 % theoretical density) Hot Isostatically Pressed (HIPed) cubic (4^3 mm) samples of TaC (NaCl type structure) and Ta_2C (hexagonal type), in flowing oxygen (1 atm) between 750 and 850 °C, with a heating rate of $17 \cdot 10^{-3}$ °C/s.

Upon oxidation of TaC a porous and columnar oxide scale forms, which has cracked open on the cube edges (observed in cross-sections with SEM). A grey oxide was observed to form during initial oxidation. XRD analysis only shows the presence of β-Ta_2O in the oxide scale. No free carbon was observed within the oxide scale, and a direct reaction of carbon to form CO_2 upon oxidation is assumed. The oxidation kinetics are found to be quasi linear at low temperatures, and slow down somewhat in the upper temperature range.

Porosity and cracking of the oxide scale at the cube edges are assumed to be induced by good adherence of the oxide to the sample surface, combined by stresses induced by a high Pilling and Bedworth ratio of 2.13. This morphology leads to easy access of O_2 to the carbide-oxide interface and easy outward diffusion of CO_2. Hence oxidation of TaC is assumed to be rate-limited by an interface reaction. The decrease in oxidation kinetics at the higher measured temperature range is attributed to increased sintering of the oxide scale, which causes some stress-relieve and hence prevents some crack formation in newly formed oxide scale.

The activation energy for oxidation of TaC within 750 – 850 °C based on the measured weigh-gain curves is 379 ± 16 kJ/mole. A mathematical model for the reaction kinetics is proposed for TaC, and the calculated reaction energy based on this model (385 ± 11 kJ/mole) is in close agreement with the experimental value.

In contrast to TaC oxidation a relatively dense and well adherent oxide layer of β-Ta_2O_5 forms on Ta_2C. Furthermore, an interlayer with a maximum thickness of 20-25 μm is observed at the carbide-oxide interface. The presence of both carbon and oxygen is detected within the intermediate layer, and XRD analysis shows evolution of the Ta_2C lattice parameter, moving from the carbide into the interlayer. The interlayer is denoted as a general oxycarbide, TaC_xO_y. It disappears near the cube edges, and on the cube faces its thickness is independent of time. Formation of the oxycarbide interlayer is shown to start preferentially at Ta_2C grain boundaries and its growth speed is approximately constant. The oxycarbide layer was found to have a noticeably higher microhardness than β-Ta_2O_5, H_V^{5N}= 12.1 ± 0.9 GPa versus 3.5 ± 0.5 GPa. The Ta_2C samples have a measured microhardness of 10.7 ± 0.9 GPa.

Ta_2C shows parabolic-type behaviour upon initial oxidation, followed by linear kinetics. Its oxidation resistance over time is higher than that of TaC. Desmaison-Brut *et al.* [94] states that a diffusion process of reactants through the oxycarbide interlayer cannot be excluded as a rate-limiting reaction for the oxidation of Ta_2C. Loriers paralinear oxidation model is proposed for Ta_2C oxidation, which "*describes growth of multilayered scales where inner compact oxide grows at parabolic rate and is simultaneously oxidized to a higher oxide with no protective properties*" [94] p. 1333.

The activation energy based on measured weight-gain curves within 750 – 850 °C is 129 ± 7 kJ/mole for Ta_2C.

Desmaison-Brut *et al.* gives a possible explanation for the lack of formation of an oxycarbide layer on the interface between the MAX phase and oxide scale by looking at the difference between crystal structure of TaC and Ta_2C. TaC has a face centred cubic (fcc) structure with the carbon atoms at the octahedral sites, which leaves almost no vacant sites to by occupied by oxygen atoms (the TaC samples used by Desmaison-Brut *et al.* are only very slightly off stoichiometric; $TaC_{0.99}$). In Ta_2C only one out of two planes are occupied with carbon atoms, which might promote the dissolution and diffusion of oxygen into the Ta_2C matrix, and the formation of the oxycarbide interface layer.

3. Methods and Experimental Aspects

3.1 Sintering methods and sample preparation

Mixing of powders

Powder mixtures of elemental Ta, Al, and C powder and of Ta, Al_4C_3, and C were prepared by two methods. To prevent contamination with O_2 and H_2O, mixing and storage of all powders took place in dry argon atmosphere in a glove box or container during mixing. Powders were mixed on a roller mixer (RM5W, CAT, Germany, 80 rpm) in a glass jar, or in a Turbula mixer (T2C, Willy A. Bachofen (WAB) company, Switzerland, 60 rpm motor speed) in a plastic jar., Zirconia or tungsten carbide balls with 5 mm diameter were added with a ratio of approximately 10:1. to the powder mixture to enhance mixing. Both mixing methods produced the same results in terms of homogeneity and will not be further differentiated. An overview of all mixing compositions and sintering experiments is given in section 4.1. The general experimental details on powder mixing are summarized in Table 13.

Table 13: Experimental details on powder mixing.

Mixing method	Mixing time	Jar material	Ball material
Roller mixer	Minimum 24 hr	glass	ZrO_2
Turbula mixer	Minimum 12 hr	plastic	WC

Spark Plasma Sintering (SPS)

Dense bulk Ta-Al-C MAX phase samples were prepared by inducing reaction sintering of mixed tantalum, aluminium, and carbon powder, at elevated temperature and pressure. This was achieved by using the method of spark plasma sintering (SPS). “SPS is a low voltage, direct current (DC) pulsed current activated, pressure-assisted sintering and synthesis technique” [95]. An alternative name for SPS is ‘field-assisted sintering technique’, as up to date no spark or plasma has been detected during SPS [95].

During SPS, high temperatures are achieved through Joule heating caused by a pulsed current (DC) through the electrically conductive green body and its surrounding graphite die and punches. The energy produced by Joule heating is dissipated directly within the conductive parts, and mainly within the green body as it has the highest electrical resistivity. This quick and efficient transfer of heat through the green body makes high heating rates (1000 °C/min), relatively homogeneous heating of the sample, and fast sintering at relatively low sintering temperatures possible, compared to conventional techniques like HP and HIP. During SPS, uniaxial mechanical pressure is applied on the green body by conductive graphite punches, in order to assist densification. SPS takes place in a controlled atmosphere, i.e. vacuum or argon at overpressure, to avoid contamination of the sample during sintering. An image of the SPS equipment and a schematic of the main components is shown in Figure 10.

The combination of fast and homogeneous internal Joule heating and external application of mechanical pressure allows for synthesis of new compounds and/or densification to near

theoretical density in one step [95]. Because the graphite die and punches have a very high electrical conductivity, a relatively low voltage (< 10 V) can produce a high current which results in a high power electrical circuit. The sintering process can be controlled by temperature, power, current, or displacement measurement.

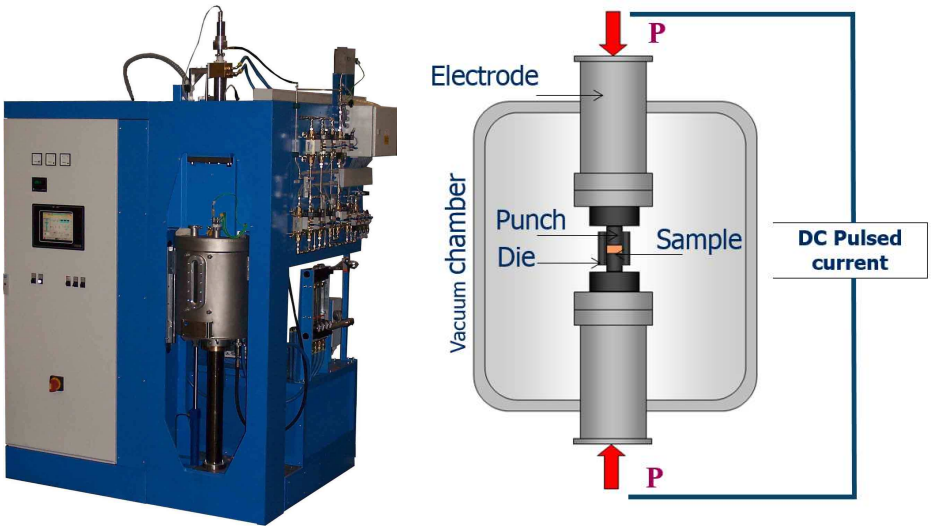

Figure 10: Spark Plasma Sintering equipment and schematic of the working principle.

The equipment used for this work is (HP D 25-SI, FCT Systeme GmbH, Germany). During heating and sintering a continuous DC was run through the sample and graphite sample holder components, and no use was made of pulsing of the current. Different sintering parameters were tested for optimal MAX phase synthesis, as described in section 4.1. All processes were controlled by temperature measurement with an axial pyrometer. Sintering took place in Argon (purity > 5 N) or vacuum atmosphere (≥ 0.77 mbar). A maximum uniaxial pressure of 50 MPa was applied to all samples during sintering, and in some segments of the temperature and pressure profile the pressure was decreased to a minimum of 5 MPa.

For preparation of SPS samples, the desired amount of powder is put in a graphite die with two graphite punches on both sides, and pre-pressed at 5 kN in the SPS vessel. To prevent powder leakage and reaction of the powder mix with the graphite die and punches during synthesis, an additional graphite sheet is placed between the die and punches, and boron nitride is sprayed on the inside of the mould and on all contact areas between the graphite sheet and powder mix. and punches during sintering. After preparation of mould and punches, the sample is placed in the SPS vessel between two graphite cones. A thick piece of graphite felt is wrapped around the graphite mould for heat insolation of the inner vessel during sintering.

Pressure-less sintering (PLS)

Pressure-less sintering (PLS) was used to attempt synthesising of Ta-Al-C MAX phase. PLS samples can then be further densified by other means (for example by SPS).

During PLS, a cold pre-pressed green body is heated to the desired sintering temperature with external heating elements in a furnace under a controlled atmosphere . No external pressure is applied during heat treatment. Chemical reactions and/or densification during sintering is only

caused by the increase of temperature in the green body. The final product commonly has a lower density than the densification achieved with pressure assisted HP, HIP, or SPS [39]. The lack of pressure is beneficial when sintering with low-melting point components, such as Al, as it won't be pressed out of the green body during reactive sintering.

The desired amount of powder mixture is pre-pressed to a green body with a cold press (Laboratory Press Model 3853-0, Carver, USA) at 30 MPa. PLS is performed with an alumina tube furnace (LTF 16/75/610, Lenton, England). The green body is placed in an alumina boat in the centre of the alumina tube. A heating rate of 5 °C/min was used for all PLS experiments, and a cooling rate of max. 10 °C/min. A flowing argon (>5 N) atmosphere (0.5 l/min) was maintained within the PLS furnace for all experiments.

Surface treatment and machining after sintering

The dense SPS samples are removed from the graphite mould, and the planar surface is grinded on a rotating grinding table using SiC paper starting with 220 grit down to 2500 grit. A diamond grinding disk was used as a first step in some cases to grind off all graphite contamination. Depending on the desired surface smoothness the sample was polished in a maximum of three polishing steps with ethanol and diamond paste of 3, 1, and ¼ µm.

In order to obtain samples with the correct dimensions for Thermal gravimetric analysis (TGA) and for crack-healing testing, MAX phase samples were machined by spark erosion wire-cutting (locally the temperature increases above T_{melt} of the MAX phase sample during cutting) with a brass wire of 0.25 or 0.10 mm thickness, under constant flow of demineralised water for cooling. Cutting speeds of 1 to 1.5 mm per minute are reached.

In cases where the MAX phase tablet had to be cut in smaller pieces without attaining specific dimensions after cutting, it was sawn in smaller pieces (quarters) with a diamond disk saw (IsoMet low speed saw, Buehler, USA).

PLS samples are very porous after sintering and therefore do not remain mechanically stable during grinding, polishing, or machining. PLS samples were therefore analysed by XRD without grinding and polishing. One sample has been pulverized with a pulverisette (P-0150, Fritsch, Germany). The powdered PLS sample was then further sintered by SPS. This is described in section 4.1.

3.2 Material characterization methods

X-ray diffractometry (XRD)

X-ray diffractometry (XRD) was used to determine the crystalline phases present in the powders and bulk samples. XRD is a non-destructive technique that reveals information about the crystallographic structures of solids. A monochromatic X-ray beam is impinged on the sample surface, and scattered by the atoms in the crystalline material. Constructive interference takes place for the scatter angles for which the path difference of electromagnetic waves scattered on different atomic planes is an integer amount of wavelengths. Constructive interference is detected

as an increased intensity of the scattered X-ray beam for certain angles between the X-ray source and the detector. The condition for constructive interference is described by Braggs law:

$$n\lambda = 2d\sin(\theta)$$

Where n is an integer, λ is the wavelength of the X-ray beam, d is the distance between two atomic planes, and Θ is the angle of incidence and reflection. A schematic of X-ray diffraction on the lattice planes of a crystalline solid is shown in Figure 11.

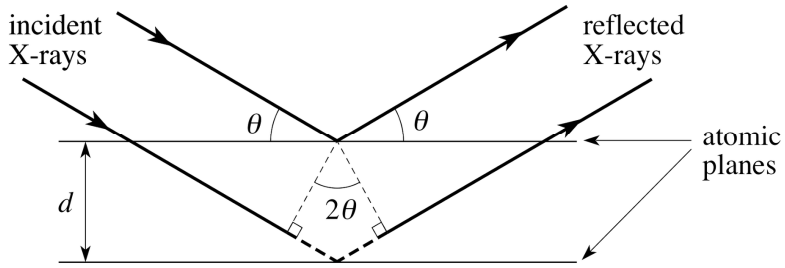

Figure 11: Schematic of X-ray diffraction on lattice planes [96].

An X-ray pattern is constructed from the data on the detected scattered X-rays , by plotting the counted X-rays against the measured angle (denoted by 2Θ). From the information on angles at which peaks in the X-ray pattern occur (e.g. angles of constructive interference), the interatomic distance of the atomic planes in the solid can be determined, and hence the crystallographic structure and the phases.

XRD experiments have been performed with a Bruker D8 Advance diffractometer (Bruker, Germany) using Bragg-Brentano geometry and Lynxeye position sensitive detector. Monochromatic Cu Kα radiation is used as X-ray source. Further parameters for recording of the diffractograms are: V12° divergence slit; scatter screen height of 5 mm; power of 45 kV times 40 mA; spinning sample; 2Θ range of 10° to 130°; step size of 0.034°; counting time per step of 1 s. Data evaluation was performed with various versions of Bruker software Diffrac.EVA (version 3.1, 4.0, and 4.1).XRD analysis with these parameters was performed on dense bulk samples as well as powders (Ta_2AlC, Ta, TaC).

Scanning electron microscopy (SEM) with Energy dispersive spectroscopy (EDS)

Analysis of microstructure and morphology of bulk and powder samples has been done using scanning electron microscopy (SEM). A high energy primary electron beam (generally between 200 eV and 30 keV) scans an area on the sample surface line by line. Interactions of the primary electron beam with atoms in the sample generate various electron signals which are partly reflected into the detector and amplified to generate an image corresponding to the measured electron intensity.

A schematic of the different signals generated due to interaction between the primary electron beam and the atoms in the sample is shown in Figure 12. The depth of the reaction volume depends on the material and the energy of the primary electrons. All signals relevant for this work are briefly explained below.

Backscattered electrons (BSE) are generated after elastic collision of primary electrons with atoms in the sample. A higher atomic number (Z) results in a higher yield of BSE electrons, because the density of collision sites (i.e. electronic density) is higher. This means that a material consisting of heavier elements looks relatively bright in a BSE SEM image. Secondary electrons (SE) are generated by inelastic collisions of primary electrons with the sample, which ionizes atoms in the sample, hence releasing SE's. SE's generally have much lower energy than BSE's, and therefore have a shorter mean free path within the sample material and a smaller detected interaction volume. Hence SE images have the highest spatial resolution, whereas BSE images shows more material specific information due to higher contrast between regions with a different elemental stoichiometry.

The SEM used for this work is equipped with an energy dispersive spectrometer (EDS), which allows for rapid qualitative and quantitative composition analysis via X-ray microanalysis. Characteristic X-rays are generated when atoms with ionized inner electron-shells relaxes, and a photon is released. Characteristic X-rays are a by-product of the image generating SE and BSE electrons. They are element specific, and thus give information about the local chemical composition of the sample. Their detected interaction volume is higher than that of SE and BSE electrons.

SEM observations were performed on the JSM 6500F (JEOL Ltd., Tokyo, Japan) equipped with the Thermoscientific Ultra dry EDS detector. Noran System Seven software was used for acquisition and analysis of EDS data. Point analysis and linescans have been performed with EDS on various samples.

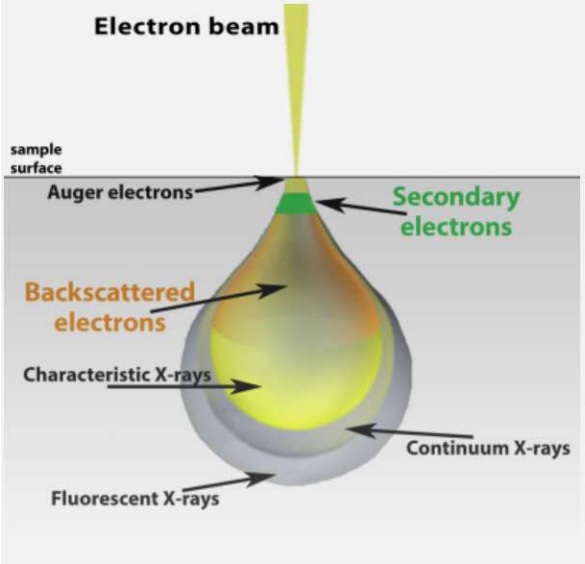

Figure 12: Schematic of the signals generated in SEM [97].

Electron probe X-ray microanalysis (EPMA) with wavelength-dispersive spectroscopy (WDS)

More accurate quantitative and qualitative analysis of the local composition profile on oxide scales of oxidized dense bulk Ta-Al-C MAX phase samples, have been obtained via electron probe X-ray microanalysis (EPMA) using wavelength-dispersive spectroscopy (WDS). Element specific X-rays are produced in the same manner as with EDS (high energy electron beam), but WDS only counts X-rays with one specific wavelength, instead of analysing the spectrum of all wavelengths detected, such as with EDS. In this way the presence of particular elements can be separately analysed.

The measurements were performed with a JEOL JXA 8900R microprobe using an electron beam with energy of 10 keV and beam current of 50 nA employing Wavelength Dispersive Spectrometry (WDS). The composition at each analysis location of the sample was determined using the X-ray intensities of the constituent elements after background correction relative to the corresponding intensities of reference materials. The thus obtained intensity ratios were processed with a matrix correction program CITZAF [1]. An airjet was used to decontaminate the sample surface of carbonaceous substances. The background pressure increased from 4.10-6 to 6.10-5 mbar. The points of analysis were picked along line scans and points and involved the elements C, O, Al and Ta, see details in Table 14.

Table 14: The energy (keV), Detection Limit (ppm), and counting error (wt-%) for each of the elements analysed using WDS.

Element, X-ray line	Energy (keV)	Detection Limit (ppm)	Counting error (wt-%)
Carbon, C Kα	0.282	300	0.1
Oxygen, O Kα	0.525	250	0.1
Aluminium, Al Kα	1.487	50	0.05
Tantalum, Ta Mα	1.710	100	0.1

X-ray photoelectron spectroscopy (XPS)

X-ray photoelectron spectroscopy (XPS) was performed on the surface of oxidized dense bulk Ta-Al-C MAX phase samples to obtain information on the bonding energies Ta, Al, and O within the oxidized surface layer. Low energy monochromatic X-rays irradiate the sample surface and excite electrons on the sample surface. An electron is emitted from the surface in case its bonding energy is lower than the energy of the X-ray. Only electrons which are emitted in close proximity of the sample surface – typically 0 to 10 nm (e.g. about 20 atomic layers) – have enough energy to reach the sample surface and escape. The bonding energy of the electron orbital which the escaped electrons were in, is determined via their kinetic energy: their kinetic energy is equal to the energy of the incident X-ray beam minus the bonding energy. XPS allows for counting of photoelectrons with a specific voltage separately, which is achieved by variation of the voltage between two separated curved plates that place the electrons in a specific orbit towards the detector. The resulting XPS pattern shows the count versus bonding energy for a range of bonding energies. The sensitivity of the detector allows for detection of very slight electron energy shifts.

The surfaces after oxidation were analysed with X-ray photoelectron spectroscopy XPS (PHI 5400 ESCA, USA) using non monochromatic Mg anode X-ray source (Mg Kα = 1253.6 eV). The Photoelectrons emitted from the samples were observed through an input lens at an angle of 45° with respect to the sample surface normal. The elliptic analysis area amounts 1.1x1.6 mm. The photoelectron spectra were recorded using a spherical capacitor analyser (SCA) operated with a pass energy of 71.55 eV, in the binding energy range of 0-1000 eV with a step size of 0.25 eV and a dwell time of 2 s per step. The energy scale of the SCA was calibrated according to the procedure described in [American Society for Testing and Materials, Surface and Interface Analysis, 17 (1991) 889]. Prior to the XPS measurements, surface contamination was removed by mild ion sputtering for 20 min using a 3 keV Ar^+ beam scanning a sample surface area of 3 × 3 mm.

3.3 Determination of sample hardness and density

Vickers micro hardness indentation

Vickers micro hardness indention was performed on dense bulk Ta-Al-C MAX phase samples to compare their hardness with theoretical and experimental values from literature. The hardness of a material is a quantification of its ability to resist plastic deformation. The load over the surface area of indentation determines the hardness number. For the method of Vickers hardness indentation, the calculation of the hardness is independent of the size of the indenter, and material. A standard diamond indenter with a square-based pyramid geometry (angle horizontal to plane is 22°) is used to produce indents. Hardness is measured in the unit 'HV', e.g. Vickers Pyramid Number, and determined by the ratio of the force applied to the indenter (F) over the surface area of the indentation (A). Based on the standard shape of the indenter, the surface area of indentation is defined as follows [98]:

$$A = \frac{d^2}{2\sin(136°/2)} \approx \frac{d^2}{1.8544}$$

Where d is the diagonal length of the indentation, in mm. HV in GPa is then calculated by:

$$\mathrm{HV} = \frac{\mathrm{F}}{\mathrm{A}} \approx \frac{1.8544 \cdot \mathrm{F} \cdot \mathrm{g}}{\mathrm{d}^2 \cdot 1000} \approx \frac{0.01819 \cdot \mathrm{F}}{\mathrm{d}^2}$$

Where F is the force in N, and g is the standard gravity of 9.80665 m/s^2.
A schematic of Vickers indentation and the measurement of the diagonals of the resulting indent is shown in Figure 13.

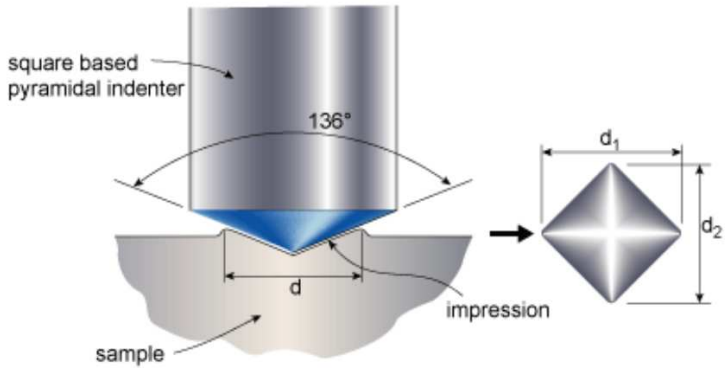

Figure 13: Schematic of Vickers indentation and measurement of the indent diagonals [99].

The equipment used for Vickers micro indentation is the DuraScan 70 microhardness tester from Struers, Denmark, which is operated with the Ecos Workflow Software. HV1 was used for all indentations performed, meaning that a load of 1 kgf was applied on the indenter during indentation. Indents were placed with sufficient distance to each other, e.g. 5 times the diagonal distance, and 2.5x diagonal length to the sample edges. For small sample pieces, no more than 5 indents could fit on the sample. An overview of all successful indentations given in section 4.2.3.

Archimedes method for density measurement

Archimedes density measurements were performed on dense bulk Ta-Al-C MAX phase samples to compare their density with theoretical and experimental values from literature. If the density of a fluid is known, the volume of the amount of displaced fluid can be readily calculated (volume = mass/density), and is identical to the volume of the immersed solid body. The density of the solid body can then be calculated by dividing this volume by the dry mass of the solid body:

$$\rho_{\text{sample}} = \frac{\text{A}}{\text{P}} \cdot \rho_{\text{water}}$$

Where ρ_{sample} and ρ_{water} represent the density of the sample and water respectively in g/cm^3. A is the mass of the dry sample in air in grams, P is the buoyancy of the sample in grams. A and P are measured experimentally for each sample.

Density measurements were performed with density determination kit and analytical balance (Kit #33360, type AG-204, Mettler Toledo, Switzerland). The density of all samples was measured subsequently and once per sample. For most samples, the density measurement was not performed on the full sample, but on a remaining piece after cutting the sample for other purposes (such as the production of TGA samples). In some cases the piece used for density calculation was very small, with a surface area below 12 mm^2, and a thickness of 4 mm.

3.4 Methods to asses oxidation reactions and kinetics

Differential thermal analysis (DTA)

To get insight in the reactions taking place in Ta-Al-C MAX phase during oxidation, differential thermal analysis (DTA) was performed on Ta_2AlC and mixed Ta_2AlC with Ta_4AlC_3 powders. For comparison of the oxidation reactions, DTA was also performed on Ta and TaC powder.

During DTA, the temperature difference between the sample and an inert reference sample (commonly an empty alumina crucible) is measured by two thermocouples, during heating. The sample and inert reference are located in the same furnace (e.g. same conditions) under controlled atmosphere, and subjected to a constant heating rate. If a chemical reactions takes place in the sample, the change of its enthalpy will cause a temporary and significant temperature difference between the sample and reference. The measured DTA signal ($T_{sample} – T_{reference} = \Delta T$) shows by convention a positive value for an exothermic reaction in the sample, and a negative value for an endothermic reaction [100].

The main components of DTA equipment are a programmable furnace with atmosphere control, recording, sample holder and inert sample containers, and thermocouples. A schematic of the DTA equipment is shown in Figure 14.

All DTA experiments for this work have been conducted using Setsys Evolution equipment (1750, Setaram, France), in an artificial air atmosphere of 20 % oxygen (10 ml/minute) and 80 % nitrogen (40 ml/minute) (>5N). DTA is performed on Ta_2AlC, Ta, and TaC, all in powdered form. The powder was heated from T_{room} (20 °C) until 800 or 1200 °C with a heating rate of 1, 2, 5, 10, or 15 °C/min. During DTA the powder is contained in an alumina crucible, and an empty alumina crucible is used as reference sample. Additional to the measurement of the temperature difference between sample and reference, the weight gain of the powder during oxidation is recorded for each DTA experiment performed. Weight gain is measured with a precision balance located within the instrument.

Ta-Al-C MAX phase powder was made from dense bulk SPS samples with a dremel (mod. 395, type 5, Dremel, USA), with a range of 10.000 to 37.000 rpm. Moderate to high speed was used to powder the samples. A clean diamond tip was used during drilling to avoid contamination of the powder. For each DTA run approximately 30 mg of powder was used. The powder was weighted with a high precision balance (type M5 5A, Mettler Toledo, USA). The powder was weighted before and after each DTA experiment, in order to verify the total weight gain as recorded with the DTA equipment.

The grain size distribution of the Ta and TaC powder was determined with a laser sizer (Master Sizer X, Malvern Instruments, UK). Laser diffraction from a laser beam that passes through a dispersed particulate sample is analysed to calculate the particle size. Higher grain size in the powder leads to a higher scatter angle of the monochromatic laser beam [101]. Visual inspection of the grain size of the MAX phase powders was performed by SEM observation.

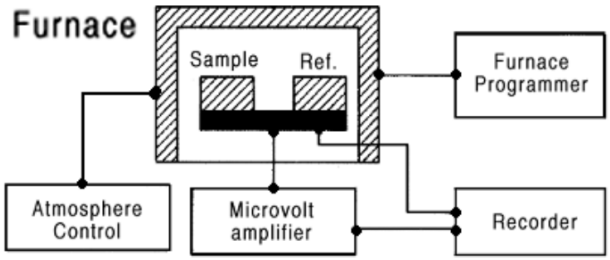

Figure 14: Schematic of differential thermal analysis instrumentation [102].

Determination of activation energy from variation of DTA peak temperature with heating rate

In case of an elementary oxidation reaction (e.g. a single transition without intermediates), the temperature at which the peak in the DTA signal is observed, changes when a different heating rate is used for the same material. Kissinger [100], amongst others, has derived a relation between the variation in peak temperature and the activation energy of the reaction for elementary reactions following first-order kinetics. In this work, the activation energies of oxidation reactions taking place in Ta_2AlC, Ta, and TaC powder was estimated from DTA data making use of the following equation, as taken from [100]:

$$\ln\left(\frac{\beta}{T^2}\right) + \frac{E_a}{R} \cdot \frac{1}{T} = constant$$

where β = heating rate, T = peak temperature, R = gas constant, E_a = activation energy. In this work, it will be named the 'Kissinger equation'.
For each heating rate, the peak temperature of the observed DTA peaks is estimated. A scatter plot is made of $\ln(\beta/T^2)$ versus 1/T, including each heating rate. The slope of the linear fit through these points is E_a/R, as follows from the Kissinger equation.
Additionally, Kissinger points can be calculated from the weight gain curve, recorded during DTA measurement. The maximum of the weight gain derivative corresponds to the elementary reaction peak temperature, allowing a comparative calculation using the Kissinger equation [100]. Similarity in the calculated value of E_a via both methods is explained by the fact that the weight gain of the powder upon oxidation changes most at the same temperature that the reaction is at its 'height', during which a peak in the heat flow is also observed [100]. The analysis described above will be named 'Kissinger analysis' in this work.

Thermogravimetric analysis (TGA)

Thermogravimetric analysis (TGA) was performed to derive the oxidation kinetics of dense bulk Ta-Al-C MAX phase in the temperature range of 600 – 800 °C. The TGA performed in this work allows for determination of changes in the physical and chemical properties of materials at elevated temperatures, by very accurate measurement of weight changes in the sample over time. The main components of the TGA equipment are a programmable furnace with atmosphere control and the sample suspension consisting of a sapphire rod, attached to a high precision

balance. A schematic of the TGA equipment is shown in Figure 15. Additionally to the schematic shown in Figure 15, the instrumentation used for this work is an advanced dual furnace (TAG, Setaram, France). The dual furnace allows for automatic correction of buoyancy effects caused by the gas flow, by conducting simultaneous identical heat treatment on an inert alumina reference sample with the same volume as the dense bulk MAX phase sample. The measured weight change of the inert reference sample is subtracted from the measured weight gain of the MAX phase sample.

The TGA performed in this work has advantages over weight gain measurement via a stop and go principle, where the sample has to be taken out of the furnace to manually measure the weight gain. Anasori *et al.* [103] and Basu *et al.* [104] reported to have applied the stop and go method to study the oxidation kinetics of Ti_2GeC and Ti_2AlC, respectively. TGA requires less time between measurements, and no sample handling and intermediate cooling (which could damage the oxide scale) of the sample has to take place. Therefore, the equipment used for this work achieves higher accuracy and less error in the weight gain measurement.

Dense bulk samples of Ta_2AlC and mixed Ta-Al-C MAX phase were oxidized isothermally for 10 hours at 600, 700, and 800 °C respectively, in dry artificial air of 20 % oxygen (10 ml/minute) and 80 % nitrogen (40 ml/minute) (>5 N).

The MAX phase sample and reference sample are heated with 10 °C/min in flowing N_2 atmosphere (50 ml/min; >5 N), to prevent any oxidation before the isothermal holding temperature is reached. When $T_{isotherm}$ is reached, the air flow is changed to 40 ml/min N_2 and 10 ml/min O_2. After 10 hours isothermal holding, the furnaces are cooled to T_{room} with 10 °C/min in flowing N_2 atmosphere (50 ml/min).

Before the start of each TGA, both furnaces are flushed two times to get rid of any oxygen or moisture, by alternatingly creating a vacuum of 10^{-1} mbar and flushing with 200 ml/minute of nitrogen. During flushing, the oxygen partial pressure is measured with mass spectrometry, and it was found that a minimal O_2 signal is reached after 30 to 60 minutes of flushing with N_2. After flushing, a N_2 flow of 50 ml/minute is established. The precision balance with the MAX phase and reference sample hanging from both sides on sapphire rods is stabilized under gas flow to reach a dTG value of 0.010 mg/min or lower and tared before the program is started.

TGA samples of the desired dimension have been produced from dense bulk SPS samples by spark erosion wire-cutting (see description on p.3 under ‘Surface treatment and machining after sintering’). After wire-cutting, possible contamination was grinded off from all samples sides with 1200 grit SiC grinding paper.

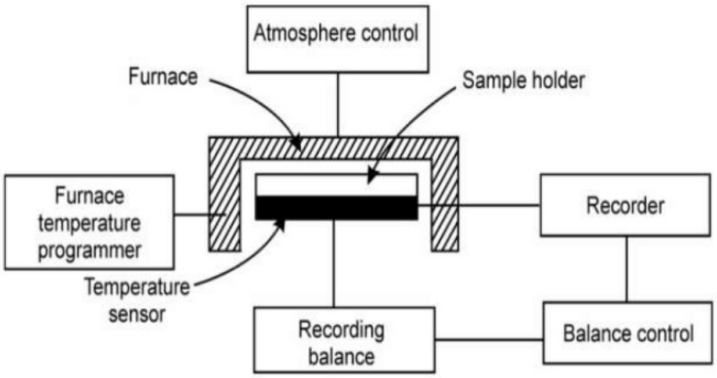

Figure 15: Schematic of TGA equipment [102] .

Calculation of Relative Volume Expansion (RVE) upon oxidation

The relative volume expansion (RVE) upon oxidation has been calculated in section 5.2 for full oxidation of Ta_2AlC and Ta_4AlC_3 to Ta_2O_5 and a mix of Ta_2O_5 and $TaAlO_4$ respectively. The RVE upon oxidation is calculated by dividing the molar volume of the oxides by the molar volume of the bulk material corresponding to the same number of the element(s) that is(are) oxidized in one molar volume of oxide [6]:

$$RVE = \frac{V_{oxide}}{V_{bulk\ material}}$$

The molar volume of the oxide and bulk material is determined from dividing the molar mass by mass density.

The calculation of the RVE upon oxidation for MAX phase as used in this work, is an adaption of the calculation of the Pilling-Bedworth ratio (PBR) which was originally used for corrosion of metals [105]. A PBR higher than 1 usually correctly indicates the formation of compressive stresses within the oxide scale upon oxidation, as the material has to expand upon oxidation, but this expansion is constraint at the oxide/bulk interface in case of good adhesion between bulk material and oxide.

3.5 Assessing self-healing potential of Ta-Al-C MAX phase

Self-Healing quantification by mechanical testing

The self-healing potential of Ta-Al-C MAX phase was tested by formation, oxidation, and re-opening of a micro-crack within dense bulk MAX phase, by driving a wedge into a dense Ta-Al-C MAX phase sample of specific geometry as shown in Figure 16 [106]. The geometry allows for self-alignment during loading when the sample is placed on a flat plate (due to its curved base), and formation of a crack in the chevron notch. The chevron notch tip is located at a 10 mm depth from the top of the sample. The load bearing capability of the sample with micro-crack before and after oxidation was measured and compared, to see if the load bearing limit of the sample was

increased by healing of the crack, after oxidation. The load versus displacement curve for crack initiation and formation, and for re-opening after oxidation are given in section 4.6.

This method was chosen over alternative methods for crack formation and testing of (residual) strength as it shows good repeatability, good control of the location of crack formation and crack path and width, and allows for multiple tests on the same sample (re-opening of oxidized crack). Three-point bending is the standard method used to test material strength in ceramics, but requires the formation of controlled pre-cracks (which is hard to achieve in ceramics) and is sensitive to surface flaws. Lie *et al.* [15] made use of three-point bending to test self-healing in Ti_2AlC MAX phase, and used different samples to test the strength of virgin, pre-damaged, and healed Ti_2AlC. In this work the virgin strength and strength after oxidation have been determined for the same sample. Other alternative methods to induce cracking in MAX phase samples are indentation, quenching, and low perpendicular velocity impact. None of these methods allow for precise control on the location of crack formation, and hence the sample can't be loaded in a straightforward manner after oxidation to test sample strength.

To create and re-open a micro-crack in controlled manner, a dense Ta-Al-C MAX phase sample was loaded with a 10 kN load cell fitted on an electro-mechanical load frame (Instron, type 5500R). The sample geometry is referred to as 'wedge sample' in this work, and shown in Figure 16. For the wedge sample used in this work, W, HW, B, and BN are respectively 29, 30, 3, and 1.5 mm. During loading a wedge is lowered into the centre opening above the chevron notch tip until a pre-load of 10 N is reached, after which the wedge is further lowered with a constant displacement of 0.1 mm/s. A maximum load is reached, after which crack initiation takes place and the load starts to drop. When a load drop of 50% is recorded, the test is automatically stopped and the wedge is retracted. This is done to avoid breaking the wedge sample in halves by crack formation down to the base of the sample. A schematic of the setup with the wedge sample located under the wedge in the load cell is shown in Figure 17.

Optical microscopy was used to observe of relatively large surface details on the sample surface, which was done for the wedge sample before and after crack formation and oxidation. An optical microscope from Keyence was used (Keyence VHX-5000 using a VHZ250R 250x-2500x lens, Keyence, Japan), which allowed for automated image stitching, and hence quick imaging of entire sample surface at magnification and high resolution. The optical microscopy images of the wedge sample were used to get an overview of the positioning of the microcrack, and locations of oxidation after isothermal holding at 600 °C for 16 hours in flowing air.

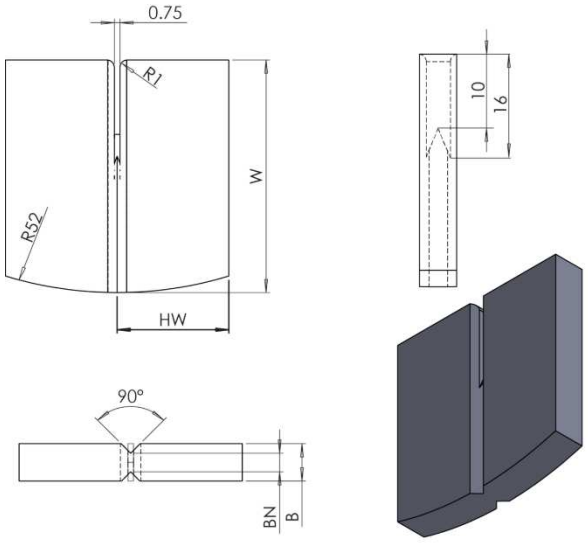

Figure 16: Dimensions of wedge sample [106].

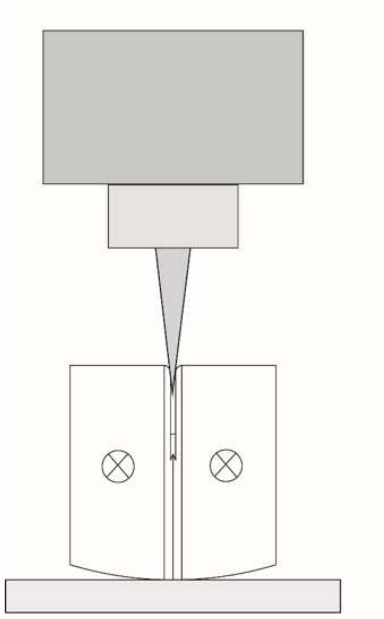

Figure 17: Schematic of the setup for loading of the wedge sample [106].

4. Results

4.1 Synthesis

Pressure-Less Sintering (PLS) and Spark Plasma Sintering (SPS) were used to prepare Ta-Al-C MAX phase. An overview is given of the different synthesis attempts of dense bulk Ta-Al-C MAX phase, in order to give insight in the important factors for synthesis of mainly single phased dense bulk Ta_2AlC. These factors are: stoichiometry of powder mixture, powder type, temperature, pressure, and atmosphere. Changes in sintering method, powder mix composition, and temperature and pressure profile during sintering are described. The main phases as identified by XRD analysis are stated.

Pressure-less sintering

Three attempts to synthesize Ta_2AlC MAX phase with pressure-less sintering have been performed. Before sintering, a mixture of elemental tantalum, aluminium, and carbon powder was pre-pressed with 300 MPa to form a tablet. The tablet was heated with a rate of 5 °C/min, and held at the desired sinter temperature for 1 hour, after which the furnace is cooled with a maximum rate of 10 °C/min. Heating, sintering, and cooling takes place under flowing argon atmosphere. The powder mix composition, sinter temperature, and phases formed (as identified by XRD analysis) for all three attempts are shown in Table 15. If one identified phase shows significantly higher peaks in the XRD pattern than the other identified phases, it is named 'main phase', see Table 15.

None of the pressure-less sintering attempts resulted in pure MAX phase material. At a sinter temperature of 1200 °C no MAX phase forms. Increasing the temperature to 1400 and 1500 °C results in formation of MAX phase, where Ta_2AlC only forms at 1500 °C, and Ta_4AlC_3 forms at both sintering temperatures. However, a significant amount of tantalum-carbides and tantalum-aluminium intermetallic is also formed (see Table 15).

Table 15: Overview of synthesis settings and results by pressure-less sintering

Number	Powder mix composition (Ta : Al : C)	Sinter temperature (°C)	Phases formed, following from XRD analysis
1	2: 1.15 : 1	1400	Main phase: Ta_4AlC_3 Minor phases: $TaAl_3$; $TaC_{0.81}$
2	2: 1.15 : 1	1200	Ta_2C; Ta_5Al_3C; $Ta_{0.97}O_2$; $AlTa_2$ & s-$AlTa_2$ (no clear 'main' phase)
3	2: 1.6 : 1	1500	Main phases: TaC; Ta_2AlC Minor phases: Ta_4AlC_3; $TaAl_3$

Spark Plasma Sintering

Spark Plasma Sintering (SPS) was performed using different starting powders, powder stoichiometry's, and heating profiles. Powder mixtures consisting of elemental powders, as well

as carbides, were tested in the search for the ideal conditions to synthesize dense bulk Ta_2AlC MAX phase.

SPS synthesis using Ta, Al_4C_3, and C

A powder mix of Ta, Al_4C_3, and C with the composition Ta : Al_4C_3 : C = 2 : 0.25 : 0.25 was sintered in argon atmosphere. This mixing composition corresponds to a stoichiometry of Ta : Al : C = 2 : 1 : 1. The powder mix was heated with 50 °C/min to a sintering temperature of 1300 °C. The pressure was increased to 50 MPa (corresponding to a force of 16 kN for an SPS sample with a diameter of 20 mm), which is reached before the start of sintering at 1300 °C. After 1 hour of sintering at 1300 °C and 50 MPa, temperature and pressure are respectively decreased to T_{room} with 100 °C/min and 16 MPa (corresponding to a minimum force of 5 kN) with 1.5 kN/min. Figure 18 shows the profile of the set temperature and set force during synthesis. The set temperature could not be monitored below 500 °C, hence the temperature decrease to T_{room} is not visible.

The black curve shows the average relative piston travel in mm, as compared to the piston position at the start of the SPS program, which is noted as 0 mm. As the piston moves during synthesis, the sample is densified. From Figure 18 it can be seen that most densification takes place when the pressure and temperature are increasing: the average relative piston travel increases from 0 to approximately 2.75 mm. During sintering, the average relative piston travel further increases to approximately 3.25 mm.

As the method of SPS is used for reaction sintering in this work, the densification of the powder sample during heating and sintering is attributed to the occurrence of chemical reactions between powder constituents, presumably in combination with conventional sintering of solid-state particles and possibly also liquid aluminium. No study has been made of the microstructural evolution over time during heating and sintering, which could be done by intermediately stopping the SPS program and observing of sample microstructure [107].

The XRD pattern and fitting after synthesis is shown in Figure 19. The phases identified by XRD analysis are Ta_2C; Ta_4C_3; Ta_5Al_3; $Ta_{0.6}Al_{0.4}$; Ta_3Al_2C. The relatively highest peaks of the XRD pattern correspond to Ta_2C; Ta_4C_3. No MAX phase was identified.

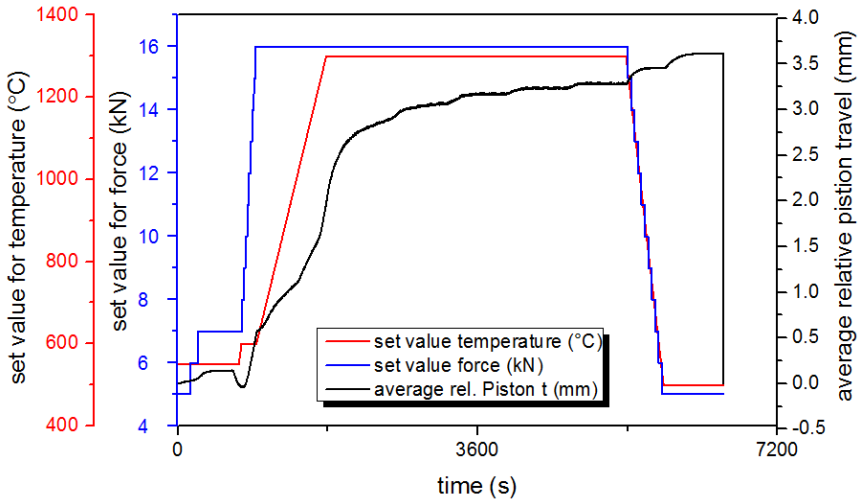

Figure 18: SPS synthesis program for mix of Ta, Al_4C_3, C - set values and measured average piston travel versus time.

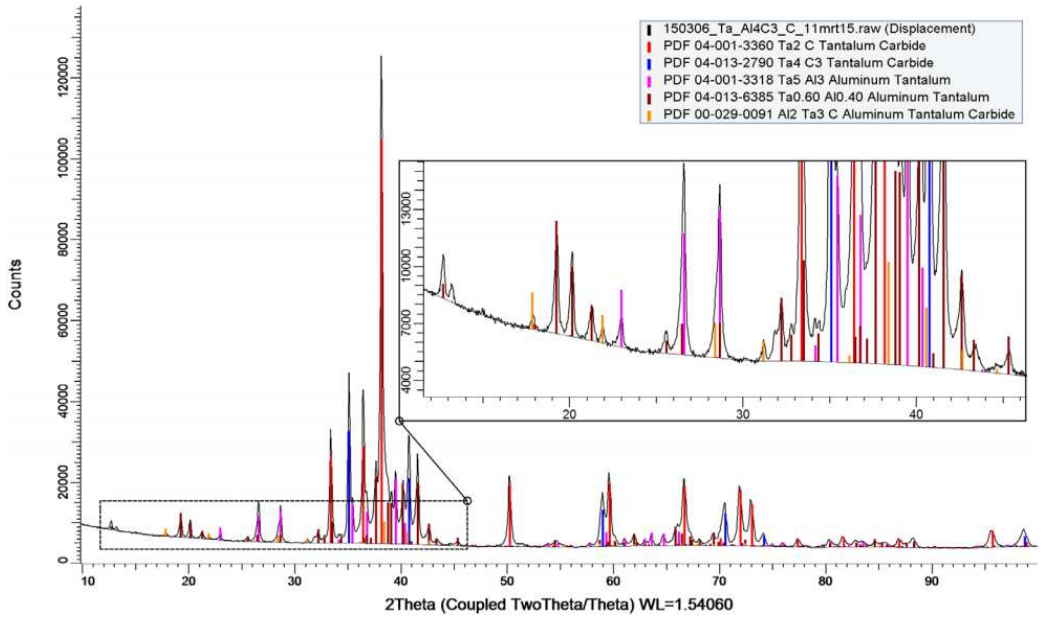

Figure 19: XRD pattern and fit for SPS sample from powder mix Ta : Al_4C_3 : C = 2 : 0.25 : 0.25, sintered at 1300 °C and 50 MPa in argon for 1 hour.

SPS sintering of pulverized PLS sample

A two-step process was tested to see if the combination of pressure-less sintering followed by SPS can lead to fully dense pure MAX phase, as demonstrated for Cr_2AlC [108]. The sample resulting from pressure-less sintering at 1500 °C with a starting composition of Ta : Al : C = 2: 1.6 : 1 (see Table 15) was pulverized and further sintered by SPS. Figure 20 shows the set values of the SPS program for temperature, force, and the relative piston travel versus time. Temperature and pressure are increased respectively until 1500 °C and 50 MPa with 80 °C/min and 5.5 kN/min. The sample is sintered at 1500 °C and 50 MPa for 2 hours instead of 1 hour, to allow all solid state reactions to take place. SPSing took place in vacuum (≥ 0.77 mbar). As can be seen in Figure 20 from the curve of average relative piston travel, most densification of the pulverized PLS sample takes place when temperature and pressure are increasing, and hardly any further densification takes place during sintering at 1500 °C.

The XRD pattern and fitting after synthesis is shown in Figure 21. The phases identified by XRD analysis are Ta_2C; Ta_4C_3; Ta_5Al_3; $Ta_{0.6}Al_{0.4}$; Ta_3Al_2C. The relatively highest peaks of the XRD pattern correspond to Ta_2C and Ta_4C_3. No MAX phase is present anymore.

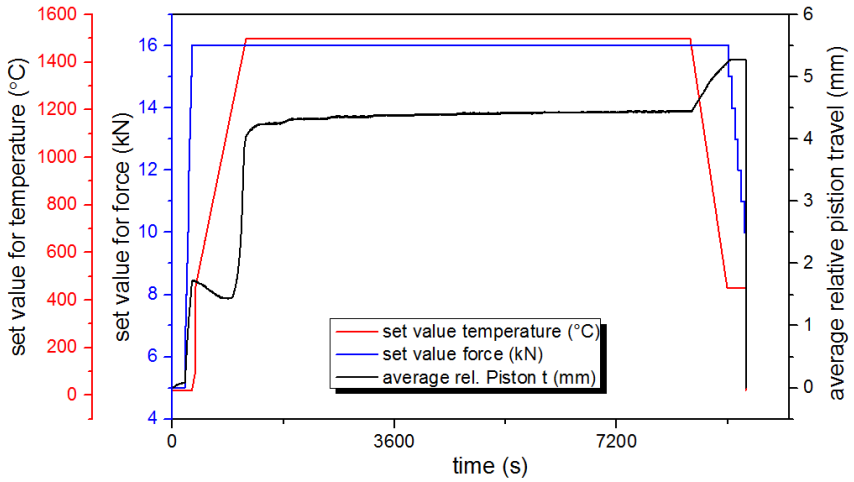

Figure 20: SPS synthesis program for pulverized PLS sample - set values and measured average piston travel versus time.

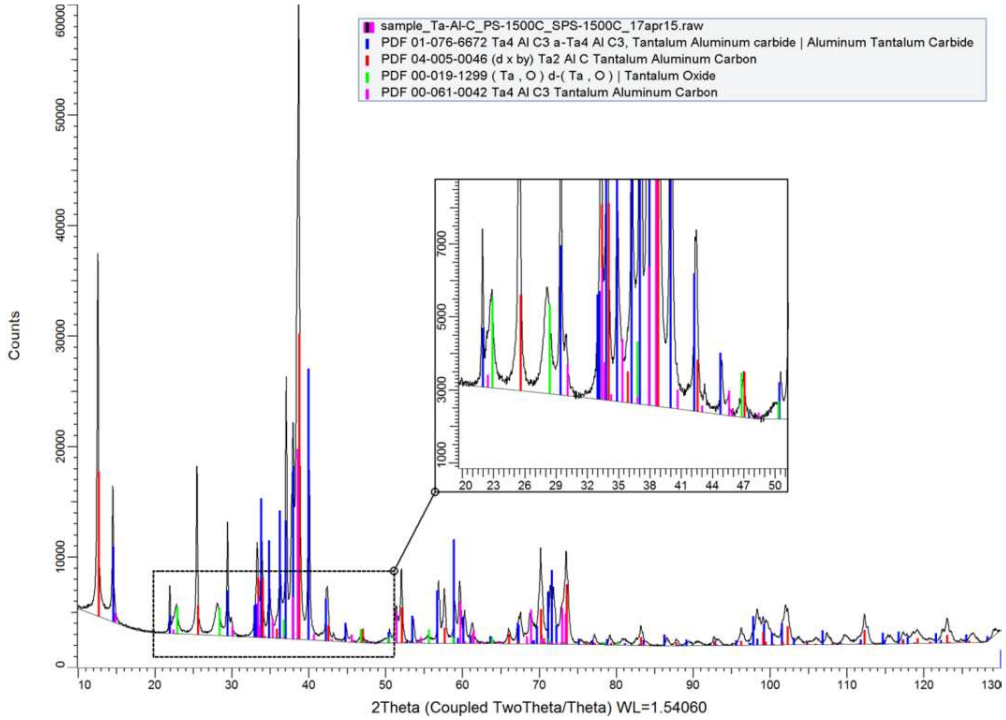

Figure 21: XRD pattern and fit for SPS sample from pulverized PLS sample, sintered at 1500 °C and 50 MPa in argon for 2 hours.

<u>SPS synthesis from elemental powders</u>

Further synthesis attempts have been performed with powder mixes of elemental powders of Ta, Al, and C. An overview of the important process parameters for all SPS attempts performed with an elemental powder mix with the composition Ta : Al : C = 2 : 1.2 : 1 is shown in Table 16. Additionally, the phases identified by XRD analysis after synthesis are stated in Table 16 for each sample. In case a sample consists of mainly one of the identified phases – which can be deduced from relative peak height within the XRD pattern – this phase is stated as ‘main’ phase in Table

16. Other phases are stated as ‘minor’ (in case of 1 extra phase) or ‘other’ (in case of multiple extra phases). The XRD patterns of all samples shown in Table 16 can be found elsewhere. [1]

The sample names are given by the date of syntheses. The main characteristics of the set temperature and set force profile is shown in Figure 22, which corresponds to synthesis of sample 150408. Further description of the synthesis process from elemental powders corresponds to the settings as shown in Figure 22 for sample 150408.

In contrast to the previously described sintering attempts by SPS, an intermediate heating step was added to allow pre-reaction of molten Al to form a solid intermetallic with Ta. The powder mix is heated from room temperature to 750 °C in 0.5 minute, and is held at this temperature for 5 minutes, before it is heated with a slower rate of 85 °C/min to the final sinter temperature of 1500 °C. Before heating, the force is maximized to 16 kN, corresponding to a pressure of 50 MPa on the green body. This densifies the pre-reacted powder mix as much as possible before any temperature is applied. The pressure is then minimized to 16 MPa (force of 5 kN) before intermediate holding at 750 °C, in order to minimize the amount of molten Al being squeezed out of the powder mixture as much as possible. In case a significant fraction of aluminium would leak out of the powder mixture, the remaining composition of the powder mix does not contain enough aluminium to facilitate the synthesis a (nearly) single-phase Ta_2AlC MAX phase sample. Aluminium leakage also damages the sides of the graphite die and punches. The sample (sample 150408) is sintered at 1500 °C and 50 MPa for 30 minutes, after which the temperature and pressure are decreased to respectively T_{room} and 16 MPa.

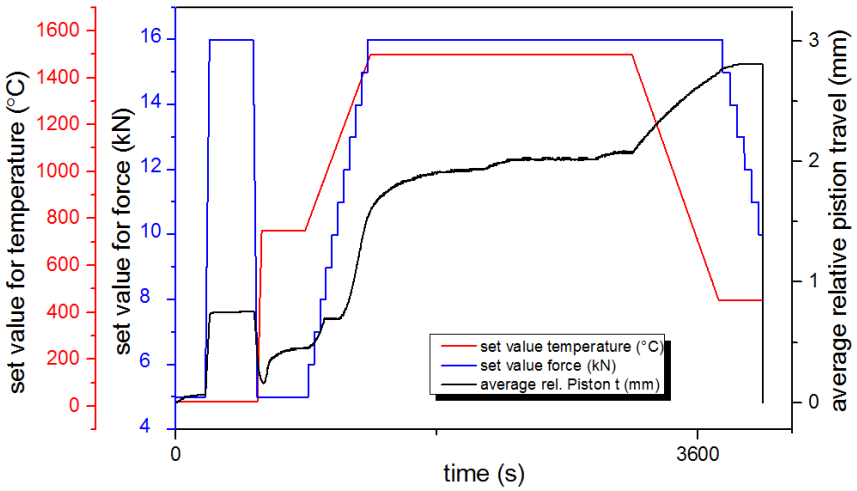

Figure 22: SPS synthesis program for elemental powder mix, corresponding to sample 150408 - set values and measured average piston travel versus time.

It was found from experiments and literature [108-110] that leakage and evaporation of molten Al cannot be completely avoided, and hence in all cases some extra Al compared to the precise

[1] Appendix 1 – Full sample overview of all synthesis attempts: XRD patterns & microstructure as observed by SEM

stoichiometry for the formation of Ta_2AlC (which is Ta : Al : C = 2 : 1 : 1) has been added to the elemental powder mix to compensate for this.

The average relative piston travel (see Figure 22) shows densification from approximately 0 to 0.75 mm during cold pre-pressing (before the intermediate heating step). After decreasing the pressure to 16 MPa, the powder mixture expands and the pistons travels back to approximately 0.2 mm. Densification from 0.2 to 0.5 mm takes place during intermediate holding at 750 °C. Densification from 0.5 to 1.75 mm takes place during heating until the sintering temperature is reached. During sintering the sample is densified by 0.25 mm.

Table 16: Overview SPS parameters for synthesis from elemental powders with composition Ta : Al : C = 2 : 1.2 : 1; all tests had a pre-press of 50MPa applied before heating and the heating rate of 85C/min was used between the intermediate holding step and sintering temperature.

Sample	**Heating**	**Intermediate holding**	**Sintering**	**Atmosphere**	**Phases identified by XRD**
150408	Rate: 1400 °C/min F = 5 kN	T = 750 °C F = 5 kN Holding time = 5 min	T = 1500 °C F = 16 kN Holding time = 30 min	Argon (pO_2 ≈ 1 ppb; pH_2O ≈ 1 ppm)	Main: Ta_2AlC Other: Ta_4AlC_3; TaO
150423	Rate: 1400 °C/min F = 5 kN	T = 750 °C F = 5 kN Holding time = 5 min	T = 1500 °C F = 16 kN Holding time = 30 min	Argon (pO_2 ≈ 1 ppb; pH_2O ≈ 1 ppm)	Main: Ta_2AlC, Ta_4AlC_3. Other: C, $TaAlO_4$
150604	Rate: 1400 °C/min F = 5 kN	T = 750 °C F = 5 kN Holding time = 5 min	T = 1500 °C F = 16 kN Holding time = 30 min	Vacuum	Ta_2AlC, Ta_4AlC_3 (mixed)
150721	Rate: 1400 °C/min F = 5 kN	T = 750 °C F = 5 kN Holding time = 5 min	T = 1500 °C F = 16 kN Holding time = 30 min	Vacuum	Ta_2AlC, Ta_4AlC_3 (mixed)
150814-I	**Rate 1**: 450 °C/min to 450 °C* **Rate 2**: 600 °C/min to 750 °C F = 5 kN	T = **700 °C** F = 5 kN Holding time = **15 min**	T = 1500 °C F = 16 kN Holding time = 30 min	Vacuum	Main: Ta_4AlC_3. Minor: Ta_2AlC
150814-II	Rate 1: 450 °C/min to 450 °C* Rate 2: 600 °C/min to 750 °C F = 5 kN	T = 700 °C F = 5 kN Holding time = 15 min	T = **1400 °C** F = 16 kN Holding time = 30 min	Vacuum	Main: Ta_2AlC. Minor: Ta_4AlC_3

150821-I	Rate 1: 450 °C/min to 450 °C* Rate 2: 600 °C/min to 750 °C F = 5 kN	T = 700 °C F = 5 kN Holding time = 15 min	T = 1400 °C F = 16 kN Holding time = 30 min	Vacuum	Main: Ta_2AlC. Minor: Ta_4AlC_3
150821-II	Rate 1: 450 °C/min to 450 °C* Rate 2: 600 °C/min to 750 °C F = 5 kN	T = 700 °C F = 5 kN Holding time = 15 min	T = 1400 °C F = 16 kN Holding time = 30 min	Vacuum	Main: Ta_2AlC. Minor: Ta_4AlC_3
150824	Rate 1: 450 °C/min to 450 °C* Rate 2: 600 °C/min to 750 °C F = 5 kN	T = 700 °C F = 5 kN Holding time = 15 min	T = 1400 °C F = 16 kN Holding time = 30 min	Vacuum	Main: Ta_2AlC Minor: Ta_4AlC_3
151109	Rate 1: 450 °C/min to 450 °C* Rate 2: 600 °C/min to 750 °C F = 5 kN	T = 700 °C F = 5 kN Holding time = 15 min	T = 1400 °C F = 16 kN Holding time = 30 min	Vacuum	Ta_2AlC, Ta_4AlC_3 (mixed)

* Internal feedback between the set temperature value and measure temperature value takes place via pyrometer, which does not register the temperature below 400 °C. Slower heating to 450 °C was added to give the pyrometer more time to register the temperature in order to avoid overshooting by mis-measurement.

4.2 Sample characterization

4.2.1 Sample overview

From the results in Table 16 it can be seen that dense bulk Ta-Al-C MAX phase samples have been successfully produced by SPSing of mixed elemental powders of Ta, Al, C in the mixing ratio 2 : 1.2 : 1. Some of these samples consist of a significant amount of Ta_2AlC and Ta_4AlC_3. Other samples consist mainly of Ta_2AlC. The former will be called ‘mixed’ material in this work, the latter ‘Ta_2AlC’ material Table 17 gives an overview of the samples that have been used for further research in this work, whether they are ‘mixed’ or predominantly single-phase ‘Ta_2AlC’, and what they have been used for. Characterization of the microstructure and determination of the hardness and density of the samples shown in Table 17 is described in this section.

Table 17: Overview of successfully synthesized dense bulk Ta-Al-C MAX phase samples by SPS.

Sample	Type	Used for
150423	mixed	Open furnace oxidation*
150604	mixed	TGA
150721	mixed	Vickers increasing hardness indentation
150814-II	Ta_2AlC	TGA, DTA powder, SEM cross-section
150821-I	Ta_2AlC	DTA powder, SEM cross-section
150824	Ta_2AlC	Crack healing attempt I, failed (40 mm wedge sample)
151109	mixed	Crack healing attempt II, successful (40 mm wedge sample)

* results are not described in this work, as these were preliminary tests for the TGA experiments

4.2.2 Ta-Al-C MAX phase microstructure

Typical microstructure mainly Ta_2AlC sample

A representative SEM backscatter image of the microstructure of the surface of a mainly single-phased Ta_2AlC samples is shown in Figure 23a. The section mainly consists of Ta_2AlC (light grey areas), with very minor Ta_4AlC_3 (darker grey areas). Internal oxides (black spots) are visible, dispersed within the microstructure. The approximate grain size in Ta_2AlC samples could not be determined from visual inspection of SEM images, as the microstructure looks more homogeneous than for the mixed samples and lacks contrast, due to the absence of the Ta_4AlC_3 fraction (see microstructure of mixed samples in Figure 24). No porosity is found in the microstructure.

A SEM backscatter image of intermetallic tantalum-aluminium impurities (dark grey areas) found when observing cross-sections of Ta_2AlC samples is shown in Figure 23b. Quantitative X-ray microanalysis with EPMA has shown that the chemical composition of the intermetallic phase most likely corresponds to Al_3Ta. The atom fractions as analysed on two locations on sample 150821-II (no corresponding SEM image shown) with X-ray microanalysis are shown in Table 18. For both measurements, the Al/Ta ratio is close to 3, which corresponds to the stoichiometry of Al_3Ta. Figure 23b shows a section of a sample cross-section with the maximum observed amount of Al_3Ta impurities. Other areas of the cross-section show no or hardly any impurities, as can be seen Figure 23a. Therefore, the average phase fraction of Al_3Ta impurities for all samples could not be determined in a straightforward way.

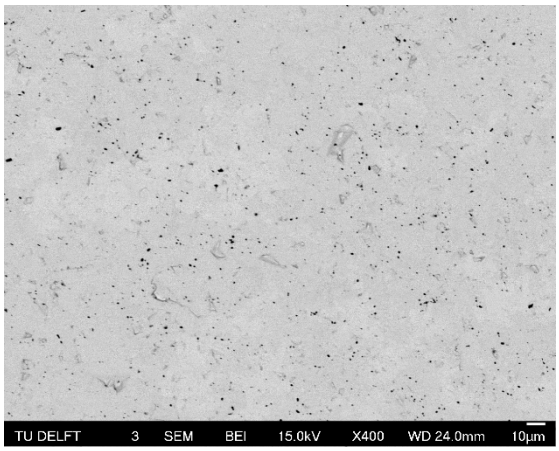

(a) surface of sample 150821-II

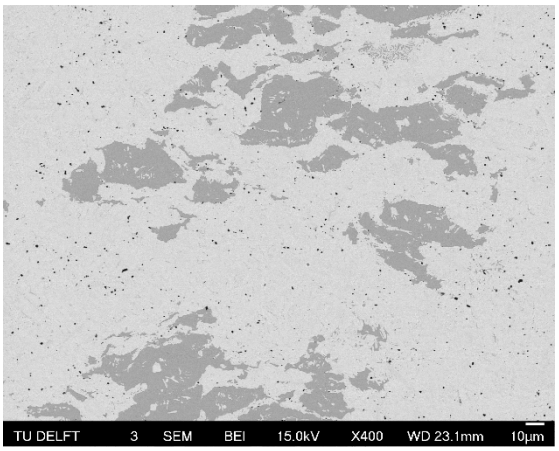

(b) cross-section of sample 150814-II

Figure 23: SEM backscatter images of microstructure of mainly single phase Ta_2AlC samples. a) microstructure of sample 150821-II in an area without Ta-Al intermetallic impurities, b) microstructure of sample 150814-II in an area with a maximum amount of Ta-Al intermetallic impurities.

Table 18: Atom percentages of Ta, Al, C, and O in Ta-Al intermetallic impurities in Ta_2AlC sample (150821-II), as measured by X-ray microanalysis with EPMA.

	Ta	**Al**	**C**	**O**	**Al/Ta ratio**
Location 1	23.9 ± 0.1	74.8 ± 0.3	1.3 ± 0.4	0.0 ± 0.0	3.13
Location 2	23.3 ± 0.2	74.6 ± 0.4	2.0 ± 0.6	0.0 ± 0.0	3.2

Typical microstructure mixed sample

Representative SEM backscatter images of the microstructure of mixed (Ta_2AlC and Ta_4AlC_3) samples is shown in Figure 24. It was found that the dark grey areas correspond to Ta_2AlC MAX phase, and the light grey areas correspond to Ta_4AlC_3 MAX phase, based on the results of X-ray microanalysis by EPMA, as shown in Figure 25. Figure 25a shows a SEM backscatter image of the sample surface of a mixed sample (sample 150604) and Figure 25a-c shows three qualitative x-ray EPMA maps of the same area for the elements aluminium, tantalum, and oxygen. On the SEM backscatter image 'light' and 'darker' grey areas are visible in the microstructure. The EPMA map of aluminium indicates that the atom percentage of aluminium is less in the lighter areas of the SEM image (these areas are dark blue on the EPMA map). The EPMA map of aluminium indicates that the atom percentage of aluminium is higher in the lighter areas of the SEM image (these areas are bright pink on the EPMA map). As XRD analysis of mixed samples only identifies the presence of Ta_2AlC and Ta_4AlC_3, it is assumed that the light grey areas correspond to Ta_4AlC_3, and the dark grey areas correspond to Ta_2AlC. This in accordance with the fact that heavy elements backscatter more and hence appear brighter on SEM backscatter images [111]. Ta_4AlC_3 consists of a higher atom percentage of the heavy element tantalum.

The black spots within the microstructure are internal oxides, formed during synthesis. This follows from comparing the locations of the black spots on the SEM image shown in Figure 25a with the locations of the white spots in Figure 25d, which correspond to a relatively very high O content. The amount of internal oxides was significantly reduced by sintering in argon atmosphere ($pO_2 \approx 1$ ppb; $pH_2O \approx 1$ ppm) instead of vacuum (≥ 0.77 mbar).

The microstructure of the mixed MAX phase samples show elongated grains with a width in the order of microns, and a length in the order of tens of microns. No visible porosity was found in the microstructure of the samples produced by SPSing from elemental powders. Lack of significant porosity is supported by measured densities close to theoretical density, as shown in section 4.2.3.

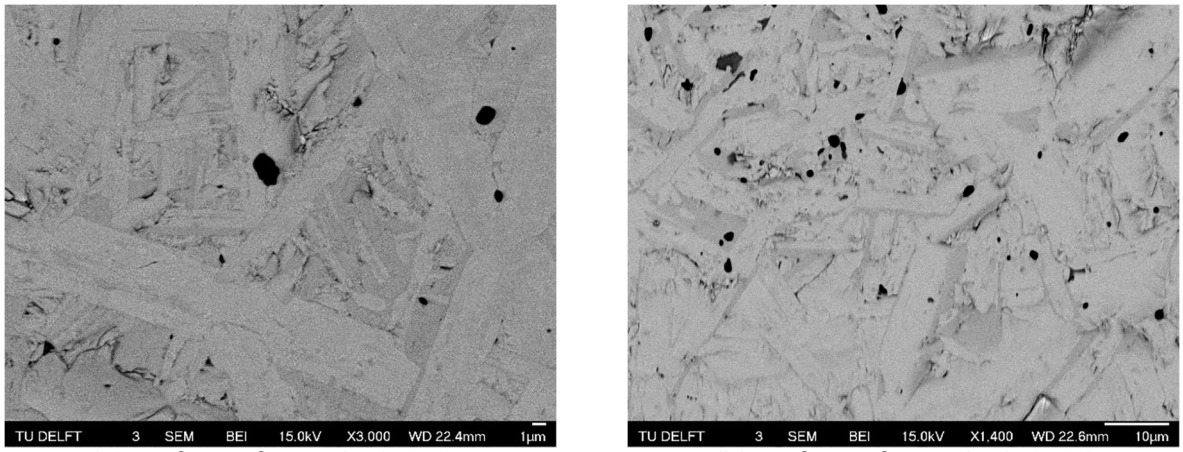

(a) surface of sample 150604 (b) surface of sample 150721

Figure 24: Representative SEM backscatter images of microstructure of mixed (Ta_2AlC & Ta_4AlC_3) MAX phase samples.

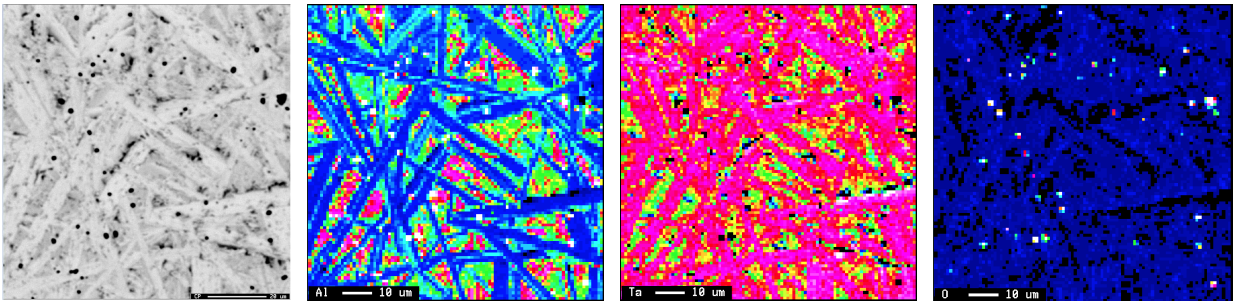

(a) SEM backscatter (b) qualitative Al mapping (c) qualitative Ta mapping (d) qualitative O mapping

Figure 25: Qualitative EPMA maps of aluminium, tantalum, and oxygen (sample 150604).

4.2.3 Hardness & density

Density and Hardness were determined by the Archimedes method and Vickers indentation, respectively. The measured density and average Vickers hardness for each sample is shown in Table 19.

The distilled water in which the samples were submerged for density measurement was 21.5 °C at the start of the measurements, and 22.0 °C after finishing. The water density corresponding to the average temperature of 21.75 °C was used for the sample density calculations, which is 0.99785 g/cm^3.

Vickers micro hardness indentation was performed on each sample, with a maximum of 5 indents per sample. From these measurements the average HV is calculated per sample, which are given in Table 19. For most samples, only a small surface area was available for indentation,

as other parts of the samples had been used for other experiments. For sample 150423 and 150821-II, respectively only 1 and 3 out of 5 indentations were successful, as a part of the indents had to be disregarded due to uneven diagonals. For sample 150814-I and 150824 all indentations had to be disregarded.

Table 19: Measured density (gr/cm^3) and Vickers hardness (HV) of dense bulk Ta-Al-C MAX phase samples.

Sample	MAX phase type	Density (g/cm^3)	Vickers hardness (HV)
150423	mixed	11.06	531
150604	mixed	11.42*	503
150721	mixed	12.34	372
150814-I	Ta_2AlC	12.37	No results
150814-II	Ta_2AlC	11.50	496
150821-I	Ta_2AlC	12.02	552
150821-II	Ta_2AlC	11.30	486
150824	mixed	11.87	No results
151109	mixed	12.72	402

*This is the average density of two measurements on different pieces from sample 160604

4.3 Microstructure and composition of oxide scale

SEM backscatter images of cross-sections of the oxide scales formed on Ta_2AlC and mixed samples after isothermal oxidation for 10 hours in artificial air at 600, 700, and 800 °C, are shown in Figure 26. Based on these images, the oxide scale thickness and microstructure is similar for Ta_2AlC and mixed MAX phase.

After isothermal oxidation of bulk Ta_2AlC and mixed samples at 600 °C a very thin (10-15 µm) darker coloured oxide enriched layer has formed on the sample surface. It is not clearly distinguishable from the underlying MAX phase matrix with SEM, see Figure 18a and d. However, a qualitative mapping of oxygen by X-ray microanalysis with EPMA clearly shows a layer of 10-15 µm thickness on the sample surface (sample 150814-II) for which the oxygen concentration is significantly increased (see Appendix 2 – Qualitative mapping of oxide scale of Ta2AlC). After isothermal oxidation at 700, and 800 °C, a white oxide scale forms on the sample surface, with a maximum observed oxide thickness of 30 and 250 µm respectively, see Figure 26b-f. The oxide scale is porous and very easily flakes off the surface while handling the sample, especially for the sample oxidized at 800 °C. Spallation cracks can be seen in Figure 26b and e. The oxide scale at 700 °C contains parts of original MAX phase composition, as highlighted with a red arrow in Figure 26b. Cracks are visible within the oxide scale, as indicated in Figure 27.

Furthermore, oxidation was found to occur in an uneven manner along the sample surface, with most oxidation along the sample edges and corners. Examples can be seen in Figure 28, showing oxidized sample edges on cross-sections of several TGA samples. Some areas of the original sample surface as can be seen in the cross-sections do not have a visible oxide scale, while some sample edges have been rounded off by relatively extensive oxidation.

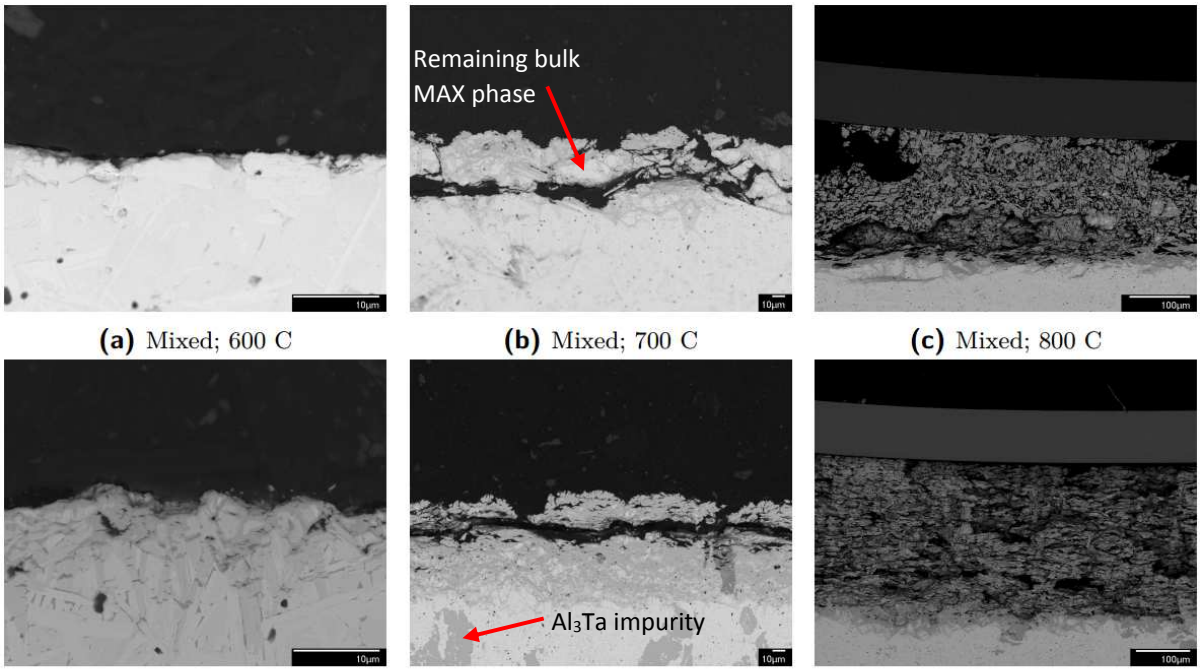

Figure 26: SEM backscatter electron images of cross-sections of oxide scales after 10 hours of isothermal oxidation of Ta_2AlC (sample 150814-II) and mixed (sample 150604) MAX phase in artificial air in the 600 – 800 °C temperature range; a & d) Ta_2AlC and mixed MAX phase oxidized at 600 °C with hardly visible oxide scale, b & e) Ta_2AlC and mixed MAX phase oxidized at 700 °C showing porous oxide scale of approximately 30 µm thickness of varying composition, where e) shows areas of Al_3Ta impurities, example indicated by red arrow, c & f) Ta_2AlC and mixed MAX phase oxidized at 800 °C showing highly porous oxide scale of maximal 250 µm thickness.

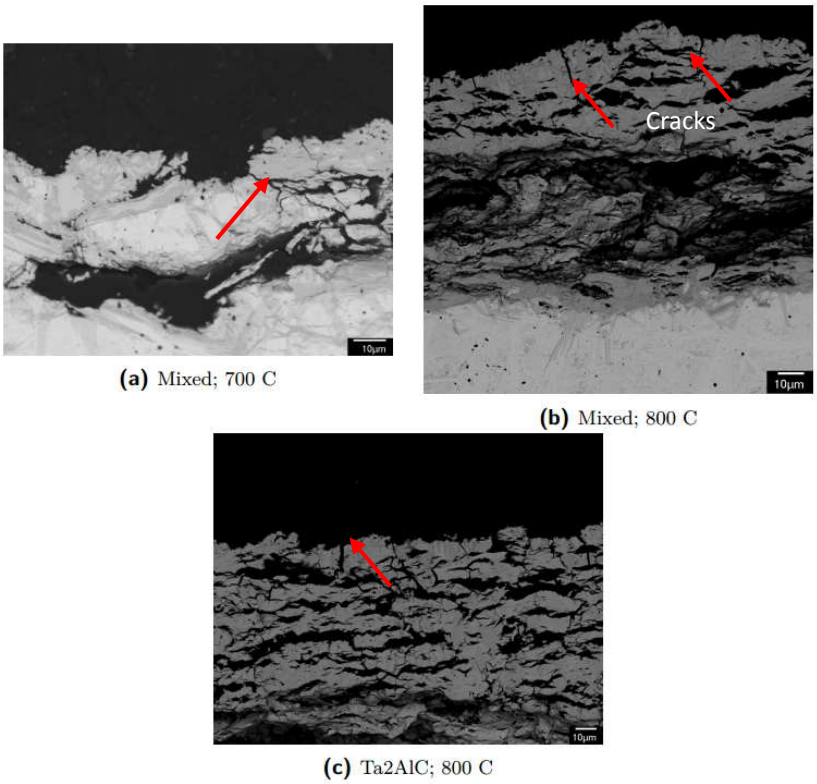

(a) Mixed; 700 C

(b) Mixed; 800 C

(c) Ta2AlC; 800 C

Figure 27: SEM backscatter electron images of the oxide scale in cross-section on Ta_2AlC (c) (sample 150814-II) and mixed (a, b) (sample 150604) MAX phase after oxidation in artificial air for 10 hours at 700 (a) and 800 °C (b, c), showing cracks within the oxide scales.

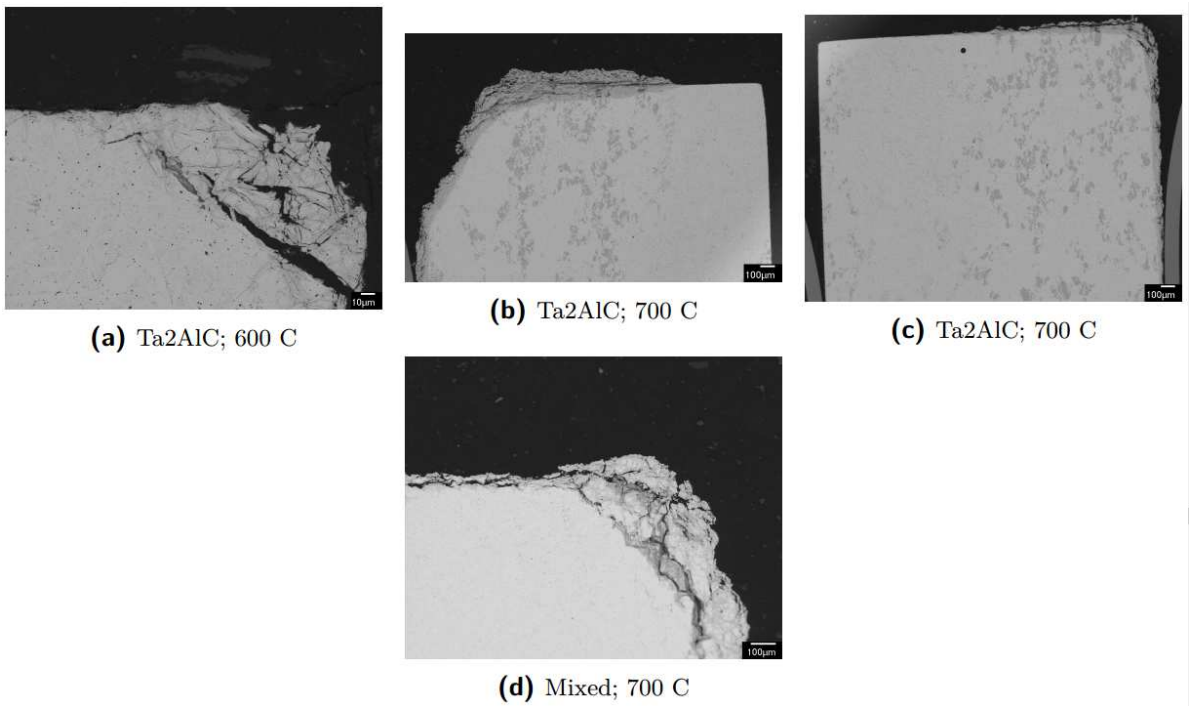

(a) Ta2AlC; 600 C

(b) Ta2AlC; 700 C

(c) Ta2AlC; 700 C

(d) Mixed; 700 C

Figure 28: SEM backscatter electron images of cross-sections of Ta_2AlC (a, b, c) (sample 150814-II) and mixed (d) (sample 150604) MAX phase, oxidized in artificial air for 10 hours, showing uneven thickness of the oxide scale along sample edges.

XRD analysis of the surface of the TGA samples oxidized at 600 °C only identifies phases corresponding to the underlying bulk MAX phase material. For the TGA samples oxidized at 700 °C, the most prominent peaks in the measured XRD pattern again correspond to the bulk MAX phase material. Smaller peaks which fit with Ta_2O_5 and $Ta_{0.87}O_{1.5}$ are also identified. For the oxide formed after 10 hours of isothermal holding at 800 °C, a part of the oxide scale could be scraped off for XRD analysis, and is analysed separately from the remaining bulk sample. The XRD pattern was found to fit best with $TaO_{1.67}$, which is alternatively called δ-Ta_2O_5, and has an orthorhombic structure [112]. Additional manual analysis of the XRD pattern also shows a good fit with TaO (see Appendix 3 – XRD pattern fits for TGA samples after oxidation).

Point analysis with energy dispersive spectroscopy (EDS) of the oxide scales on all TGA samples reveal that its overall stoichiometry does not correspond well to the commonly known Ta-, Al-, or ternary oxides, such as Ta_2O_5, TaO_2, TaO, or $TaAlO_4$. Instead, the chemical composition varies along the thickness of the layer, and the average composition is shown in Table 20.

Table 20: Averaged atom% of Ta, Al, and O in the oxide scale formed on Ta_2AlC (sample 150814-II) and mixed (sample 150604) MAX phase, as measured by EDS point analysis.

		Ta_2AlC			mixed		
		Ta	Al	O	Ta	Al	O
600 °C	**average**	**26**	**9**	**66**	**20**	**7**	**73**
	min	16	5	60	13	3	55
	max	35	18	70	33	12	81
700 °C	**average**	**26**	**7**	**67**	**38**	**8**	**54**
	min	16	6	62	28	3	43
	max	31	14	74	47	10	66
800 °C	**average**	**27**	**9**	**64**	**27**	**6**	**67**
	min	17	5	51	25	5	65
	max	37	21	71	30	8	68

XRD and EDS analysis shows similar phases and average stoichiometry of the oxide scale for the Ta_2AlC and mixed samples oxidized in the 600 to 800 °C range. Locally, areas of different composition have been identified within the oxide scale with X-ray microanalysis by EPMA, for the samples oxidized at 700 and 800 °C. Figure 29 shows a representative example of the regions of different composition within the oxide scale, and Table 21 shows the corresponding average atom percentages for each region. The composition within the oxide scales was found to fluctuate from 'light' regions, into slightly darker regions, and finally the darkest regions, with an average oxygen at.% of respectively 28.8, 37.3, and 69.5. The light regions are visible as 'spots', surrounded by the dark regions with the highest oxygen atom percentage, and the quantity of light regions becomes less when moving from the oxide/MAX phase interface to the oxide scale surface. The Ta/Al ratio (see Table 21) within all regions lies within 2.1 and 2.8, and thus does not differ much.

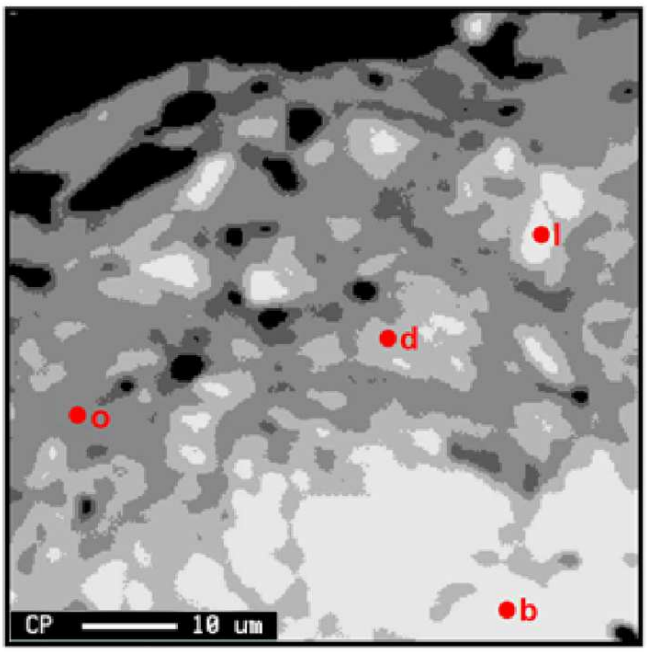

Figure 29: Representative example (sample 150814-II) of regions with different composition within oxide scales as identified on SEM backscatter images and by analysis with x-ray/EPMA, b = bulk, o = oxide, d = transition region, l = l-light area in oxide.

Table 21: Average at.% of Ta, Al, C, and O, and Ta/Al ratio within different colour regions of the oxide scale (sample 150814-II).

	Ta	Al	C	O	Ta/Al
Oxide	19.3	7.6	3.4	69.5	2.5
Transition region	33.6	12.2	17.0	37.3	2.8
Light area in oxide	36.6	17.2	18.0	28.8	2.1
Bulk	52.6	19.5	26.9	1.2	2.7

When moving from the bulk MAX phase matrix into the oxide scale, the atom percentage of oxygen was observed to increase rapidly over a short distance of approximately 2 µm on average, for all oxidized samples. This can be seen from Figure 30, which shows quantitative X-ray line scan measurements on a cross-section of Ta_2AlC (sample 150814-II) after isothermal oxidation at 600 and 800 °C. The atom percentage of Ta, Al, C, and O is measured from within the oxide scale into the underlying MAX phase material. No depletion of any of its components was observed within the MAX phase matrix directly underneath the oxide scale. It should be noted that fluctuation of the stoichiometry of the oxide scale does not follow as clearly from the line scans in Figure 30, as it does from the quantitative X-ray microanalysis and SEM image shown in Figure 29. Two possible reasons are the location of the line scans (accidentally little variation in composition) and the resolution (spacing of 1 µm between measurements along the line).

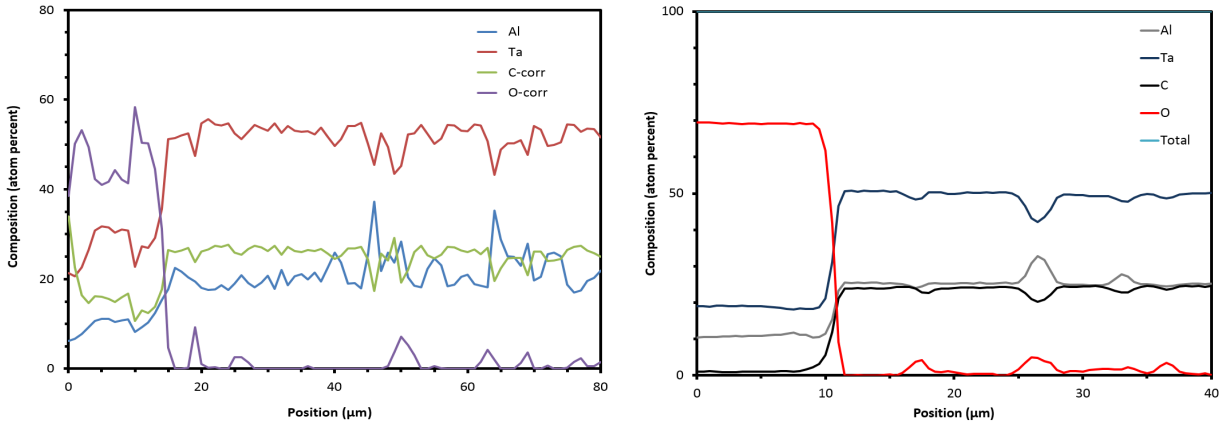

(a) (b)

Figure 30: Quantitative X-ray line scans of Al, Ta, C and O atom percentage measured on cross-sections of isothermally oxidized Ta_2AlC (sample 150814-II) when moving from oxide scale into underlying MAX phase; a) Ta_2AlC oxidized at 600 °C, line scan starting from oxide surface into MAX phase bulk, with total line scan length of 80 µm b) Ta_2AlC oxidized at 800 °C, line scan starting from within oxide scale at approximately 10 µm above unreacted sample surface until 30 µm into MAX phase bulk.

X-ray photoelectron spectroscopy (XPS) of the binding energy of tantalum and aluminium in the oxidized surfaces of the bulk samples oxidized at 600, 700 and 800 °C show that the binding energies of both elements increase when the isothermal oxidation temperature becomes higher. For tantalum, a chemical shift is observed for the core electrons of the Ta4f and Ta4d subshells, as shown in Figure 31. Both Ta4f and Ta4d subshells show splitting, which arises from spin-orbit coupling effects in the final state after an electron is removed by the energy of the impinging X-ray. Due to this effect, a double peak can be seen in the spectral lines. For Ta4f these are the Ta4f5/2 and Ta4f7/2 peak. For Ta4d these are the Ta4d3/2 and Ta4d5/2 peak. For aluminium, the binding energy of the Al2p subshell was measured to shift to a higher energy for a higher oxidation temperature, as shown in Figure 32. No subshell splitting was observed for the Ta2p state. The full measured XPS spectrum for the Ta_2AlC dense bulk samples oxidized at 600, 700 and 800 °C respectively, are shown in Appendix 4 – Measured XPS spectra for oxidized dense bulk Ta2AlC.

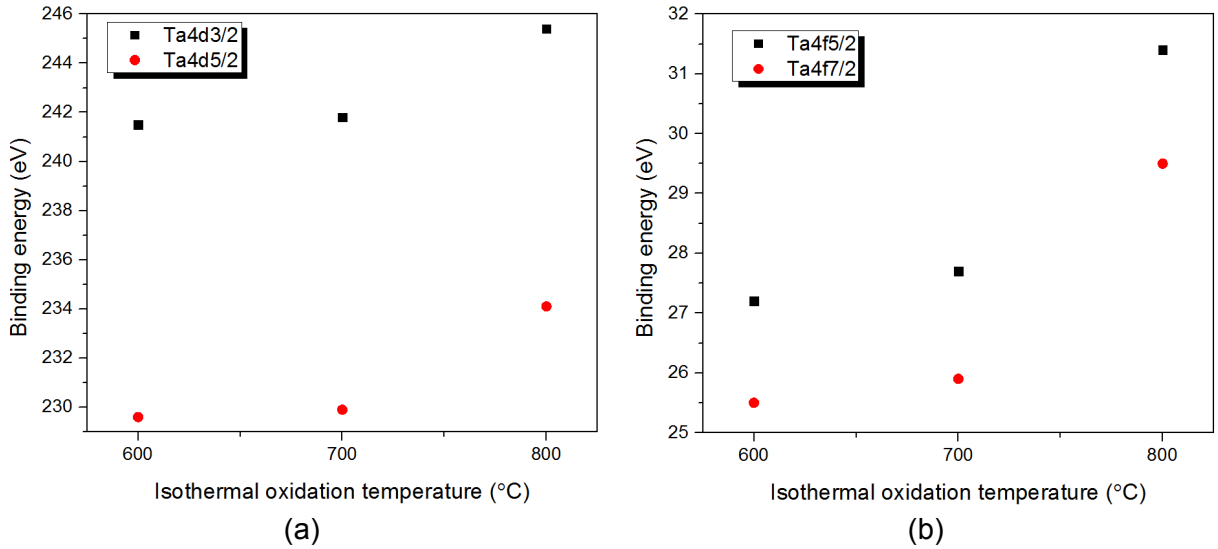

Figure 31: Binding energy against isothermal oxidation temperature for the TGA samples oxidized at 600, 700, and 800 °C as measured by XPS analysis for a) the Ta4d3/2 and Ta4d5/2 peak, and b) Ta4f5/2 and Ta4f7/2.

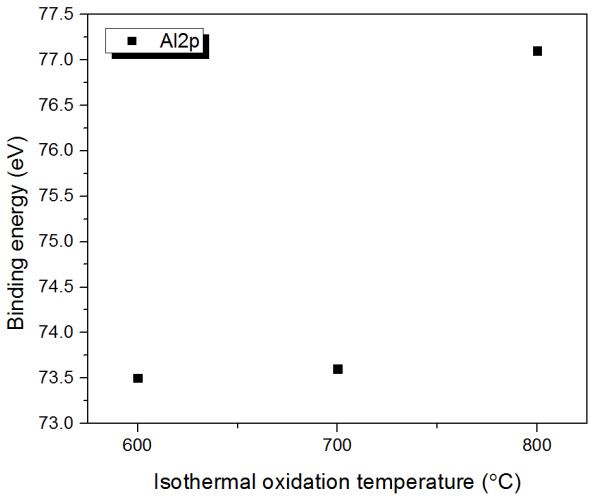

Figure 32: Binding energy against isothermal oxidation temperature for the TGA samples oxidized at 600, 700, and 800 °C as measured by XPS analysis for Al2p.

4.4 Oxidation reactions and activation energies

When heating Ta_2AlC and mixed MAX phase powder from room temperature until 1200 °C, two distinct exothermic reactions have been observed by performing Differential Thermal Analysis (DTA). The heat flow and weight gain versus sample temperature for 30 mg Ta_2AlC (sample 150821-II) heated with a heating rate of 5 °C/min is shown in Figure 33. Two peaks in the heat flow curve are observed at approximately 760 °C and 865 °C, which correspond to exothermic reactions taking place during oxidation.

The near linear increase of weight gain from room temperature to approximately 500 °C is ascribed to buoyancy of the alumina DTA crucible with MAX phase powder. At approximately 500

°C the slope of the TG curve starts to increase and a weight gain of 6.85 mg from approximately 500 to 900 °C is ascribed to uptake of oxygen during oxidation. At 865 °C the second heat flow peak takes place, and the TG curve shows a small dip at the same temperature.

The CO_2 signal within the DTA furnace during heating has been measured with a mass spectrometer and shown in Figure 33. A peak occurs at approximately 865 °C as the second heat flow peak takes place. The measured CO_2 signal increases from approximately $4.3 \cdot 10^{-11}$ A to a maximum of $1.92 \cdot 10^{-9}$ A. This indicates that carbon in the MAX phase material reacts with oxygen to form CO_2 during the second oxidation reaction.

It was found that Ta_2AlC and mixed MAX phase powder generate similar DTA results, as shown in Appendix 5 – DTA curves of Ta2AlC and mixed MAX phase powder. Therefore, further DTA experiments have only been performed on Ta_2AlC MAX phase powder.

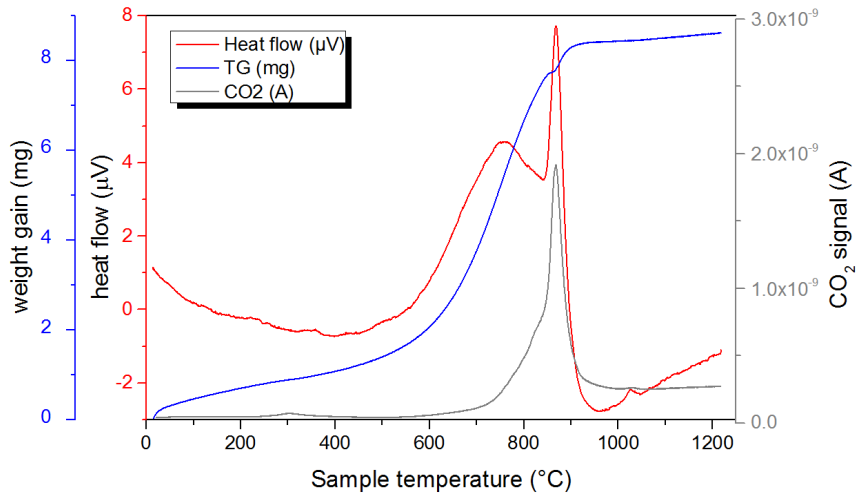

Figure 33: Heat flow and mass gain (TG) of 30 mg Ta_2AlC powder (sample 150821-II) heated from room temperature until 1200 °C with 5 °C/min, combined with CO_2 signal (obtained with mass spectrometer). Varying powder size with 2 to 30 µm diameter, as observed with SEM.

XRD analysis of Ta_2AlC and mixed MAX phase powders after the second reaction reveal the reaction products Ta_2O_5 and $TaAlO_4$. Chemical analysis of the powders when heated until 800 °C, when only the first reaction (at T = 760 °C) has taken place, shows fractions of the original un-oxidized MAX phase, alumina, tantalum-oxide ($TaO_{1.1}$), tantalum-carbide (Ta_4C_3), and ternary-oxide ($Ta_{1.86}Al_{0.14}O_{4.86}$).

The activation energies of both observed oxidation reactions have been approximated from the DTA data by the method as described in section 3.4. This has been done in two ways: 1) from data on the heat flow peak temperature, and 2) from data on the dTG/dt peak temperature. To obtain the necessary data, five DTA experiments were conducted on Ta_2AlC powder (sample 150821-II), with a heating rates of 1, 2, 5, 10, and 15 °C/min. Using a different heating rate results in a shift of the heat flow-, and dTG/dt peak temperature. It was found that the activation energy of the second oxidation reaction cannot be determined by this method. For the second oxidation reaction, the shift of the heat flow-, and dTG/dt peak temperature for different heating rates is very minor, which causes the calculated value of the activation energy based on the slope of the fit through the Kissinger points to be unreasonably high (>1400 kJ/mol). The calculated activation

energy of the first oxidation reaction in Ta_2AlC is -146 ±10 kJ/mol and 217 ±16 kJ/mol for the peak temperature from heat flow and dTG/dt, respectively. They have been determined from the slope of the linear fit through the Kissinger points shown in Figure 34.

Table 22: Activation energies as calculated from analysis of DTA data of Ta_2AlC powder (sample 150821-II) and the 95% confidence interval.

	E_a reaction 1 (kJ/mol)	95% confidence interval (kJ/mol)
Heat flow peak temperature	-146	± 10
dTG/dt peak temperature	-217	± 16

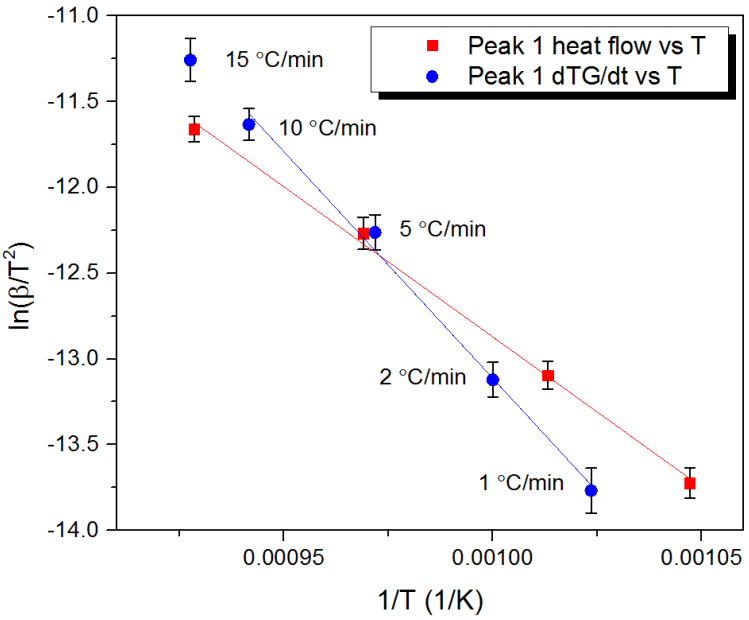

Figure 34: Kissinger points and linear fit of 1st reaction from DTA data on Ta_2AlC powder (sample 150821-II) for the heating rates 1, 2, 5, 10, and 15 °C/min, calculated based on the temperature during heating at which the peak in heat flow and dTG/dt takes place (T_p).

The activation energy of the first reaction has also been estimated from the weight gain data from TGA analysis of bulk Ta_2AlC and mixed samples, as TGA was conducted in the same temperature range as the first reaction discovered by DTA analysis (600 to 800 °C). The calculated activation energies based on TGA data is shown in Table 23. For each isothermal holding temperature of 600, 700, and 800 °C respectively, ln(k) is plotted against ($1/T_{isotherm}$), where 'k' is the slope of the linear part of the weight gain curves during isothermal holding, see Figure 35. The activation energy was determined from the slope of the linear fit through these points. The 95 % confidence interval for the activation energies calculated from TGA data is relatively large.

Table 23: Activation energies for oxidation in the temperature range of 600 to 800 °C, as calculated from analysis of TGA data on bulk Ta_2AlC (sample 150821-II) and mixed (sample 150604) TGA samples.

	E_a reaction 1 (kJ/mol)	95 % confidence interval (kJ/mol)
Ta_2AlC	-129,3	± 35.9
Mixed	-158,2	± 65.0

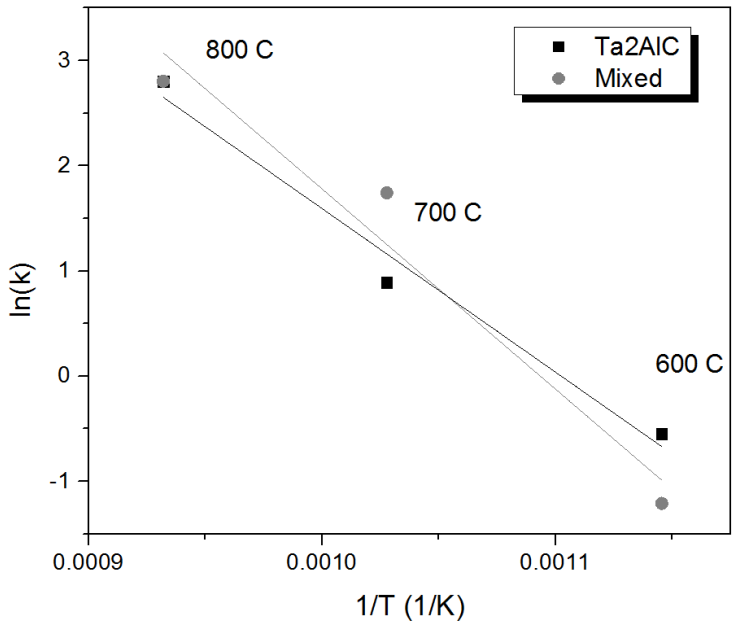

Figure 35: Kissinger points and linear from TGA data on bulk Ta_2AlC (sample 150814-II) and mixed (sample 150604) samples isothermally oxidized at 600, 700, and 800 °C for 10 hours in artificial air.

Oxidation reactions and activation energies of pure Ta and TaC powder

For comparison, the oxidation reactions in pure Ta and TaC powder have been investigated in the same manner as was done for Ta_2AlC powder. The average grain size is approximately 40 µm and 2 µm for Ta and TaC powder, respectively. Figure 36 shows the grain size distribution for both powders as measured by laser sizer. The difference in grain size is assumed not to be a factor of large influence for comparison of oxidation behaviour of both powders, as for both powders oxidation was found to take place sufficiently rapidly to fully oxidize all powder for all tested heating rates when heating to 1200 °C.

Pure Ta and TaC powder was heated from room temperature to 1200 °C with a heating rate of 1, 2, 5, and 10 °C/min respectively. Figure 37 shows the heat flow and weight gain curves versus sample temperature for 30 mg of pure Ta and TaC respectively, heated with a heating rate of 5 °C/min. Both Ta and TaC powder show one heat flow peak upon oxidation to 1200 °C. For heating with 5 °C/min, the heat flow peak for Ta takes place at approximately 578 °C, and for TaC at approximately 690 °C. A single heat flow peak was also observed for Ta and TaC for all other heating rates tested in this work whereas Ta_2AlC showed two separate heat flow peaks (see Figure 33), at 760 °C and 865 °C for a heating rate of 5 °C/min.

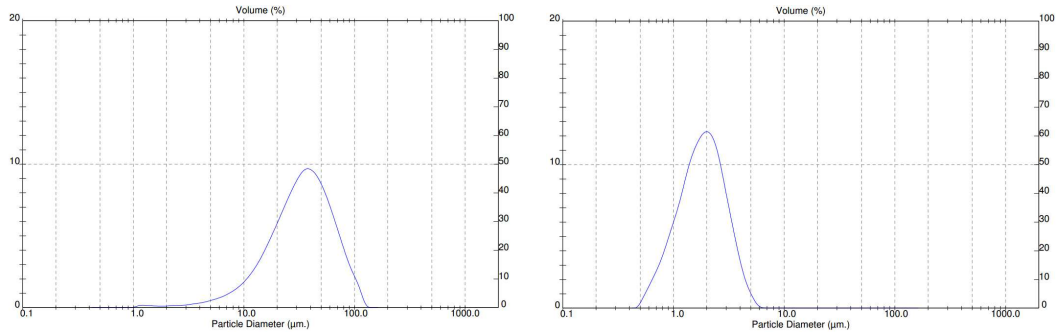

(a) Ta (b) TaC

Figure 36: Grain size distribution of a) Ta, and b) TaC powder used for DTA, as measured with laser sizer.

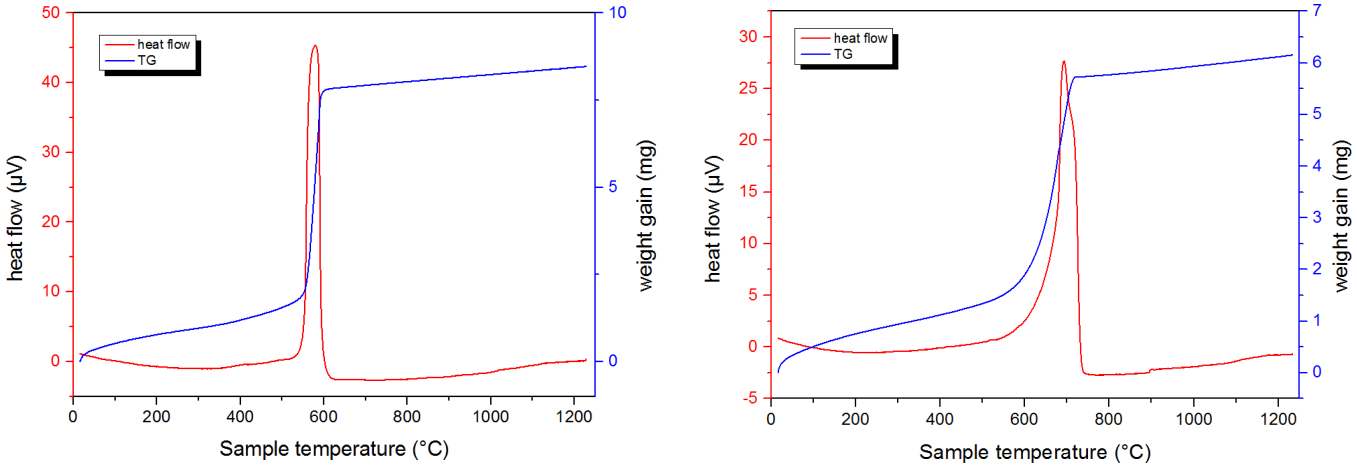

(a) Ta (b) TaC

Figure 37: Heat flow and mass gain (TG) curves of 30 mg pure Ta and TaC powder heated from T_{room} until 1200 °C with 5 °C/min, a) pure Ta powder, b) pure TaC powder.

The CO_2 signal was measured for Ta and TaC with a mass spectrometer, for the DTA experiments with a heating rate of 1, 2, 5 and 10 °C/min. During oxidation of Ta, no increase of the CO_2 signal takes place. During oxidation of TaC, the CO_2 signal increases notably at the same temperature as the heat flow peak occurs, for all tested heating rates (see Appendix 6 – DTA curves of Ta and TAC powder incl. CO2 signal for the DTA plots with heating rate 2 °C/min). This indicates that the reaction of carbon in TaC with oxygen to form CO_2 happens at the same time as oxidation of Ta takes place, as only one heat flow peak is observed.

XRD analysis of Ta and TaC after heating to 1200 °C shows that full oxidation has taken place, as only Ta_2O_5 is identified for both powder types and for all heating rates tested.

The calculated activation energies for the oxidation reaction of Ta and TaC powder and their 95 % confidence interval is given in Table 24, as calculated from the DTA data for different heating rates. The 95 % confidence intervals of the calculated activation energies for Ta and TaC are very large, as the linear fit through the Kissinger points is poor. Figure 38 shows the corresponding plot with Kissinger points and linear fit line, based on the DTA data for Ta and TaC powder. Based on the poor linear fit for TaC, the calculated E_a for TaC with this method will be disregarded. Excluding the Kissinger point corresponding to a heating rate of 1 °C/min in Figure 38b in the

calculation of the activation energy does not result in a reasonable value for E_a, or a smaller 95 % confidence interval either (see Appendix 7 – Kissinger analysis for non-isothermal TaC oxidation, excluding the heating rate of 1 °C/min)

Table 24: Activation energies as calculated from analysis of DTA data of Ta and TaC powder, and the 95 % confidence interval.

	E_a reaction 1 (kJ/mol)	95 % confidence interval (kJ/mol)
Ta - heat flow peak temperature	-305.3	± 88.2
Ta - dTG/dt peak temperature	-286.6	± 98.0
TaC - heat flow peak temperature	-207.4	± 162.0
TaC - dTG/dt peak temperature	-268.5	± 176.8

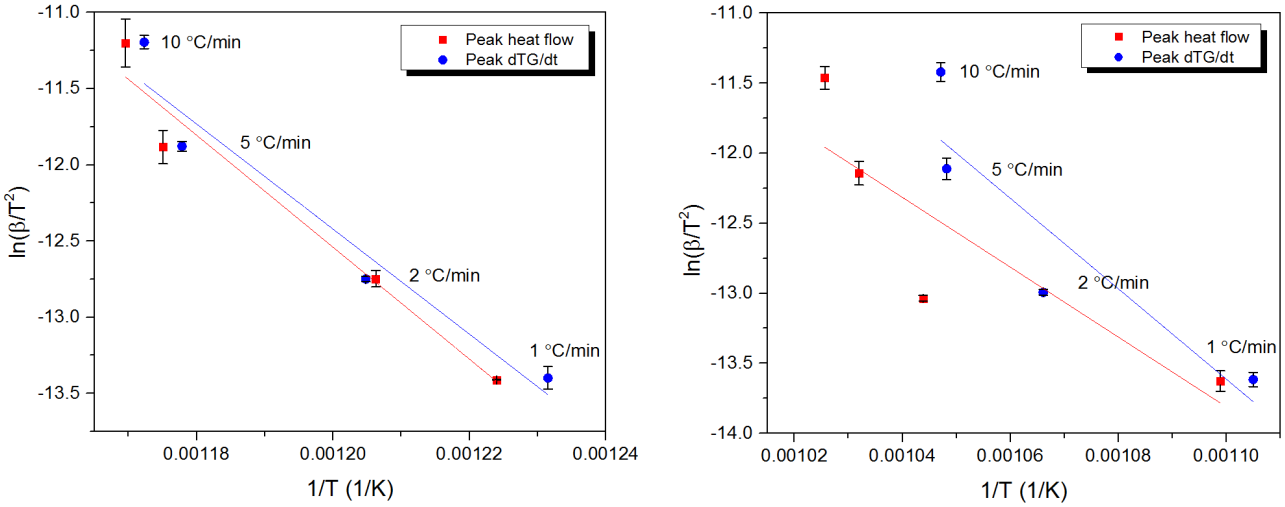

Figure 38: Kissinger points and linear fit from DTA data of Ta and TaC powder for the heating rates 1, 2, 5, and 10 °C/min, a) pure Ta powder, b) pure TaC powder, calculated based on the temperature during heating at which the peak in heat flow and dTG/dt takes place (T_p).

4.5 Oxidation kinetics

The oxidation kinetics are analysed based on the weight gain curves for isothermal holding of dense bulk Ta_2AlC (sample 150814-II) and mixed (sample 150604) samples, for 10 hours at 600, 700, and 800 °C. All samples show approximately linear weight gain after the initial start of oxidation (approximately 30 minutes at 600 °C, shorter times at 700 and 800 °C). The total mass gain for 10 hours isothermal holding increases approximately with an order of magnitude from 600 to 700 °C, and from 700 to 800 °C. The mass gain for Ta_2AlC and mixed material lies in the same order of magnitude for each holding temperature. Figure 39 shows the weight gain curves versus time as measured with thermogravimetric analysis (TGA), separately for all three temperatures.

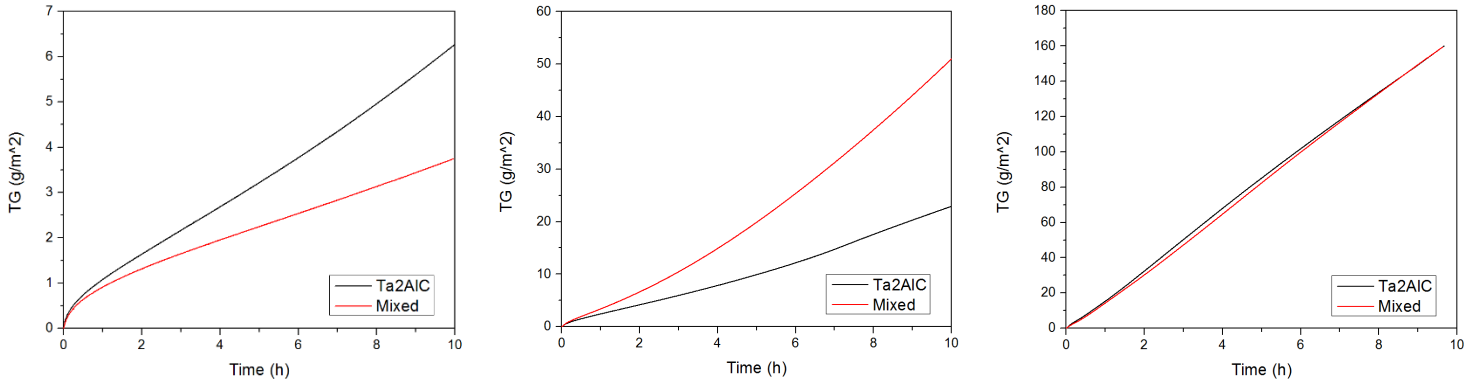

(a) Oxidation at 600 °C (b) Oxidation at 700 °C (c) Oxidation at 800 °C

Figure 39: Mass gain vs. time for isothermal oxidation of dense bulk Ta_2AlC (sample 150814-II) and mixed (sample 150604) MAX phase for 10 hours in artificial air, a) oxidation temperature of 600 °C, b) oxidation temperature of 700 °C, c) oxidation temperature of 800 °C.

The measured mass gain data during isothermal holding at 600, 700, and 800 °C have been used to calculate corresponding oxide scale thickness for pure dense $TaAlO_4$, Ta_2O_5, TaO_2, and TaO respectively, over time (for 10 hours holding). The plots of oxide scale thickness versus time for each holding temperature are shown in Figure 40. When comparing the calculated scale thickness with the observed oxide scale thickness on cross-sections of the TGA samples, as shown in Figure 26, the calculated oxide thicknesses are roughly an order of a magnitude lower than the observed oxide scale thickness on the TGA samples. The curves shown in Figure 40 have been calculated by dividing the mass gain per m^2 by the theoretical density of the oxide (in g/cm^3).

Figure 40: Oxide scale thickness vs. time for isothermal oxidation of dense bulk Ta_2AlC (sample 150814-II) and mixed (sample 150604) MAX phase for 10 hours in artificial air, a) oxidation temperature of 600 °C, b) oxidation temperature of 700 °C, c) oxidation temperature of 800 °C.

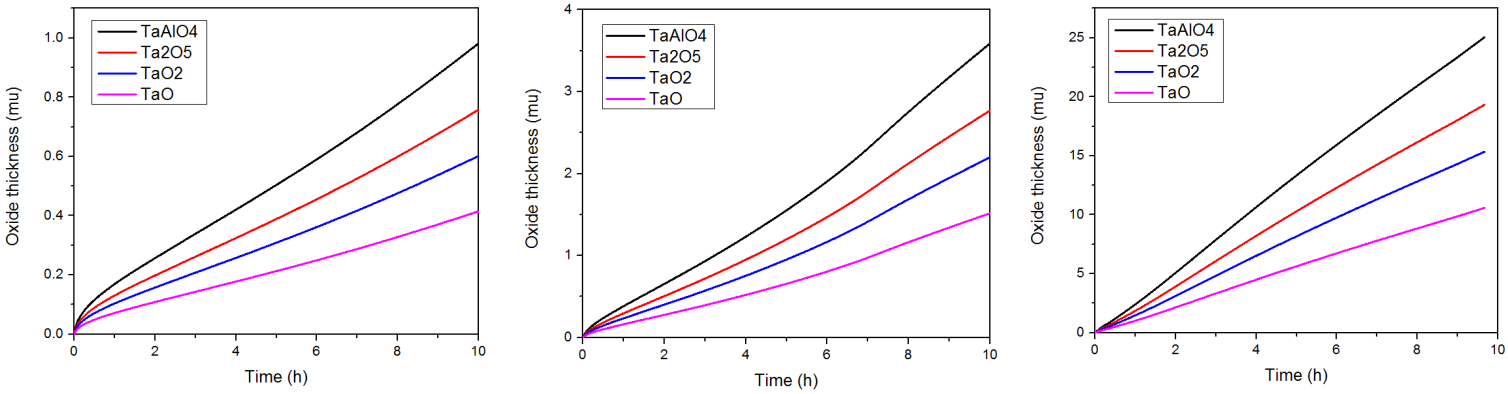

(a) Oxidation at 600 °C (b) Oxidation at 700 °C (c) Oxidation at 800 °C

4.6 Analysis of self-healing potential of Ta-Al-C MAX phases

The self-healing potential of Ta-Al-C MAX phase was tested by cracking and reopening a newly designed specimen by wedge loading using an electro-mechanical load frame (Instron, type 5500R). The method is described in section 3.5.

A microcrack of 8.3 mm length and with a minimum and maximum width of respectively 1 and 8 μm in a dense bulk sample of mixed MAX phase (sample 151109) was observed to be mostly *not* filled with oxide after isothermal oxidation at 600 °C in air for 16 hours.

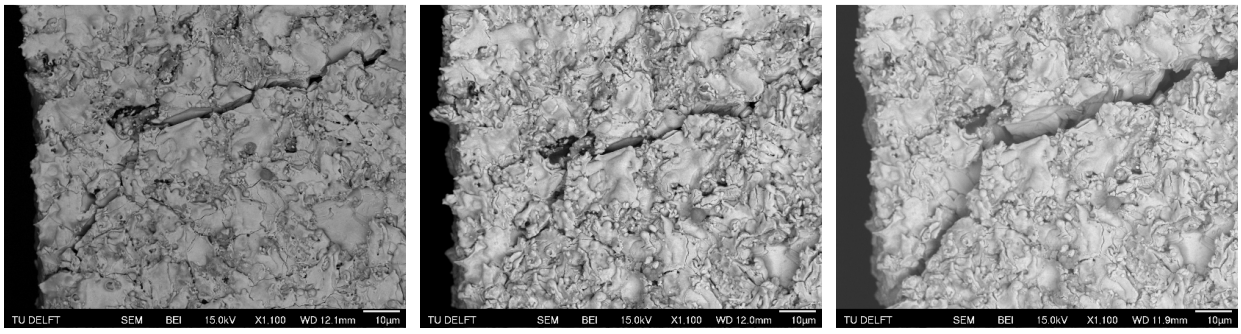

(a) virgin crack (b) oxidized crack (c) re-opened crack

Figure 41: SEM backscatter images of the start of a crack on mixed wedge sample surface (sample 151109); a) before oxidation (virgin), b) after isothermal oxidation at 600 °C for 16 hours in air, c) after re-opening of the crack after oxidation.

Secondary SEM images of the start of the crack before and after oxidation, and after 're-opening' of the crack, viewed on the sample surface are shown in Figure 41. The observed crack width is approximately the same in the virgin material as it is after oxidation. After re-opening the crack has widened notably.

Figure 42 shows SEM backscatter and secondary images of the cross-section of an oxidized crack in dense bulk Ta_2AlC MAX phase (sample 150824). The backscatter images show good visible contrast between the dark grey oxide scale and the underlying bulk MAX phase material. The oxide after isothermal oxidation at 600 °C for 16 hours in air is noticeably thicker (between 30 and 50 μm) and more visible than the oxide scale observed after 10 hours of isothermal oxidation (see Figure 26). Another notable difference with the oxide scale observed after 10 hours oxidation, is the presence of pores in the oxide scale after 16 hours of oxidation at 600 °C. The crack width is not filled by the oxide, and the open crack is clearly visible. This can be verified by the SEM secondary images in Figure 42, which show the topology of the cross-section.

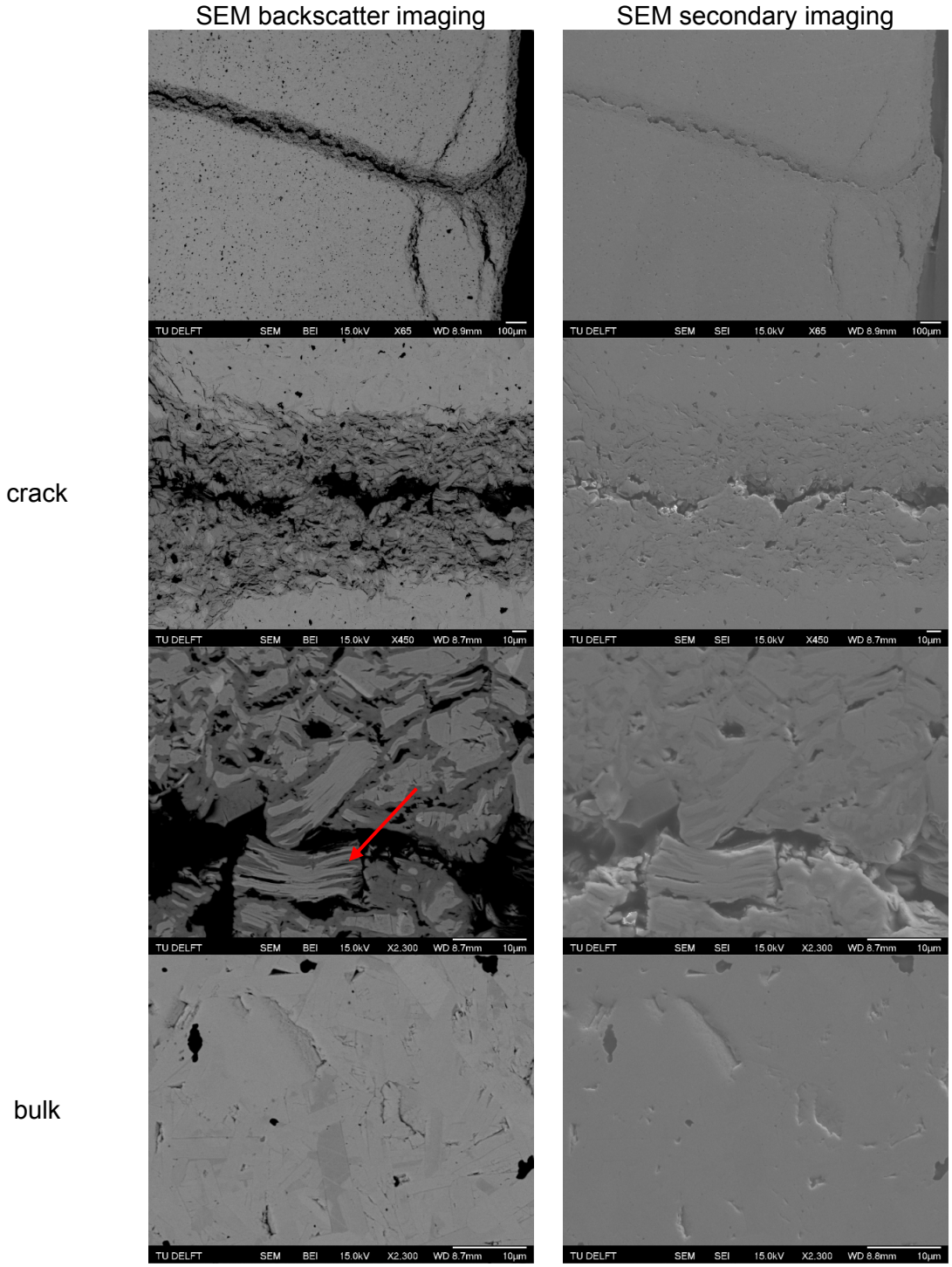

Figure 42: SEM backscatter and secondary images of an oxidized crack on Ta_2AlC wedge sample cross-section (sample 150824) after isothermal oxidation at 600 °C for 16 hours in air.

Furthermore, the layered microstructure of the MAX phase is clearly visible within the oxide scale. An example is indicated in Figure 42 with a red arrow. The formation of pores can be seen within the oxide scale.

Oxidation is observed to take place irregularly; on some locations a big change from the virgin material was observed after oxidation, while other locations were barely oxidized. Irregular oxidation of the microcrack in sample 150824 is shown in Figure 43. A red arrow points out a heavily oxidized region.

Figure 43: Optical microscopy image (Keyence) of the microcrack in Ta_2AlC wedge sample after isothermal oxidation at 600 °C for 16 hours in air, as seen from the surface (sample 150824), showing irregular oxidation.

An indication of the mechanical strength of a mixed MAX phase wedge sample during cracking and crack re-opening after oxidation is obtained from the load displacement curves shown in Figure 44. The blue curve corresponds to the crack initiation and formation in the virgin sample. The red curve corresponds to crack re-opening and further crack formation after isothermal oxidation. At the start of the test the wedge is placed in contact with the wedge sample and preloaded. This determines the origin in Figure 44. The virgin wedge sample before fabrication of the microcrack could bare a maximum load of 225 N. Further wedge displacement initiates the formation of the microcrack. During cracking, multiple near vertical load drops took place. When formation of the microcrack was stopped, the remaining loadbearing capacity of the wedge sample was 155 N. The final crack length is approximately 8.3 mm. After isothermal oxidation, the sample was loaded again. The maximum load is reached at approximately 142 N, after which it drops to 140 N in about 7 seconds, followed by a near vertical load drop. After re-cracking, the crack length is approximately 11.9 mm. After oxidation, the loadbearing capability of the wedge sample was not increased.

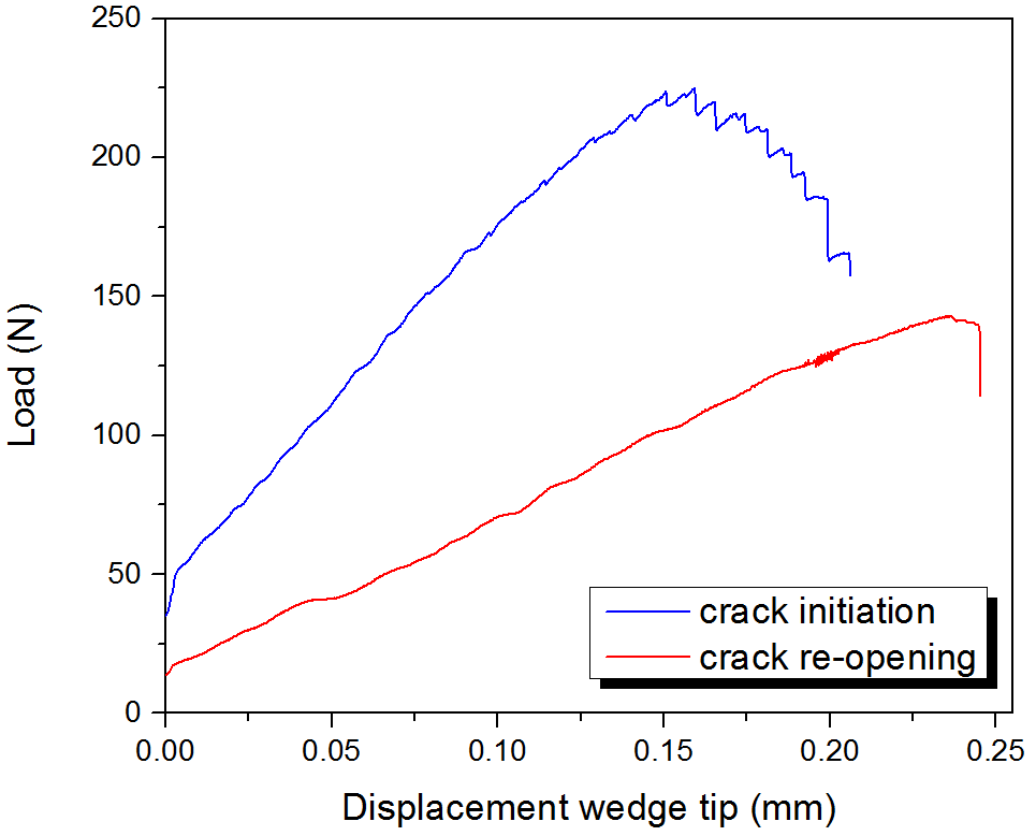

Figure 44: Load versus displacement curves for crack initiation and crack re-opening in a mixed wedge sample (sample 151109) after isothermal oxidation at 600 °C for 16 hours in air.

5. Discussion

5.1 Synthesis and characterization of dense bulk Ta-Al-C MAX phase

For the three pressure-less sintering experiments performed on elemental powder mixes, it was found that increasing the temperature from 1200 to 1500 °C resulted in the formation of a significant fraction Ta_2AlC MAX phase (third PLS sample). All pressure-less sintered samples also contained significant fractions of impurities: Ta-Al intermetallics and carbides, and $Ta_{0.97}O$ for the sample sintered at 1200 °C. The formation of the oxide phase is assumed to be due to a small amount of oxygen or water vapour in the powders used for the elemental powder mix, due to initial handling of powders outside argon atmosphere. After this, all powder handling was performed in argon atmosphere.

The powder composition was only changed for the third attempt of pressure-less sintering, but the sinter temperature was also changed. The effect of the change of powder composition can therefore not be determined separately based on the results as shown in Table 15.

Pressure-less sintering resulted in the formation of porous material with low mechanical strength in all cases, as was observed during grinding of the sample surfaces for XRD analysis; a large amount of material was very easily grinded off.

Further sintering of the pulverized third PLS sample with SPS at 1500 °C resulted in dense bulk material without any MAX phase. Therefore it seems that the fractions of Ta_2AlC and Ta_4AlC_3 that were present in the PLS sample have decomposed during further sintering under pressure at 1500 °C. Decomposition of MAX phases during sintering in vacuum has been reported in literature, where it is stated that 'purity of powders and sintered materials, temperature, vapour pressure, atmosphere, and type of heating elements used' seem to be important factors determining the susceptibility to thermal decomposition [113]. Surface decomposition due to the release of gaseous Al is reported, because the vapour pressure of Al exceeds the pressure in the furnace. Use of a graphite heater was reported to promote dissociation of Ti_3SiC_2 into TiC_x [113]. In this work the powdered PLS sample was heated by SPS in vacuum in a graphite die and punches. This route toward synthesis of dense bulk Ta-Al-C MAX phase was not pursued further. PLS of porous MAX phase followed by densification by SPS is a two-step synthesis route, and it would be more desirable to design a direct 'one-step' route in which the reaction to form MAX phase and densification take place simultaneously.

Direct SPSing of dense bulk Ta-Al-C MAX phase from a mixture of Ta, Al_4C_3, and C (ratio 2 : 0.25 : 0.25) was tried because Al_4C_3 has lower sensitivity to high temperatures than elemental Al. Aluminium melts at 660 °C, and problems with leakage of molten aluminium were expected when using elemental powders, based on the experience of direct synthesis of Ti_2AlC and Cr_2AlC MAX phase from elemental powders [108, 109]. As no MAX phase was identified by XRD with the use of carbide powder, further attempts were made using powder mixes of elemental powders.

The following factors were found to influence the result of direct SPSing of elemental powder mixes: lowering of the sintering temperature from 1500 to 1400 °C (leaving all other parameters unchanged) results in the formation of mainly Ta_2AlC, instead of a mixture of Ta_4AlC_3 and Ta_2AlC (as identified by XRD on the sample surface after grinding and polishing). As Ta_4AlC_3 has a lower

atom percentage of Al than Ta_2AlC, it is assumed that for sintering at 1500 °C, a bigger fraction of the elemental unreacted Al is pressed out or evaporated from the die and punches than for sintering at 1400 °C. It is not understood at what stage of the heating program the Al is pressed out of the graphite sample holder. As explained in section 4.1, an intermediate holding step at was added (with T_{hold} = 750 or 700 °C) before sintering, to allow molten Al to react with Ta to form a solid intermetallic and avoid loss of liquid Al. During intermediate holding, the pressure on the green body is kept at a minimum of 16 MPa. The hypothesis that a reaction between Ta and Al takes place during intermediate holding is supported by the observed piston travel of 0.3 mm which indicates densification, even though a minimal pressure is applied to the sample.

The compositional difference between samples sintered at 1400 °C and 1500 °C hints towards the loss of Al also during sintering, which suggests that not all liquid Al has reacted during intermediate holding, and more Al is lost for the higher sintering temperature. Nevertheless, the addition of the intermediate holding step noticeably reduced the amount of liquid material being squeezed out of the sample holder, as this could be observed when taking the sample and holder out of the SPS after synthesis. Decreasing the intermediate holding temperature from 750 to 700 °C and increasing the holding time from 5 to 15 minutes further decreased the amount of Al leakage during synthesis.

It was found that sintering in vacuum consistently lead to the formation of a small but significant fraction of internal oxides (TaO, $TaAlO_4$, as identified by XRD). Sintering in argon avoids the formation of oxide impurities. The formation of oxides is therefore attributed to the vacuum not being high enough (≥ 0.77 mbar) to avoid the presence of oxygen (as O_2 or in H_2O) in the SPS vessel to form internal oxides.

Furthermore it should be noted that changing the sample diameter from 20 to 40 mm in diameter caused the formation of mixed material (Ta_2AlC + Ta_4AlC_3) when using the program that results in Ta_2AlC for samples with a diameter of 20 mm. Hence it seems that higher temperatures than the set sintering temperature are reached during sintering of bigger samples. Possibly, this effect is caused by local inhomogeneous heating of the larger powder compact.

Analysis of the microstructure of Ta_2AlC has shown the presence of a significant fraction of Al_3Ta impurity on some areas of sample cross-sections. It was shown by Okamoto [114] that Al_3Ta forms below 1098 °C at atmospheric pressure. Hossein et. al has shown that Al_3Ta is the first phase that forms when sintering Ta-Al powder mixtures, regardless of the initial composition [115]. Hence it can be assumed that the Al_3Ta impurities have formed before the sintering temperature was reached, and before the pressure reaches 50 MPa. This means that the intermetallic phase of Al_3Ta starts to nucleate and grow before Ta_2AlC MAX phase forms when higher temperature and pressure is reached. It is not known whether part of the Al_3Ta transforms into Ta_2AlC at T_{sinter} and P_{sinter}. Possibly, the excess Al in the elemental powder mixture (composition Ta : Al : C = 2 : 1.2 : 1) remains in the Al_3Ta impurities.

The microstructure of both Ta_2AlC and mixed samples show the characteristic features of the MAX phase microstructure when observed with SEM: elongated grains, layered microstructure visible at high magnification.

The microstructure of the mixed MAX phase sample show alternating grains of Ta_2AlC and Ta_4AlC on a micrometre length scale. Lin *et al.* [80] has observed examples of polymorph Ta-Al-C MAX phases with – amongst others – alternating atomic layers of Ta_2AlC and Ta_4AlC_3. Possibly, the formation of alternating grains of Ta_2AlC and Ta_4AlC has started from a similar polymorph microstructure.

The measured densities of the Ta_2AlC and mixed samples as shown in section 4.2.3 are in reasonably good agreement with theoretical density as stated in literature; 11.52 g · cm^{-3} for Ta_2AlC [26], and 12.919 g · cm^{-3} for Ta_4AlC_3 [81]. Hence it can be concluded that dense bulk MAX phase was successfully synthesized. However, the measured density of Ta_2AlC samples varies from min. 11.30 to max. 12.37 g · cm^{-3}, and for mixed samples from min. 11.06 to max. 12.72 g · cm^{-3}. The measured results do not show a higher density for the mixed samples compared to Ta_2AlC samples as was expected based on the values for theoretical density. Possible reasons are measurement error, and the fact that the mixed samples also consist of Ta_4AlC_3, which makes the difference in density smaller than the theoretical densities of the pure MAX phases.

The most probable reasons for scatter of the measured densities are the presence of air bubbles on the sample and holder (causing lower measured density), and the size difference of the sample pieces that were measured. For some samples relatively small pieces had to be used, with surface area below 12 mm^2 and a thickness of max. 4 mm. The presence of air bubbles on the older, will have a relatively larger effect on the calculated density for samples with a smaller volume. It stands out that some of the Ta_2AlC samples have a density higher than the reported theoretical density of 11.52 g · cm^{-3} [26], which cannot be explained by the presence of air bubbles. The presence of a varying amount of Al_3Ta impurity cannot explain the high measured density either, as the density of Al_3Ta is reported to be 6.89 g/cm^3 [116].

The measured Vickers hardness of the Ta_2AlC and mixed samples scatter considerably, as shown in Figure 45 in a scatterplot with all HV values per sample. The hardness varies from 486 to 552 HV for Ta_2AlC, and from 372 to 531 for mixed samples. The measured values are however in rough agreement with values stated in literature; 448.7 ± 10.2 HV for Ta_2AlC [66] and 520 ± 10.2 HV for Ta_4AlC_3 [83]. Similar for the measured density of the samples, the Vickers hardness is not notably higher for the mixed samples.

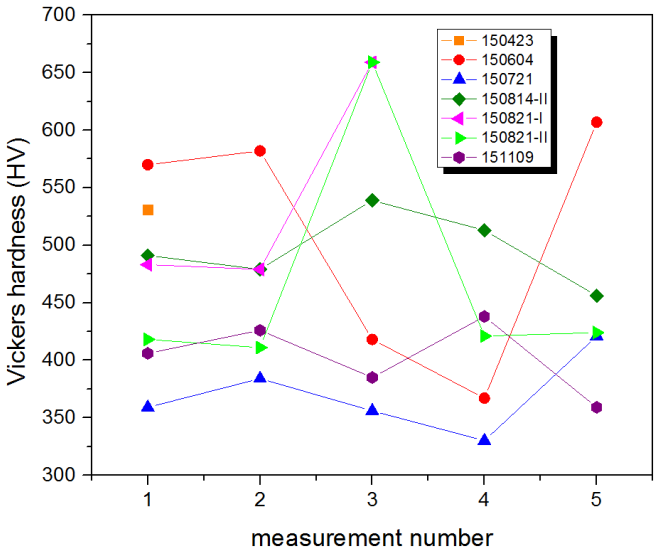

Figure 45: Measured Vickers micro hardness value (HV) versus measurement number, for all samples measured.

Several reasons could cause the observed scatter between the HV measurements on one sample (max. 5 per sample) and between different samples. The diameter of the indents lies approximately in the range of 40 to 60 µm. The length of the elongated grains of mixed samples was observed to be in the order of 10 µm, and the width in the order of several µm. A similar grain size is assumed for the MAX phase material in the Ta_2AlC samples. Hence, the indent size might be slightly small compared to the size of individual grains in the sample, which could cause scatter in the measured HV hardness due to placing of grain boundaries and other local discontinuities and differences of the microstructure within indents. Furthermore, the Al_3Ta impurities observed in the Ta_2AlC samples reach a size in the same order of the indent diameter (see Figure 23). It has however been attempted to avoid indentation of Al_3Ta impurities. In retrospect, a higher load for Vickers micro indentation might have resulted in less scatter because the indent size would have been larger.

For some samples the surface could not be placed exactly perpendicular to the indenter, due to non-parallel sample surfaces after grinding. This was observed clearly for sample 150721, for which a relatively high hardness is measured. Furthermore, possible difference in grain size between the different samples has not been analysed in this work. However, based on available SEM images the grains appear to have roughly the same order of magnitude for all samples observed. An inhomogeneous microstructure could be another reason for scatter of Vickers hardness within one sample or between different samples. The Ta_2AlC samples have an unknown fraction and distribution of Al_3Ta impurity. Impurities have been observed on several locations on cross-sections of Ta_2AlC samples. For the mixed samples, the fraction of Ta_2AlC and Ta_4AlC_3 might vary slightly between samples and within samples. The latter was however not observed by SEM analysis of sample surfaces.

5.2 Microstructure and composition of oxide scale

Based on observation of the microstructure and fluctuating chemical composition of the oxide scale, and the literature review on oxidation of Ta, TaC, and Ta_2C given in section 2.6, inward oxidation is thought to take place in Ta-Al-C MAX phase at elevated temperatures, which presumably starts with dissolution and inward diffusion of oxygen into the MAX phase. It was found that oxide formation was caused by oxidation of tantalum, the 'M element' of the MAX phase, instead of the expected preferential oxidation of aluminium. Inward diffusion of oxygen seems to take place preferably along grain boundaries of the MAX phase material, based on the microstructure of the oxide scale as was shown in Figure 29. As time progresses, the remaining 'unoxidized' part of the grain oxidizes. Hence, within the oxide scale, fully oxidized (dark) grain boundary regions alternate with lighter and gradually 'less oxidized' regions that represent the bulk volume of the former MAX phase grain. Figure 46 represents a schematic overview of the process inward oxidation in Ta-Al-C MAX phase over time. The size of the alternating oxidized and bulk areas as shown in Figure 29 is of the same order of magnitude as the grain size in mixed samples, as identified in Figure 24, in the order of 10 µm. However, the elongation shape of grains as observed Figure 24 cannot be clearly distinguished from the shape of the light (bulk) and dark (oxidized) areas in Figure 29.

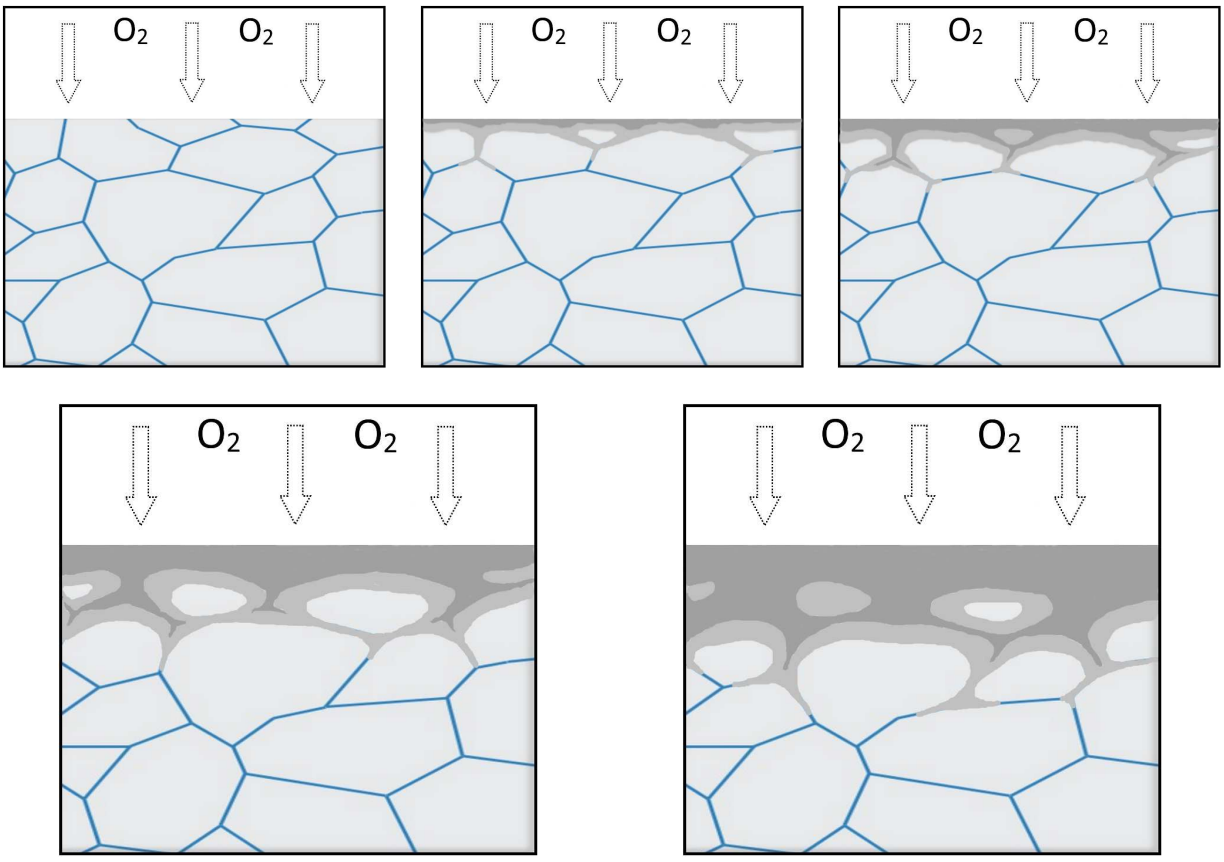

Figure 46: Schematic of inward oxidation over time, showing progressing inward oxidation in the images from left to right and top to bottom.

Isothermal oxidation of Ta-Al-C MAX phase within the temperature range of 600 to 800 °C does not result in the formation of a regular oxide scale with a homogeneous composition that matches any of the expected stable oxides. This follows from comparing the average atom percentages within the observed oxide scale as shown in Table 20, and those of the most expected stable oxide phases as shown in Table 25. Additionally, from XRD analysis of the surface of the oxidized TGA samples it can be concluded that the oxide scale formed in the 600 – 800 °C temperature range possibly consists in part of metastable tantalum-oxides. XRD analysis of the surface of the TGA sample oxidized at 600 °C only identifies MAX phase, even though – based on the material and radiation type – the minimum layer thickness that can be measured was reported to be 1.90 µm (for 2Θ = 40°) and 3.93 µm (for 2Θ = 90°) [117]. Several reasons are possible for the absence of clear oxide peaks: the presence of oxide particles which are too small to be detected; large peak broadening due to lattice distortions; complete absence of crystalline material within the oxidized layer. For the TGA sample oxidized at 700 °C peaks of Ta_2O_5, $Ta_{0.87}O_{1.5}$, and MAX phase material, are identified by XRD analysis. Possibly the oxidized layer is still thin enough on certain surface areas for the MAX phase material underneath to be identified too. Based on analysis of the microstructure of the oxide scale, it could also be that local areas with a crystal structure very similar to that of the Ta-Al-C MAX phase are present within the oxide scale, which could cause MAX phase to be identified by XRD analysis. Compared to the XRD results of virgin Ta_2AlC and mixed MAX phase, some of the XRD peaks corresponding to MAX phase materials of the oxidized TGA samples, appear to be slightly broadened. Distortions of the MAX phase crystal lattice could be caused by the presence of oxygen atoms which have diffused into the MAX phase. The oxide scale of the TGA sample oxidized at 800 °C was shown by XRD analysis to possibly consist of $TaO_{1.67}$ (also called 'δ-Ta_2O_5') or TaO.

XPS analysis of the binding energy of tantalum and aluminium on the surface of the bulk Ta-Al-C MAX phase samples isothermally oxidized at 600, 700, and 800 °C, shows that the binding energy of both tantalum and aluminium increases as the isothermal oxidation temperature increases (see Figure 31 and Figure 32). This suggest that the oxidation state of tantalum and aluminium increases as the isothermal holding temperature increases. No Al_2O_3 was identified by XRD or EDS analysis, but the results of XPS suggest that aluminium does oxidize during isothermal holding. Aluminium might be incorporated in metastable tantalum oxides or Ta_2O_5 in solid solution in the oxide scale formed in the 600 – 800 °C temperature range. At higher oxidation temperatures the ternary oxide $TaAlO_4$ has been identified, as a result of DTA of Ta-Al-C MAX phase powder non-isothermally oxidized until 1200 °C.

The binding energies found for Ta4f7/2 and Al2p are compared with the binding energy ranges reported by the Handbook of X-Ray Photoelectron Spectroscopy [118] for metallic Al and Ta and for their oxides. All the binding energies found for Al2p are too high to correspond to metallic Al, but for the samples oxidized at 600 and 700 °C – approximately 73.5 and 73.6 eV respectively – are also relatively low to correspond to aluminium oxide. For the sample oxidized at 800 °C, the binding energy of approximately 77.1 eV is very high to correspond to aluminium oxides, which are stated to fall between 74 and 75 eV [118]. For tantalum-oxide, the binding energy range for Ta4f7/2 in Ta_2O_5 is reported, in which tantalum has the maximum oxidation state of +5. It is reported to fall between approximately 26.3 and 27 eV [118]. The binding energies found in this work do not correspond to this margin. The binding energies for the samples oxidized at 600 and 700 °C are lower, with values of approximately 25.5 and 25.9 eV. The binding energy for the

sample oxidized at 800 °C is higher, with a value of approximately 29.5 eV. Especially the latter binding energy is surprising, as tantalum cannot oxidize to a higher state than +5, and hence no higher binding energy for the Ta4f7/2 subshell than 27 eV was expected to be found.

Literature review of oxidation of Ta_2AlC [84] hints towards the formation a largely X-ray amorphous oxide scale at 600 °C, and mixture of Ta_2O_5, $TaAlO_4$, and amorphous oxide above 700 °C, with increasing volume fraction of $TaAlO_4$ for higher isothermal oxidation temperatures. No $TaAlO_4$ was identified by XRD analysis after oxidation of Ta-Al-C MAX phase in the temperature range of 600 – 800 °C in this work. In literature, the Ta/Al ratio was found to remain the same for bulk and oxide scale, which is also the case for the oxide scales analysed in this work. The oxidation mechanism of Ta_2AlC or other Ta-Al-C MAX phases is not described in literature. Therefore, additionally oxidation of Ta, TaC, and Ta_2C has been studied in section 2.6.

The final oxidation product of Ta, TaC, and Ta_2C is Ta_2O_5. The Ta-O phase diagram as assessed by Garg *et al.* [85] and discussed in section 2.6 shows that the solubility of O in Ta does not exceed 3 at.% in the temperature range of 600 to 800 °C, and that the equilibrium phases are Ta + β-Ta_2O_5 when the at.% of O becomes higher than 3. However, many metastable Ta-O oxides have been experimentally observed and reported in literature as reviewed by Garg *et al.* [85]. Oxidation of Ta is reported to happen in three steps; formation of a thin layer saturated with oxygen, followed by formation of a suboxide layer (precise stoichiometry unknown), on which Ta_2O_5 forms [88]. The oxidation mechanism of TaC is not clearly stated. No carbon is found in the oxide scale of TaC, and hence a direct reaction to form CO_2 upon oxidation of TaC is assumed [94]. Oxidation of Ta_2C is described to happen via the formation of a 'general oxycarbide' (TaC_xO_y) layer at the MAX phase-oxide interface, which preferentially grows at Ta_2C grain boundaries [94].

The Loriers paralinear oxidation model proposed for Ta_2C [94] (see section 2.6) can possibly also explain the oxidation mechanism of Ta_2AlC as observed in this work, as it fits with the observation of apparent gradual grain boundary oxidation as shown in Figure 29, and by the gradually increasing O content and decreasing C content as shown in Table 21. However, no proof for the presence of an oxycarbide layer on the oxide/MAX phase interface was found in this work. Analysis of the change of composition when moving from unoxidized MAX phase into the oxide scale do not show the presence of an intermediate layer between oxide scale and underlying MAX phase at the oxidation front, as can be seen in the line scans made by X-ray microanalysis shown in Figure 30. Instead, the transition from bulk MAX phase composition to oxide scale takes place over a very small region of 2 µm. It is expected that this is the result of a small saturation region of the MAX phase with oxygen, and that this steep 'oxidation front' moves further inward upon ongoing oxidation into the bulk MAX phase. It is not clear why a steep oxidation front is observed at the oxide scale/MAX phase interface, but at the same time apparent gradual oxidation is observed for remaining MAX phase grains 'trapped' within the oxide scale after initial oxidation of the grain boundaries.

Literature review of oxidation of Ta_2AlC and pure Ta shows that various metastable oxides and/or an amorphous oxide phase might form at the lower temperature range, which could also be the case for the oxides found in this work after isothermal oxidation at 600, 700, and 800 °C.

As no notable differences are observed between the oxide scales on Ta_2AlC and mixed samples, it is assumed that the oxidation mechanism and oxidation products of Ta_2AlC and Ta_4AlC_3 are similar. Furthermore, the Al_3Ta impurities in the Ta_2AlC samples do not seem to affect the oxidation of the surrounding Ta_2AlC matrix.

Table 25: At.% of Ta, Al, and O, and CTE of most expected oxide phases.

	Ta	Al	O
$TaAlO_4$	17	17	67
Ta_2O_5	29	0	71
TaO_5	33	0	67
TaO	50	0	50

Unlike the oxidation of Ti_2AlC and Cr_2AlC – where outward oxidation and formation of mainly Al_2O_3 takes place on the original surface of the bulk material – oxidation of Ta-Al-C MAX phase apparently moves inward, and does not result in a protective oxide scale of homogeneous composition within the temperature range of 600 – 800 °C. Inward oxidation is found more commonly for metals with a relatively high oxygen solubility [119].

The relative volume expansion upon oxidation (RVE) has been determined for two cases: 1) conversion of MAX phase into Ta_2O_5 only, and 2) conversion of MAX phase into Ta_2O_5 and the maximum possible (based on stoichiometry of the reaction) amount of $TaAlO_4$. These oxides are chosen because they are the only two oxides identified after full oxidation of Ta_2AlC powder with DTA, as described in section 4.4, and hence are assumed to be the closest 'educated guess' to the oxides formed in the 600 – 800 °C range during isothermal oxidation. The calculated RVE's are shown in Table 26, and show a relative volume expansion higher than 50%[2]. The high RVE upon oxidation corresponds well with the observed microstructure of the oxide scales on TGA samples after isothermal oxidation at 700 and 800 °C which are highly porous (see Figure 26).

Table 26: RVE upon oxidation of Ta_2AlC and Ta_4AlC_3 for conversion into 1) Ta_2O_5 and 2) into Ta_2O_5 and $TaAlO_4$.

	RVE for conversion into Ta_2O_5	RVE for conversion into Ta_2O_5 & $TaAlO_4$
Ta_2AlC	1.55	2.00
Ta_4AlC_3	1.77	2.02

The formation of large cracks in the oxide scale, as shown in Figure 27. are assumed to be caused by internal stresses due to a mismatch of the CTE of the MAX phase matrix and the oxide scale. CTE values as reported in literature for Ta_2AlC are $8.0 \cdot 10^{-6}$ K^{-1} [66], and $5.7 \cdot 10^{-6}$ K^{-1} (25 – 1000 °C range) [84] (see section 2.5). For Ta_4AlC_3 a CTE of $8.2 \pm 0.3 \cdot 10^{-6}$ K^{-1} [83] was reported. Not for all oxides shown in Table 25 a CTE has been reported in literature; Table 27 shows the information available, including references. The CTE values found for the bulk MAX phase material is in all cases significantly higher than the CTE values found for β-Ta_2O_5 and TaO. Therefore, compressive stresses will be induced within the oxide scale upon cooling of the TGA samples to room temperature.

[2] See Appendix 8 – Calculation of RVE upon oxidation of Ta-Al-C MAX phase

Table 27: Literature values of the CTE of Ta_2O_5 and TaO, incl. method of measurement and reference.

Oxide	**CTE (**$\cdot 10^{-6}$ K^{-1})	**Method**	**Reference**
B-Ta_2O_5	2.9 (25 – 550 °C) 4 (550 – 1200 °C)	Dilatometry	[120]
TaO	3.00 (unreported temperature range)	XRD	[121]

Uneven oxidation on the surface of the bulk Ta-Al-C MAX phase samples – as illustrated in Figure 28 – has also been reported for oxidation of bulk tantalum [88]. Kofstad *et al.* has explained the rounding off of sample edges by the fact that oxygen dissolution and diffusion happens from both sides. The rounded corners of the cross-sections observed in this work are assumed to be caused by the same mechanism. It can however not be explained why some corners have not been oxidized at all, as can be seen in Figure 28b and c, and further research is needed to answer this question.

The fact that the Ta/Al ratio stays roughly the same for the different regions of the oxide scale and bulk material, shows that no large scale redistribution of Ta or Al takes place within the microstructure upon oxidation in the 600 to 800 °C temperature range. For example, there is no separation into different oxides on a length scale in the order of tens of µm. Also, this result supports the lack of a depletion zone of the A-element on the MAX phase/oxide interface.

5.3 Oxidation reactions and activation energies

Two exothermal chemical oxidation reactions were observed when heating Ta-Al-C MAX phase powder until 1200 °C, and only after the second reaction the MAX phase powder is fully converted into the oxidation products Ta_2O_5 and $TaAlO_4$. Based on mass spectrometer analysis , carbon reacts with oxygen during the second reaction, after which it leaves the sample in gaseous form as CO_2. The small 'dip' in the weight gain curve (see Figure 33) during the second oxidation reaction, is hence assumed to correspond to the loss of carbon from the MAX phase powder. The dip in the weight gain curve reaches a maximum of approximately 1.5 mg below the expected value, in case of the absence of the dip. The mass of the element carbon in 30 mg of Ta_2AlC powder is approximately 1 mg. The order of magnitude of the dip in the weight gain curve thus corresponds well to the mass of carbon in the DTA powder before oxidation.

XRD analysis after the first reaction identified unreacted Ta_2AlC, and the phases $TaO_{1.1}$, Ta_4C_3, and $Ta_{1.86}Al_{0.14}O_{4.86}$. This indicates that full conversion of the MAX phase takes place via a number of metastable intermediate oxide and carbide phases. In comparison, DTA of pure Ta and TaC powder shows one exothermal reaction upon oxidation, during which Ta_2O_5 is formed, and in the case of TaC during which C is oxidized to gaseous CO_2 at the same time.

The Kissinger analysis is performed on Ta_2AlC, Ta, and TaC powder to determine the activation energy of each observed reaction. The method of DTA can be used only for simple decomposition reactions to determine E_a, regardless the order of the reaction [122]. If multiple reactions take place at the same time, or if the reaction mechanism changes within the measured temperature range, the Kissinger analysis might not result in an accurate value for E_a.

The Kissinger points for the first oxidation reaction in Ta_2AlC show a very good linear fit, which result in a small 95% confidence interval. The activation energy of the first reaction of Ta_2AlC oxidation has been determined from experimental data in three ways (as discussed in section 4.4), resulting in the values 145.7 ± 10.0, 216.5 ± 15.8, and 129,3 ± 35.9 kJ/mol. It stands out that the activation energy calculated via dTG/dt peak analysis differs notably from the other two values. This is caused by the fact that the peak in the dTG/dt curve so apparently the weight gain over time does not change in the same manner as the heat flow, when changing the heating rate of DTA. The activation energy which is experimentally determined for the second observed exothermic reaction in the MAX phase powder is unreasonably high; 1429.0 kJ/mol (determined from heat flow peak temperature), and 1602.6 kJ/mol (determined from dTG/dt peak temperature). The peak temperature at which the second oxidation reaction has its peak does not vary significantly for different heating rates. Based on the phases identified by XRD after the first and second reaction have taken place, full oxidation into Ta_2O_5 and $TaAlO_4$ takes place during the second reaction, as well as formation of CO_2. Hence, it can be said that the second oxidation reaction cannot qualify as a 'simple decomposition reaction' and might therefore not result in a reasonable value for E_a. It should however be noted, that with this reasoning the first oxidation reaction also isn't a simple decomposition reaction, as different oxides and carbides were identified by XRD ($TaO_{1.1}$, Ta4C3,$Ta1_{.86}Al_{0.14}O_{4.86}$). Nevertheless Kissinger analysis does result in a reasonable value for E_a. For both observed reactions, it is unknown what the exact reaction path is.

Kissinger analysis of pure Ta results in an E_a of -305.3 ± 88.2 (heat flow peak temp) and -286.6 ± 98.0 kJ/mol (dTG/dt peak temp), so both methods result in a relatively big 95% confidence interval based on the linear fit. The activation energies reported in literature for oxidation for Ta is 183 ± 8 kJ/mol [91] (for initial parabolic oxidation), which is considerably lower than the E_a determined in this work. The bonding of Ta with C and Al in Ta-Al-C MAX phase appears to increase the activation energy for oxidation.

The Kissinger analysis of TaC powder has to be disregarded, as the Kissinger points do not fit well enough on a linear line, resulting in a very large 95% confidence interval. As it was shown that oxidation of Ta to form Ta_2O_5 and oxidation of C to form gaseous CO_2 take place at the same time during oxidation of TaC, oxidation of TaC apparently does not follow a simple decomposition reaction either. The activation energies reported in literature for TaC and Ta_2C are respectively, 379 ± 16 kJ/mol [94] (in the 750 – 850 °C range, based on experimentally determined weight gain), and 129 ± 7 kJ/mol [94] (also in the 750 – 850 °C range). It can be noted that the activation energy for oxidation of Ta_2C as reported in literature is close to the activation energy as calculated in this work for the first reaction taking place in Ta_2AlC.

5.4 Oxidation kinetics

The observed oxidation kinetics (based on weight gain over time, for isothermal holding of bulk samples) shows initial behaviour that resembles parabolic oxidation, followed shortly by near linear oxidation behaviour for the remaining holding time for the temperature range of 600 – 800 °C. Initial parabolic behaviour is most visible for the bulk sample oxidized at 600 °C, as was shown in Figure 39. Initial parabolic behaviour was also reported in literature for oxidation of Ta, TaC, and Ta_2C (see section 2.6). This is ascribed to the formation of an initially dense Ta_2O_5 layer [88] (for Ta) or a more generally described 'multi-layered scale with inner compact oxide' [94] (for Ta_2C). Initially, the growth of a dense oxide layer follows parabolic behaviour because diffusion of oxygen through the dense oxide scale is the rate-limiting process. Upon further oxidation, it was proposed that the oxide scale cracks, and forms pores due to internal stresses (proposed for Ta), or that the protective oxide is further oxidized into an oxide with no protective qualities (proposed for Ta_2C). In the latter case, there is a possibility that a protective 'intermediate dense oxide layer' still exists between the MAX phase and porous oxide. However, when the thickness of this dense layer stays the same, oxidation kinetics remain linear. The porous nature of the eventual oxide scale explains linear kinetics for ongoing oxidation: oxygen keeps reaching the oxide/MAX phase interface within the same time because it does not have to diffuse through an increasing dense oxide scale, but can reach the interface by convection. Based on the results shown in Figure 39, the same oxidation kinetics – and hence mechanism – is assumed for Ta_2AlC and mixed Ta-Al-C MAX phase.

It was shown that calculation of oxide layer thickness based on the measured mass gain over time and the densities of known stable oxides (see Figure 40), results in a calculated oxide scale thickness of approximately a factor 10 thinner than the observed thickness on the samples. It is assumed that this discrepancy is caused by the extra volume of pores and cracks within the observed oxide scales.

5.5 Self-healing potential of Ta-Al-C MAX phases

From the results of section 4.6 was shown that Ta-Al-C MAX phase does not have self-healing capabilities by filling of cracks with a stable, dense, protective oxide. Because oxidation of bulk MAX phase only showed a visually dense oxide scale for oxidation at 600 °C, the crack healing experiment was also performed at 600 °C. At higher temperatures it is expected that the oxide scale which forms does not have any self-healing properties because it is porous and non-protective, as was shown in section 4.3. However, as shown in Figure 41, SEM images of the oxidized crack do not show consistent crack-filling. The load displacement curves (see Figure 44) have shown that the load-bearing capability of the cracked sample is not increased after oxidation. Furthermore, the cascade of near vertical load drops of the load displacement curves indicates a combination of brittle and plastic deformation upon crack-formation.

6. Conclusions & Recommendations

6.1 Conclusions

The first goal of this work was to find a synthesis route to synthesize dense bulk predominantly single-phase Ta_2AlC MAX phase. The best results for synthesis of dense bulk single-phased Ta_2AlC have been achieved with SPS of elemental powders (ratio Ta : Al : C = 2 : 1.2 : 1) at 1400 °C and a pressure of 50 MPa for 30 minutes in argon atmosphere, for a sample diameter of 20 mm. SPS in argon atmosphere instead of vacuum strongly reduces the amount of internal oxides in the resulting sample. It was found that the addition of an intermediate heating step at 700 °C and 5 MPa (minimal pressure during SPS) before sintering at 1400 °C helps to avoid major loss of liquid Al from the powder compact, as a significant fraction of Al is otherwise squeezed out of the powder compact during sintering at 50 MPa. It is believed that the intermediate heating step facilitates the formation of solid intermetallic Al_3Ta from molten Al (melting point ≈ 660 °C) and Ta. Presumably a large fraction of Al_3Ta transforms to Ta_2AlC during sintering at 1400 °C via an unknown chemical reaction path. XRD analysis of the sample surface only identifies Ta_2AlC, but imaging of cross-sections with SEM show a varying fraction of Al_3Ta to be present in the samples after synthesis by SPS.

Changing of the sinter temperature from 1400 to 1500 °C results in a dense bulk Ta-Al-C MAX phase sample with alternating elongated grains of Ta_2AlC and Ta_4AlC_3. No Al_3Ta impurities are identified in these 'mixed' samples. It is assumed that for sintering at 1500 °C, a larger fraction of liquid Al is squeezed out of the powder compact during sintering, as Ta_4AlC_3 has a smaller atom fraction of Al. Individual grains are observed to have a length in the order of tens of μm, and a width of several μm. The grain size of Ta_2AlC was not observed clearly by SEM due to lack of contrast between different grains (as observed with SEM), but is assumed to be in the same order of magnitude.

It was found that increasing the diameter of the SPS sample results synthesis of mixed MAX phase instead of predominantly single-phase Ta_2AlC, when using the exact SPS process parameters that resulted in Ta_2AlC for samples of 20 mm diameter. Inhomogeneous sample heating for samples with a bigger diameter, where temperatures above the set sintering temperature are reached, could explain these results.

All SPSed samples of Ta_2AlC and mixed composition approach the theoretical density values for Ta-Al-C MAX phases as mentioned in literature (Ta_2AlC and Ta_4AlC_3), and no porosity is observed with SEM. The Vickers Hardness as measured with the HV microhardness method on Ta_2AlC and mixed samples shows considerable scatter but does roughly correspond to literature values reported for Ta_2AlC and Ta_4AlC_3. It stands out that no significant difference in hardness and density is measured between Ta_2AlC and mixed samples, because reported literature values are different for Ta_2AlC and Ta_4AlC_3.

The second goal of this work was to analyse the oxidation behaviour of Ta-Al-C MAX phase, and report on its potential for self-healing. Oxidation of Ta_2AlC and Ta_4AlC was observed to be directed inward, and first takes place along the grain boundaries. Mainly tantalum oxides are

formed, instead of the expected formation of Al_2O_3 by preferential A-element oxidation. The remaining bulk of the grains is oxidized gradually over time, following the initial oxidation of the grain boundaries, presumably after sufficient diffusion and dissolution of oxygen to form a thin saturated layer at the MAX phase surface (comparable to the oxidation mechanism of pure tantalum and TaC). Isothermal oxidation at 600, 700, and 800 °C for 10 hours in dry artificial air results in an oxidized scale with varying thickness along the sample surface, and a maximum observed thickness of 10-15, 30, and 250 µm, respectively. The strong variation of the oxide scale thickness across sample surfaces of individual samples is not explained in this work. No differences in oxidation behaviour were observed between Ta_2AlC and mixed samples. The oxide scales formed at 700 and 800 °C are highly cracked and porous. The cracks are likely caused by the large stresses generated due the relative volume expansion upon inward oxidation. This relative volume expansion was calculated for two hypothetical cases for Ta_2AlC and Ta_4AlC_3, namely: oxidation into β-Ta_2O_5, and oxidation into a combination of β-Ta_2O_5 and $TaAlO_4$. In all calculated cases the calculated relative volume expansion is higher than 55 %. The relative volume expansion is assumed to also be relatively high for conversion to other metastable tantalum-oxides. The oxide scale formed at 600 °C after 10 hours of oxidation does not show porosity.

The composition of the oxide scales formed in the 600 – 800 °C range do not show an ambiguous match with particular stable tantalum-oxides, or the ternary $TaAlO_4$ oxide. The composition of the oxide scales have been analysed by XRD and X-ray microanalysis with EPMA. XRD analysis of the oxide scale formed at 800 °C suggest the presence of $TaO_{1.67}$ (also called 'δ-Ta_2O_5') or TaO. The composition of the oxide scales formed on bulk Ta-Al-C MAX phase formed at 600 and 700 °C as analysed by XRD and X-ray microanalysis does not correspond well to known tantalum- (Ta_2O_5, TaO_2, TaO), and ternary-oxides ($TaAlO_4$). Local differences in composition are observed between locations within the oxidized scale which are thought to represent grain boundaries, and locations corresponding to the bulk volume of the grain which have not been fully oxidized. Based on the results from XPS analysis, aluminium is assumed to be present within the oxide scales formed in the 600 – 800 °C range in oxidized state. Furthermore, the oxidation state of Al and Ta are both increasing with an increasing isothermal oxidation in the 600 – 800 °C range, as the binding energies have been observed by XPS to increase. It should be noted that the binding energies of Ta and Al for the sample oxidized at 800 °C are found to be higher than the binding energy margin for Ta_2O_5 and Al-oxides as reported by the Handbook of X-Ray Photoelectron Spectroscopy [118].

Two exothermal oxidation reactions are observed to take place upon oxidation of Ta_2AlC and mixed MAX phase powder (by DTA). After the first reaction of in Ta_2AlC has taken place (Ta_2AlC heated till 800 °C), unreacted Ta_2AlC, $TaO_{1.1}$, Ta_4C_3, and $Ta1_{.86}Al_{0.14}O_{4.86}$ was identified by XRD. After the second reaction has taken place, for heating to 1200 °C, β-Ta_2O_5 and $TaAlO_4$ is identified by XRD. Carbon oxidized to gaseous CO_2 during the second oxidation reaction. Hence, full oxidation of Ta-Al-C MAX phase leads to formation of β-Ta_2O_5 and $TaAlO_4$. Based on these results, full oxidation of Ta_2AlC and Ta_4AlC_3 into its stable oxides is thought to take place via a series of intermediate reactions of oxygen within the MAX phase, during which several metastable oxides can form. These metastable oxides start to transform into β-Ta_2O_5 and $TaAlO_4$ when the MAX phase is further heated above approximately 900 °C.

The observed kinetics of oxidation in the 600 – 800 °C temperature range shows initial oxidation resembling parabolic oxidation, followed shortly thereafter by linear oxidation. Linear oxidation behaviour is assumed to be caused by pore formation due to the high RVE upon oxidation. During initial oxidation, no pores have yet formed and oxygen diffusion into the bulk MAX phase is the rate-limiting process.

The activation energy of both reactions have been analysed, but could only be estimated in a meaningful way for the first oxidation reaction that was observed with DTA to take place. Three different approached result in different values for E_a (145.7 ± 10.0, 216.5 ± 15.8, and 129.3 ± 35.9 kJ/mol). The difference between the calculated E_a for using the three methods is relatively large. Compared to the activation energies reported in literature for initial oxidation of Ta, Ta_2C, and TaC, the calculated E_a shows roughly the same order of magnitude. Initial oxidation refers to the initial time period during which oxidation is observed to resemble parabolic kinetics.

Analysis of the oxidation of Ta and TaC, for comparison to Ta-Al-C MAX phase oxidation, shows full conversion to Ta_2O_5 by a visually single exothermic oxidation reaction during which carbon was observed to oxidize to gaseous CO_2.

Dense bulk Ta_2AlC and Ta_4AlC_3 MAX phase do not possess self-healing capabilities, based on the experiment conducted in this work. Crack formation, oxidation, and re-opening of a microcrack in a mixed sample showed no increase of mechanical load bearing capability after oxidation.

6.2 Recommendations

In order to gain further insight in the reactions taking place between the powder constituents during Ta-Al-C MAX phase synthesis by SPS, it is recommended to stop the SPS run at various stages during synthesis, and identify the phases present in the sample. As a start, this should be done at the beginning and end of the intermediate holding step at 700 °C, and at the start of sintering at T_{sinter}. To be able to sinter single-phase dense bulk Ta_2AlC by a similar SPS route, the formation and conversion of Al_3Ta intermetallic should be better understood. Similar test runs by SPS are recommended for 40 mm samples, to observe the difference in microstructural evolution during sinter in comparison to 20 mm samples, as a different sample size was found to result in different Ta-Al-C MAX phases in the final sample.

Also, further testing with small changes in the intermediate holding temperature and time, and final sinter temperature and time are recommended to further improve the avoidance of liquid Al leakage from the powder compact during sintering.

EBSD analysis of SPSed samples is recommended to determine the grain size, in order to check whether the grain size of Ta_2AlC and mixed samples is indeed similar, and to verify the grain sizes observed by SEM in the mixed samples. Additionally, possible local differences in microstructure could be observed, and possible difference is grains size between different samples fabricated with the same SPS program could be identified. This helps to determine the repeatability of synthesis by SPS.

Furthermore it is recommended to perform additional microhardness and density measurement after taking measures to reduce scatter. For density measurement this could be

done by using bigger sample pieces (preferably the entire SPS sample before cutting into smaller pieces for other purposes). This requires synthesis of new samples. For Vickers microhardness indentation, it is recommended to test scatter for a higher indentation load. In this work VH1 is used (load of 1 kgf). A higher load results in bigger indentations, and possible less effect of local inhomogeneity's in the sample microstructure.

After the study on the oxidation behaviour of Ta-Al-C MAX phase performed in this work, several question remain. Based on the results of this work, it is not yet understood what the precise reaction mechanism for oxidation of Ta_2AlC and Ta_4AlC_3 is. It is recommended perform additional DTA runs and measure multiple Ta_2AlC powder samples by XRD after oxidation to 800 °C, to check if XRD consistently identifies the same phases. Furthermore, analysis of the powder just before the second oxidation reaction takes place is recommended, to see if the phase-composition has changed between the end of the first oxidation reaction and start of second reaction. The use of SEM with EDS, and X-ray microanalysis with EPMA has shown the presence of aluminium within the oxide scales formed in the 600 – 800 °C temperature range. The XPS results suggest an increasing ionisation state for Al when the isothermal oxidation temperature is increased. Further research could be performed to find out if Al is incorporated in the oxide scale in solid solution, or in a different manner.

Furthermore, it is unclear what causes the highly irregular oxidation of the sample surface of Ta_2AlC and mixed dense bulk samples. Certain areas of the sample surfaces after isothermal oxidation in the 600 – 800 °C temperature range clearly show the presence of an oxide scale, while on other locations no oxide scale was observed with SEM on cross-sections. Further research is recommended to explain these results.

Further attempts to find the activation energy of the first and second oxidation reaction by the method that was used in this work is not recommended. This method has been reported to only produce valid results in the case of 'simple decomposition reactions', which do not consist of multiple parallel reaction mechanisms. As several different reaction products were observed after the first and second oxidation reaction, these are not believed to qualify as simple decomposition reactions.

Appendix 1 – Full sample overview of all synthesis attempts: XRD patterns & microstructure as observed by SEM

Pressure-less sintered samples: XRD pattern

PLS - Attempt 1

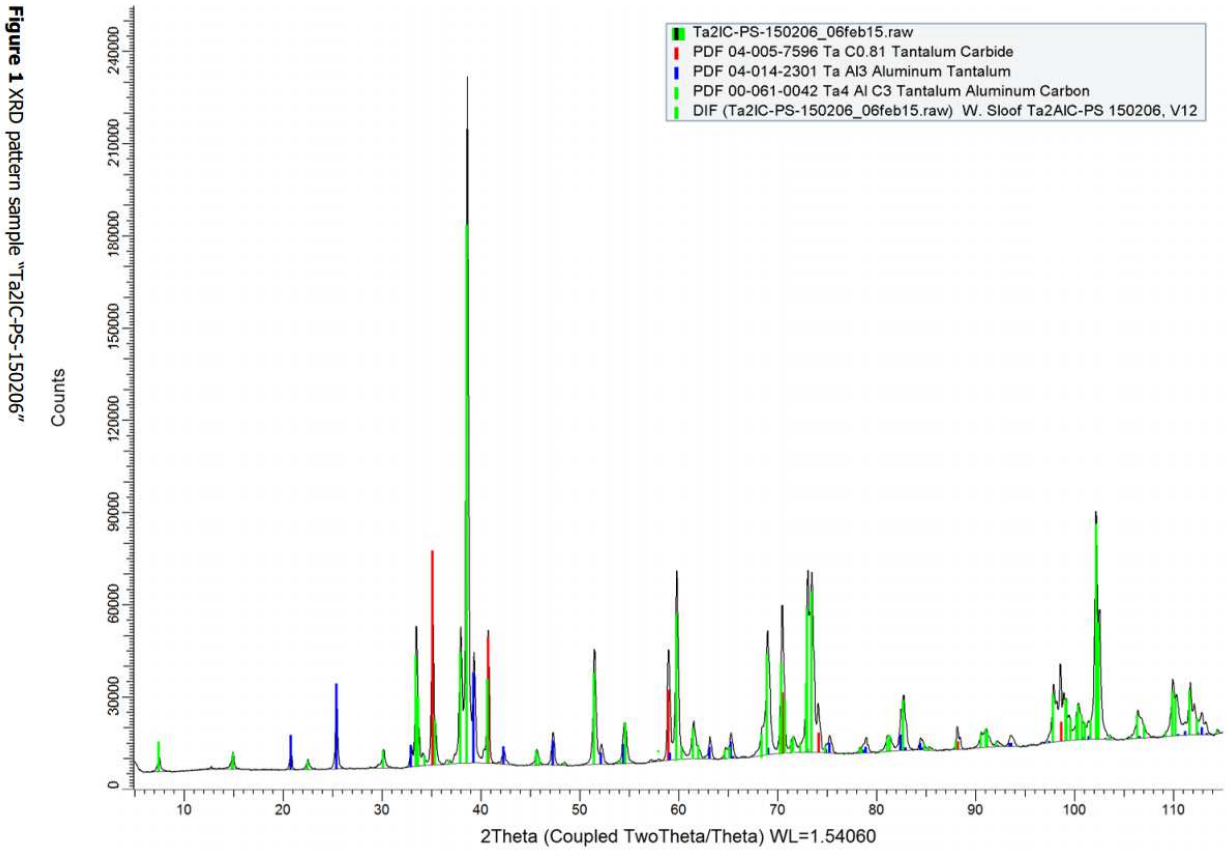

Figure 47: XRD pattern and fit for PLS sample 150206, sintered at 1400 °C for 1 hour in flowing argon, from elemental powders with composition Ta : Al : C = 2: 1.15 : 1.

PLS - Attempt 2

sample	*compound*	
150305-Ta-Al-C_PS-1200C	Tantalum Carbide	Ta2 C
	Aluminum Tantalum Carbide	Ta5 Al3 C
	Tantalum Oxide	Ta0.97 O2
	σ-Aluminum Tantalum	Al Ta2

Table 1.

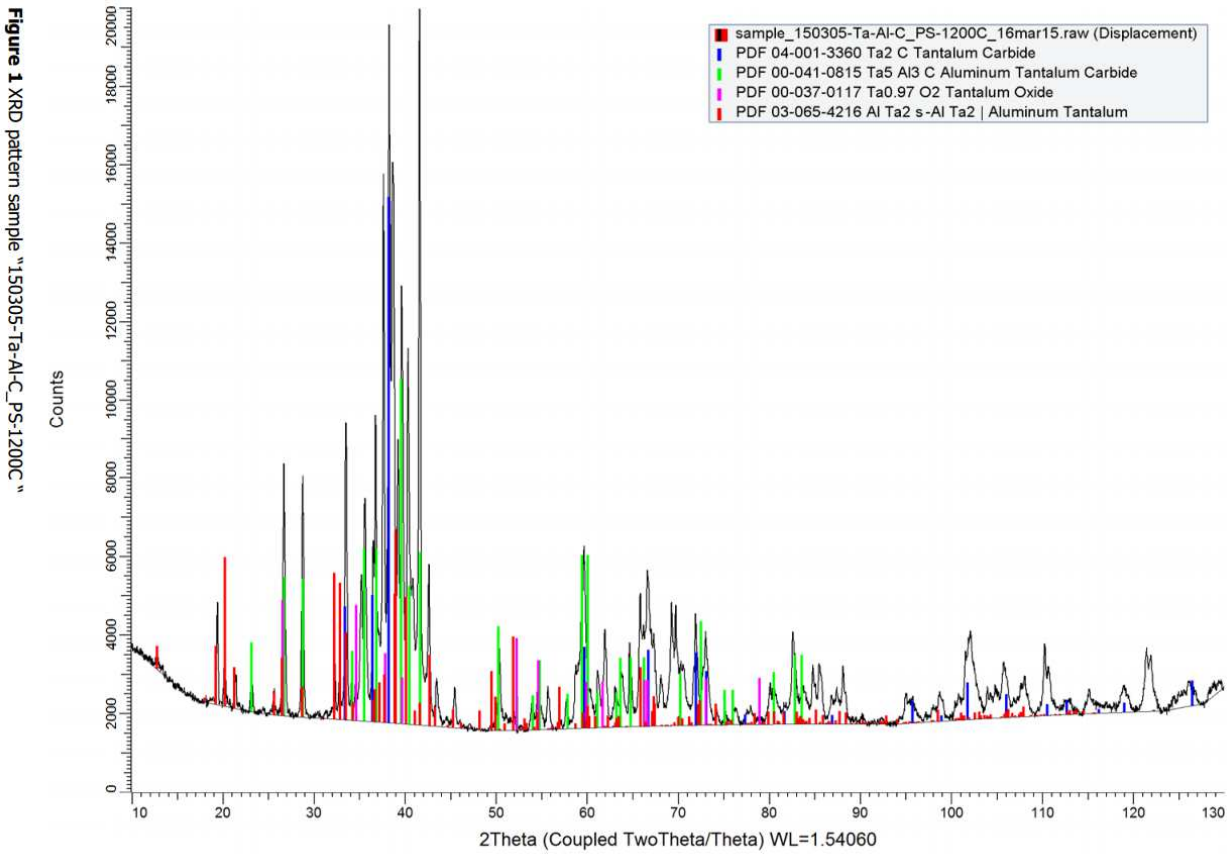

Figure 48: XRD pattern and fit for PLS sample 150305, sintered at 1200 °C for 1 hour in flowing argon, from elemental powders with composition Ta : Al : C = 2: 1.15 : 1.

PLS - Attempt 3

sample	*compound*	
150323-Ta-Al-C_PS-1500C	Tantalcarbide	Ta C
	α- Tantalum Aluminum Carbide	Ta4 Al C3
	Tantalum Aluminum Carbon	Ta2 Al C
	Aluminum Tantalum	Ta Al3

Table 1.

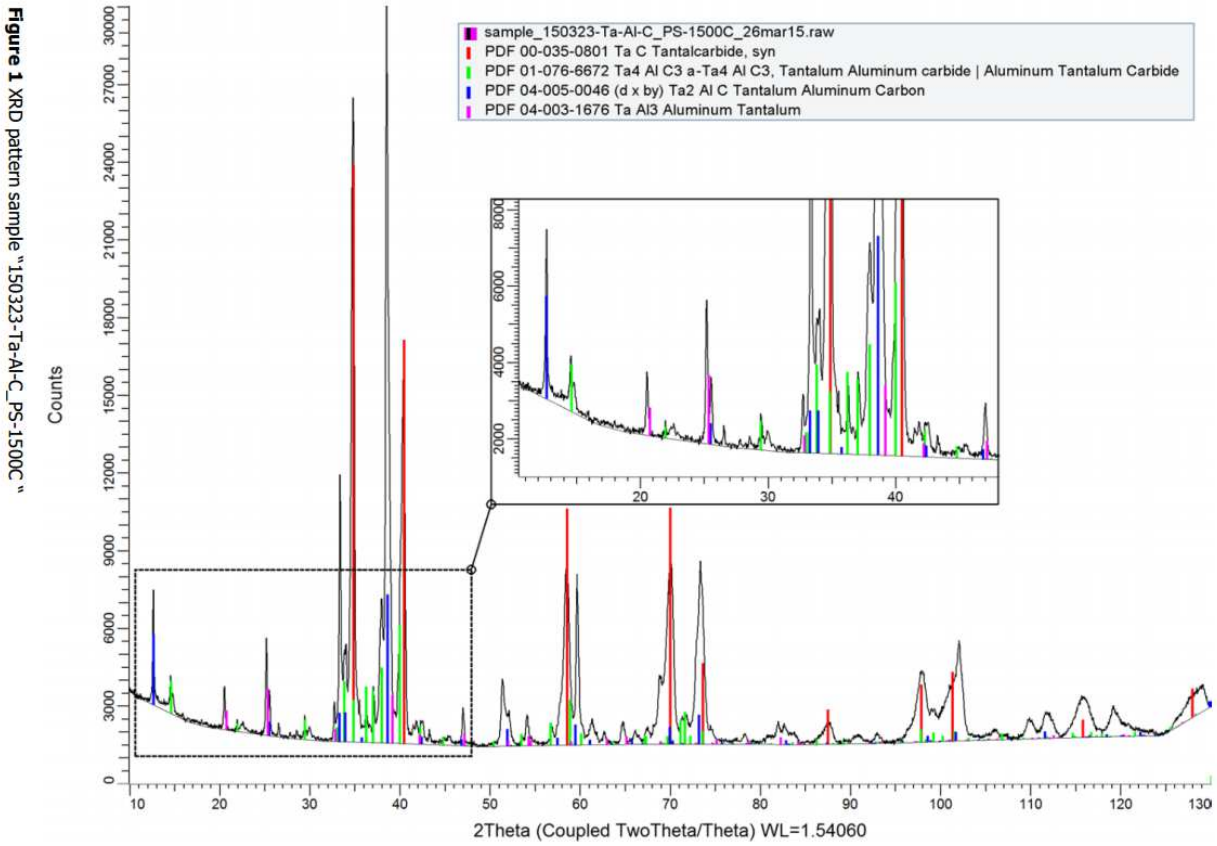

Figure 49: XRD pattern and fit for PLS sample 150323, sintered at 1500 °C for 1 hour in flowing argon, from elemental powders with composition Ta : Al : C = 2: 1.6 : 1.

SPS samples used for further research: XRD pattern & selection SEM images

All samples shown in this appendix are SPSed from elemental powders with composition Ta : Al : C = 2 : 1.2 : 1. In all cases a pressure of 50 MPa is applied during sintering at the maximum temperature. Other details on SPS synthesis are shown in Table 17.

Sample 150423 – mixed with internal oxides

sample	*compound*	
150423-Ta-Al-C_SPS-1500C 2nd-try	Tantalum Aluminum Carbon	Ta2 Al C
	Tantalum Aluminum Carbon	Ta4 Al C3
	α- Aluminum Tantalum Carbide	Ta4 Al C3
	Tantalum Aluminum Oxide	Ta0.5 Al0.5 O2
	Graphite	C

Table 1.

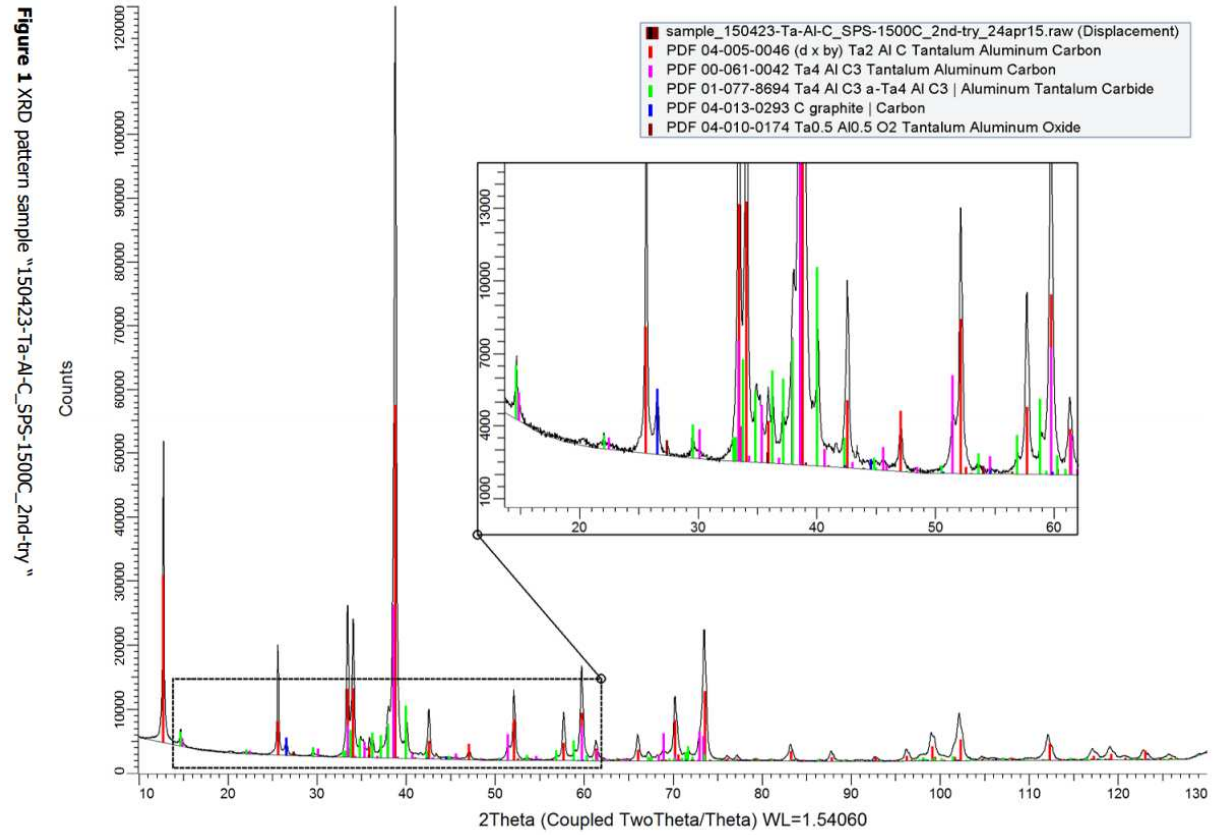

Figure 50: XRD pattern and fit for mixed SPS sample 150423.

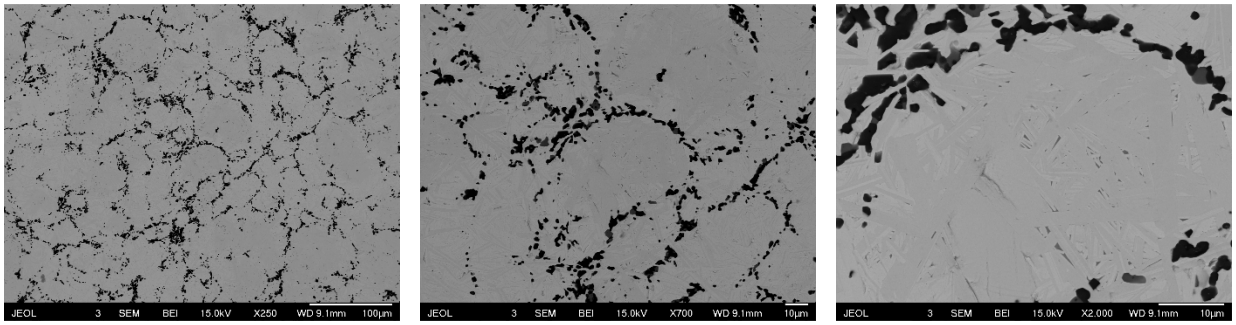

Figure 51: SEM backscatter images of the microstructure of mixed SPS sample 150423, internal oxides (black areas) are clearly visible, and appear to be present mainly on former grain boundaries of elemental Ta powder.

Note: internal oxides are clearly visible, and appear to be present mainly on grain boundaries. The grain boundaries are believed to correspond to those of the elemental tantalum powder grains, and the internal oxides have formed during densification of the powder compact.

Sample 150604 – mixed

sample	*compound*	
150604-Ta-Al-C_rapid-SPS-1500C	Tantalum Aluminum Carbon Tantalum Aluminum Carbon	Ta2 Al C Ta4 Al C3

Table 1.

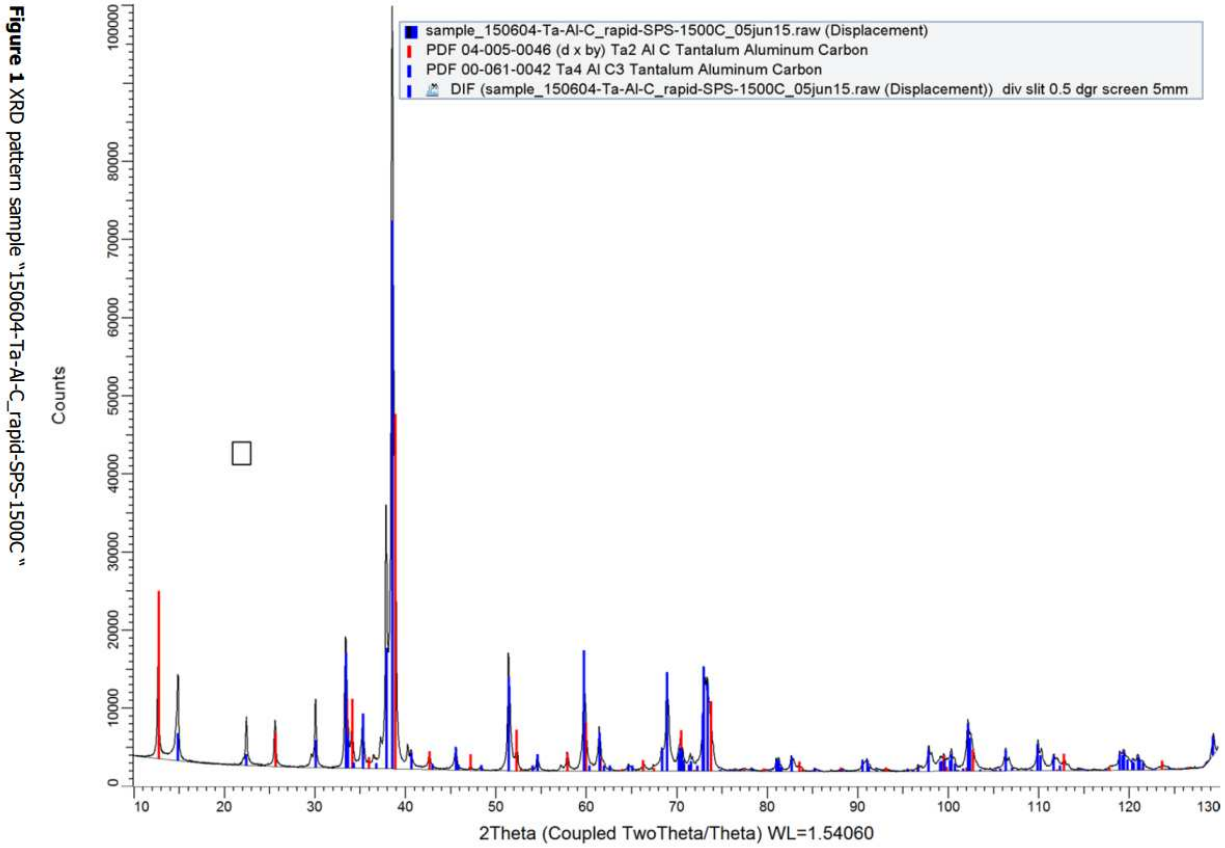

Figure 1 XRD pattern sample "150604-Ta-Al-C_rapid-SPS-1500C"

Figure 52: XRD pattern and fit for mixed SPS sample 150604.

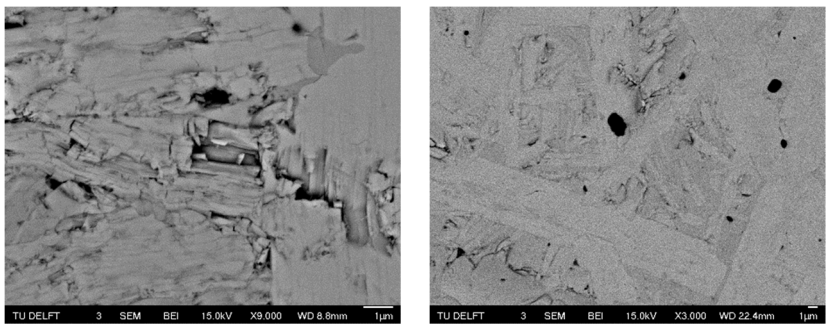

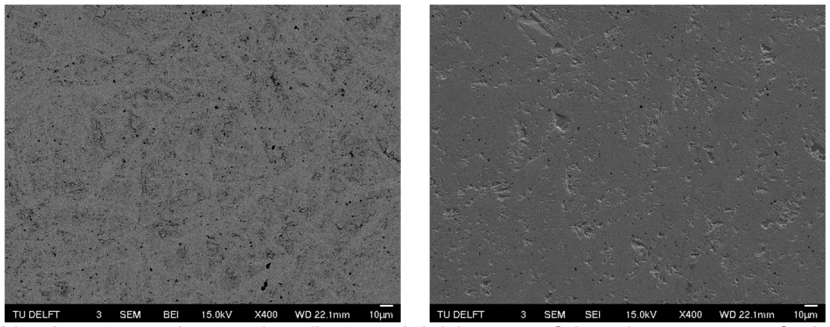

Figure 53: SEM backscatter and secondary (bottom right) images of the microstructure of mixed SPS sample 150604.

Sample 150721 – mixed

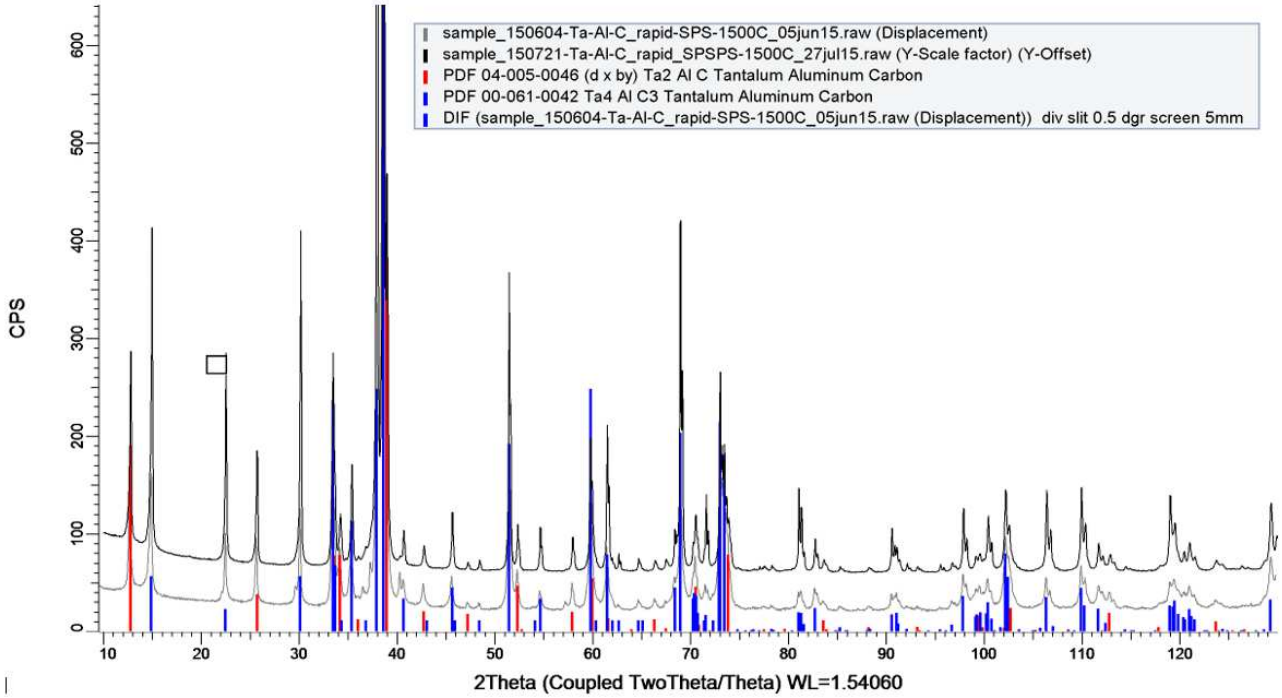

Figure 54: XRD pattern and fit for mixed SPS sample 150721.

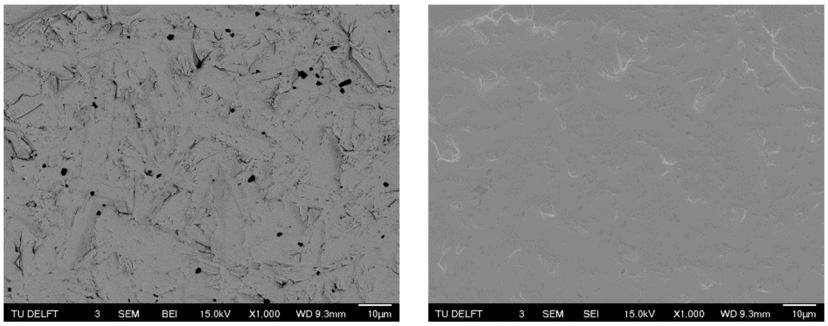

Figure 55: SEM backscatter and secondary image of the microstructure of mixed SPS sample 150721.

Samples 150814-I & II – Ta_2AlC (minor Al_3Ta impurities)

sample	*compound*	
150814-Ta-Al-C_SPS-1400C	Tantalum Aluminum Carbon Tantalum Aluminum Carbon	Ta4 Al C3 Ta2 Al C
150814-Ta-Al-C_SPS-1500C	Tantalum Aluminum Carbon Tantalum Aluminum Carbon	Ta4 Al C3 Ta2 Al C

Table 1.

150814-I (T_{sinter} = 1500 °C)

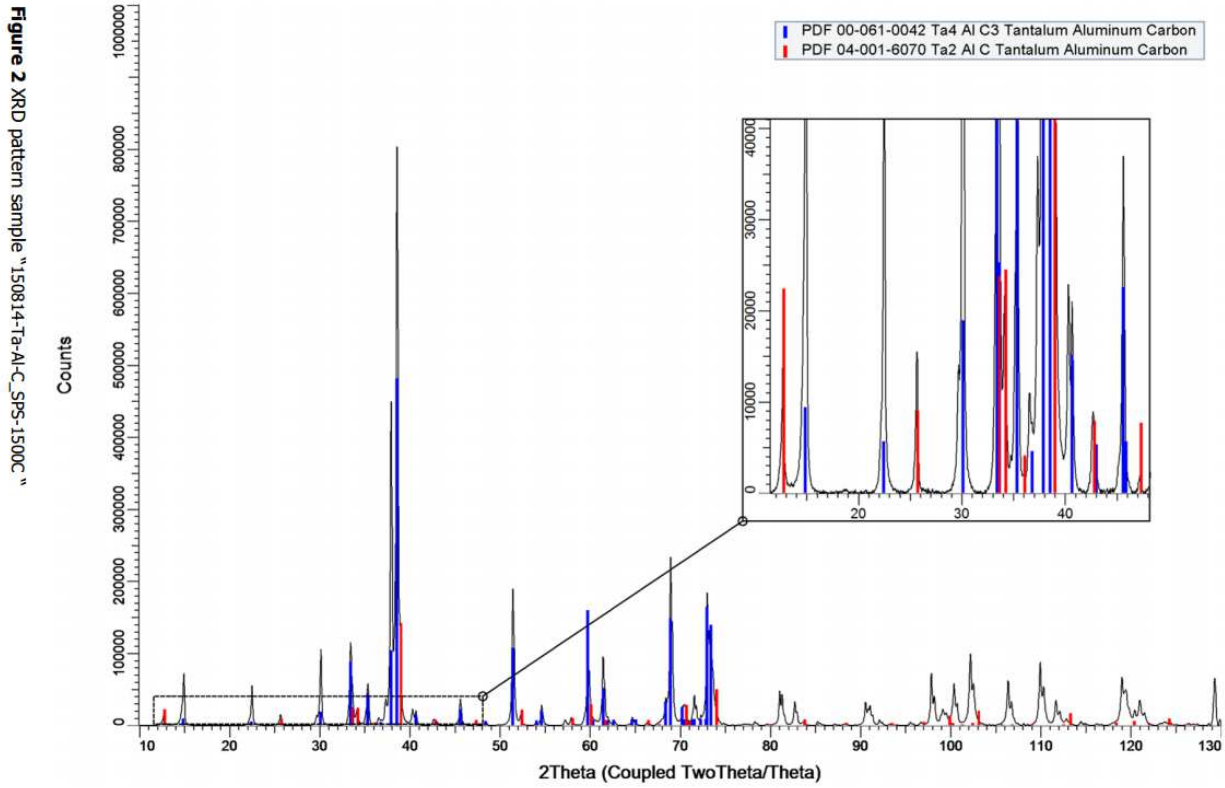

Figure 56: XRD pattern and fit for mainly Ta_2AlC SPS sample 150814-I.

No SEM images made

150814-II (T_{sinter} = 1400 °C)

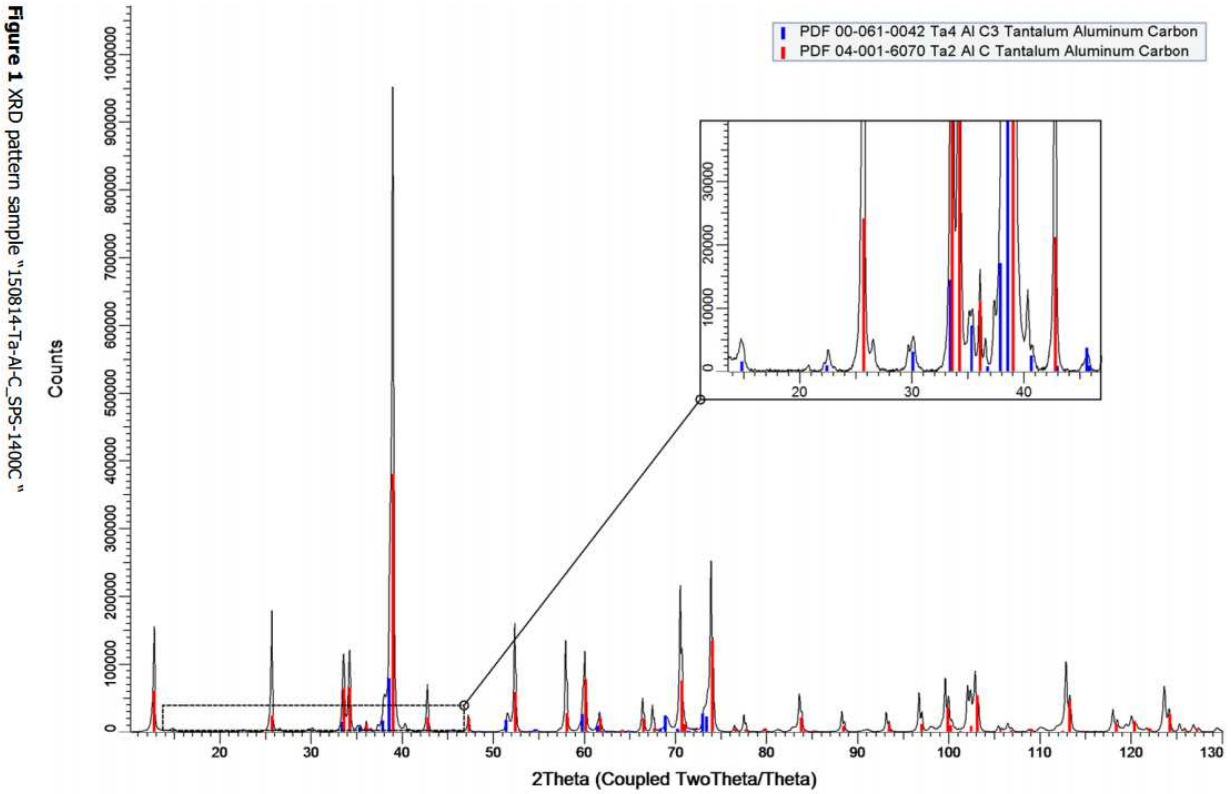

Figure 57: XRD pattern and fit for mainly Ta_2AlC SPS sample 150814-II.

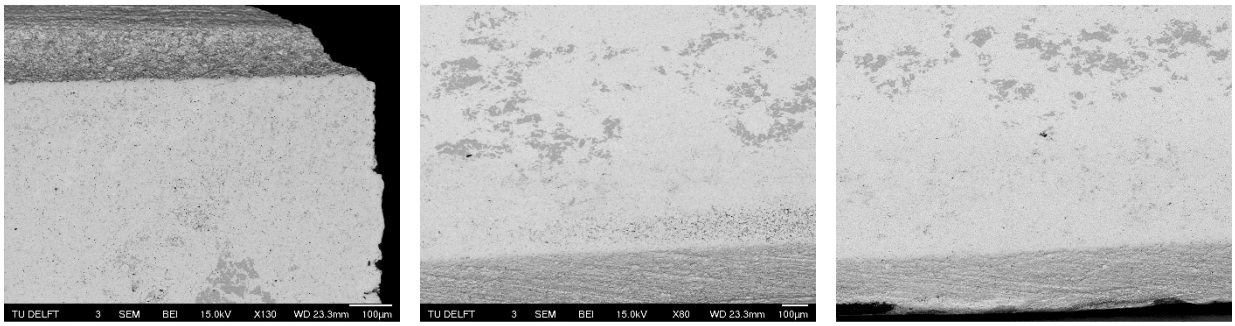

Figure 58: SEM backscatter images of the microstructure of mixed SPS sample 150814-II, viewing a cross-section at relatively large magnification to show the distribution of Al_3Ta impurities (dark grey spots).

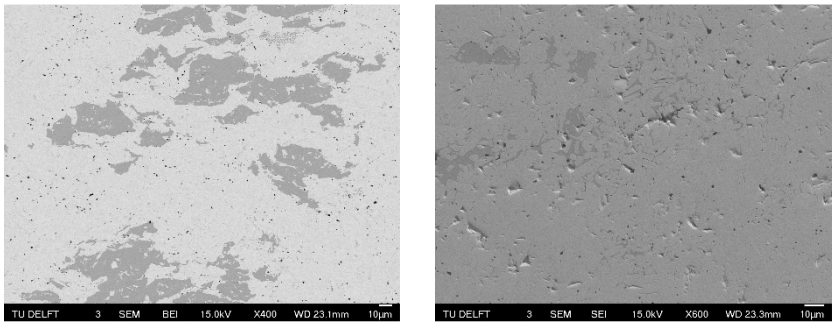

Figure 59: SEM backscatter and secondary image of the microstructure of mixed SPS sample 150814-II, viewing a cross-section to show areas of Al_3Ta impurities (dark grey spots).

Samples 150821 I & II – Ta_2AlC (minor Al_3Ta impurities)

sample	*compound*	
150821-Ta-Al-C_SPS-1400C	Tantalum Aluminum Carbon Tantalum Aluminum Carbon	Ta2 Al C Ta4 Al C3
150821-II-Ta-Al-C_SPS-1400C	Tantalum Aluminum Carbon Tantalum Aluminum Carbon	Ta2 Al C Ta4 Al C3

Table 1.

150821-I (T_{sinter} = 1400 °C)

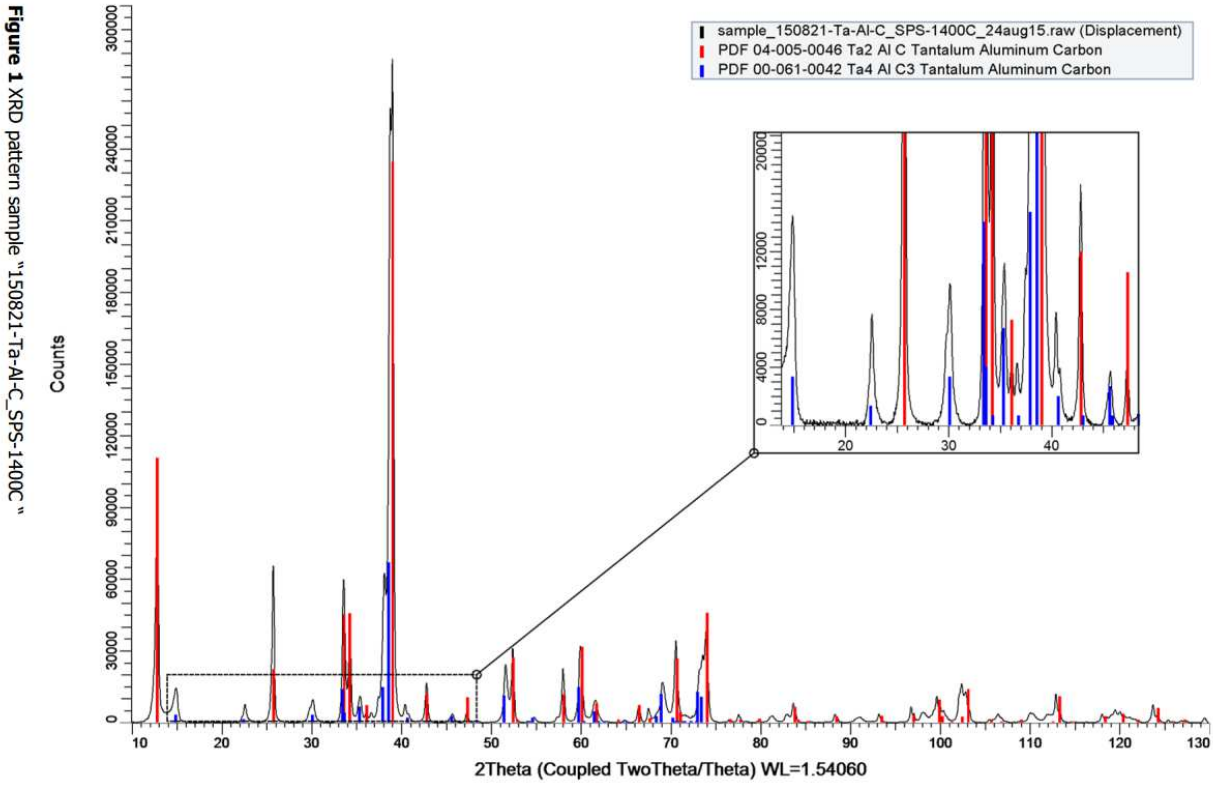

Figure 60: XRD pattern and fit for mainly Ta_2AlC SPS sample 150821-I.

No SEM images made

150821-II (T_{sinter} = 1400 °C)

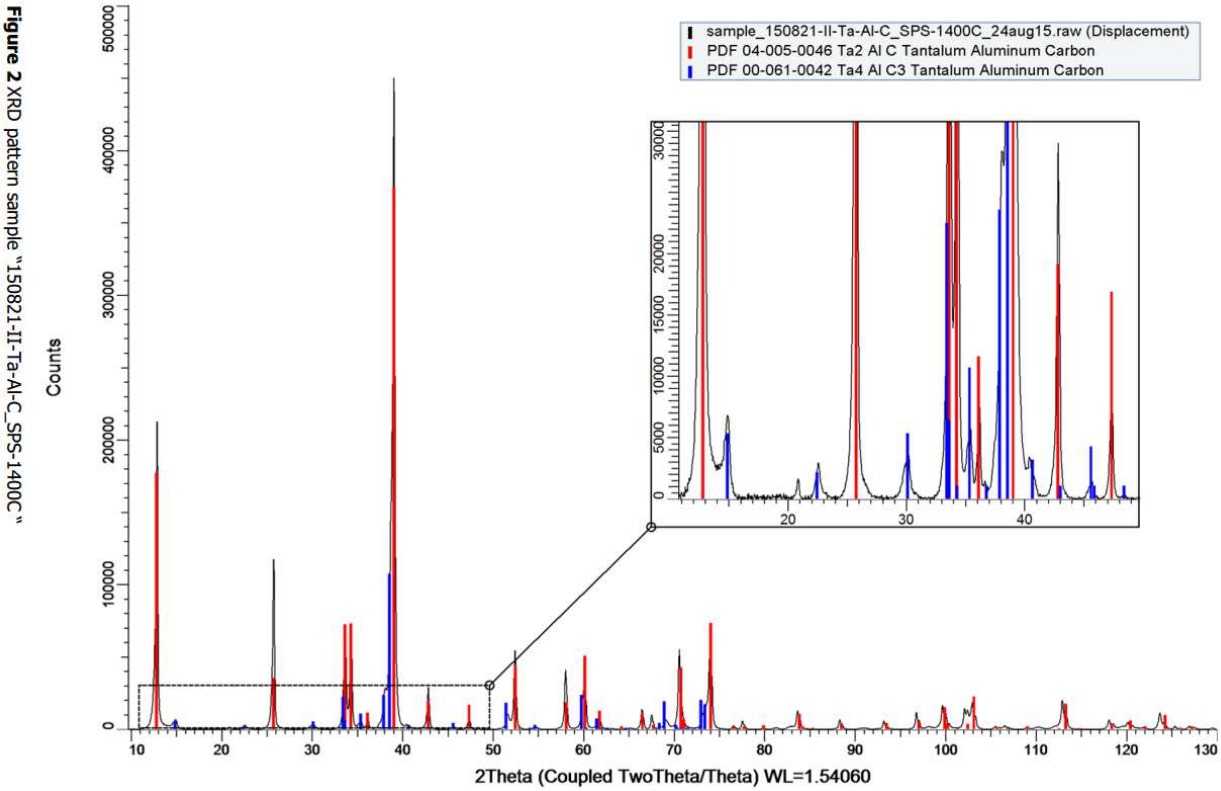

Figure 61: XRD pattern and fit for mainly Ta_2AlC SPS sample 150821-II.

SEM images surface

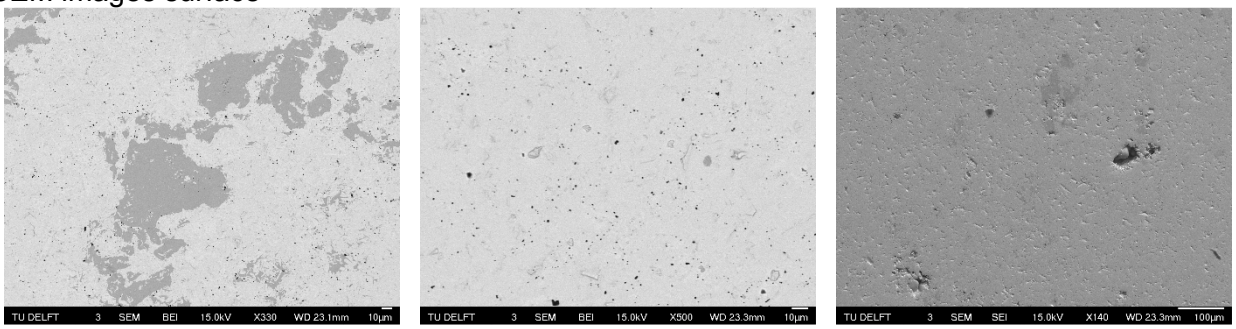

Figure 62: SEM backscatter and secondary (right) images of the microstructure of mainly Ta_2AlC SPS sample 150821-II.

Sample 150824 – Ta_2AlC, minor Ta_4AlC_3

Sample	Phase	Formula
Ta_Al_C_150824	Tantalum Aluminum Carbon	Ta2 Al C
	α-Ta4 Al C3 | Aluminum Tantalum Carbide	Ta4 Al C3

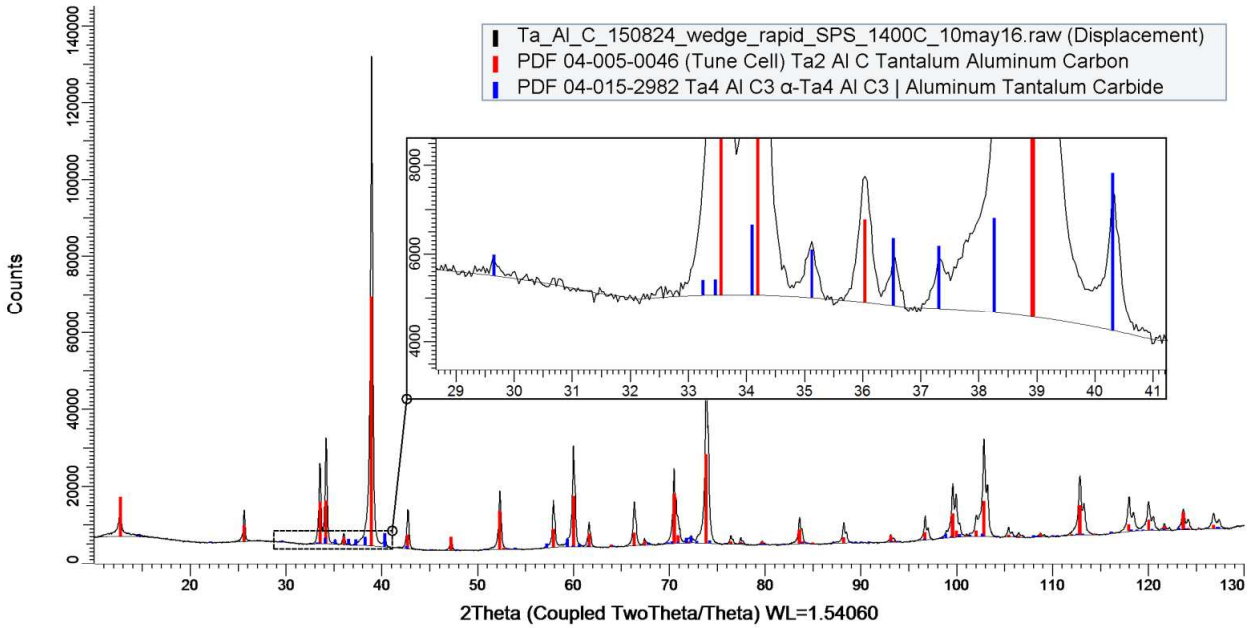

Figure 63: XRD pattern and fit for SPS sample 150824, used as wedge sample (40 mm diameter).

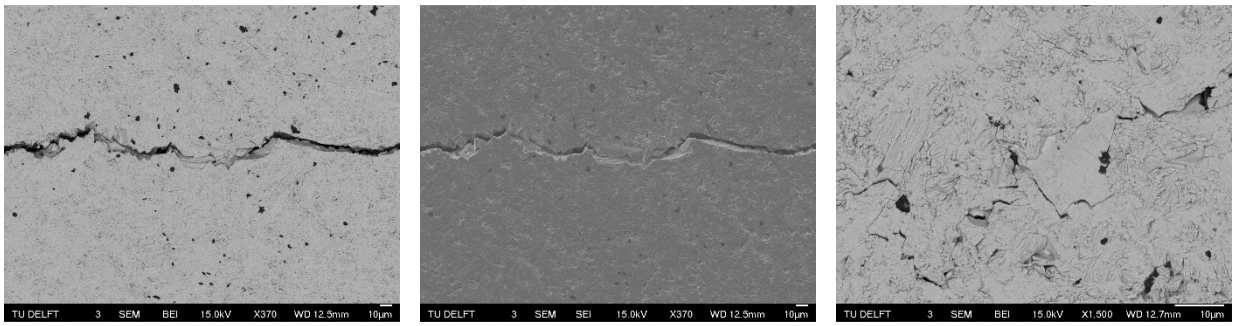

Figure 64: SEM backscatter and secondary (middle) images of the microcrack running along the virgin surface of SPS sample 150824.

Sample 151109 – mixed

sample	*compound*	
Ta-Al-C_151109_rapid-SPS-1400C	Tantalum Aluminum Carbon Tantalum Aluminum Carbon	Ta2 Al C Ta4 Al C3

Table 1.

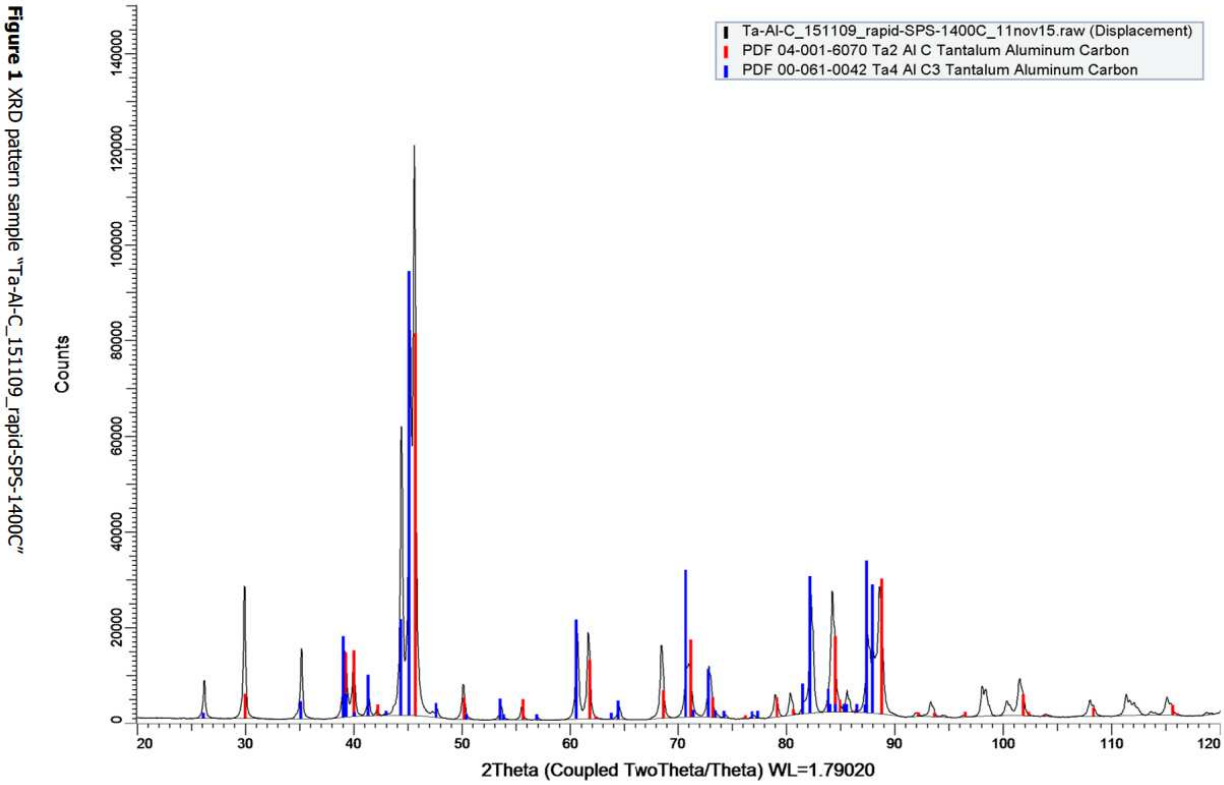

Figure 65: XRD pattern and fit for mixed SPS sample 151109, fabricated for use as wedge sample (40 mm diameter).

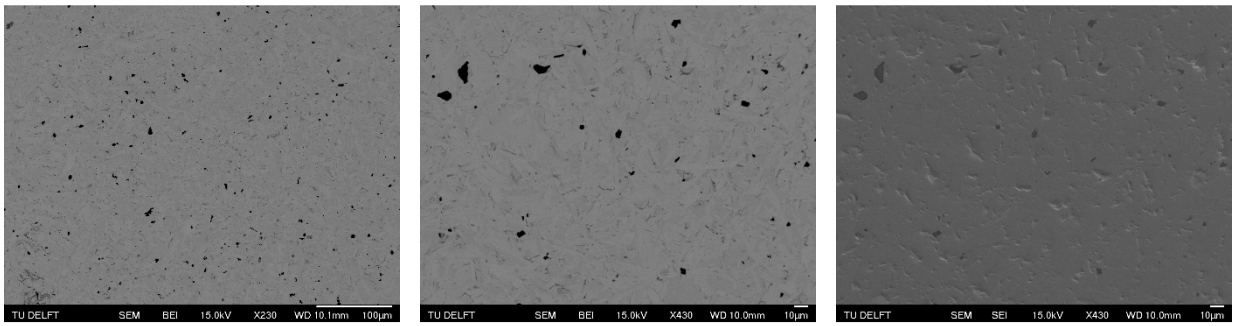

Figure 66: SEM backscatter and secondary (right) images of the microstructure of mixed SPS sample 151109.

Appendix 2 – Qualitative mapping of oxide scale of Ta_2AlC

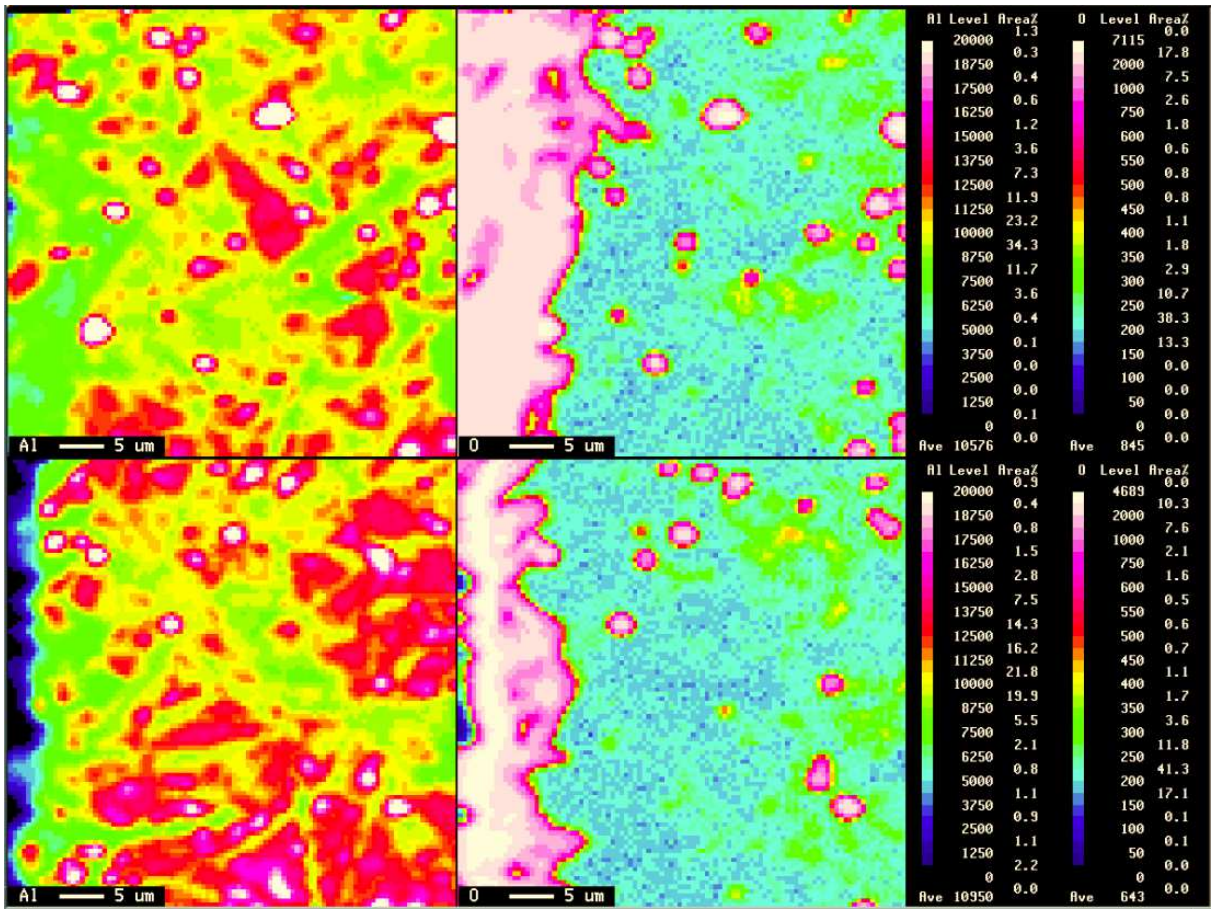

Figure 67: qualitative X-ray mapping of Ta and Al within the oxide scale and underlying bulk Ta_2AlC MAX phase (sample 150814-II) after isothermal oxidation at 600 °C for 10 hours in artificial air. Maps made at 2 different areas on the sample surface.

Appendix 3 – XRD pattern fits for TGA samples after oxidation

An overview is given of the XRD patterns of the TGA samples after isothermal oxidation in artificial air, which have been compared to powder diffraction patterns of different tantalum- and tantalum-aluminium common oxides. Only the results with a relatively good fit for the TGA sample oxidized at 800 °C are shown. For the 800 °C, the oxide was analysed with XRD separately in powder form. The oxide scales on the 600 and 700 °C TGA samples could not be measured separately, and hence show mainly the XRD pattern of the underlying bulk MAX phase sample, as the oxide scale turned out to be too thin to be clearly recognized from the final measured XRD pattern.

Measured XRD patterns of all TGA samples after oxidation (top to bottom: 800, 700, 600 °C TGA sample)

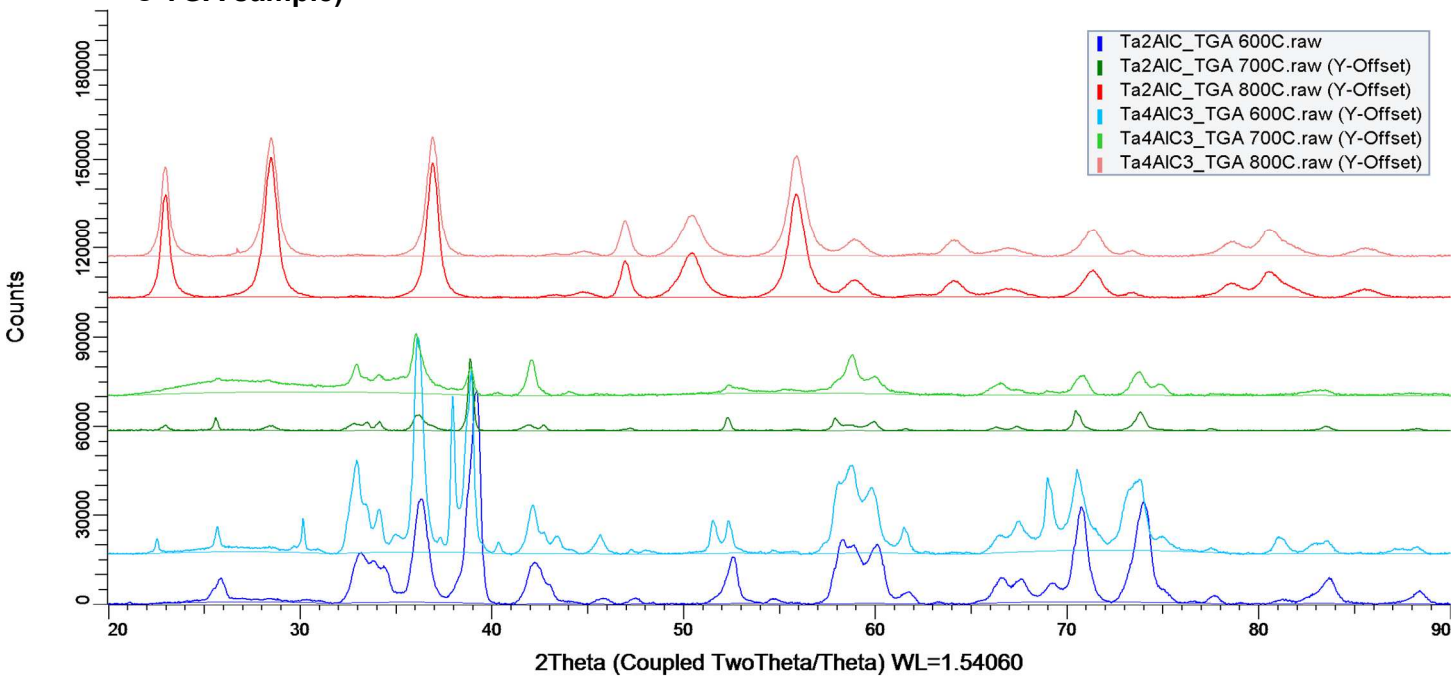

Figure 68: XRD patterns of all TGA samples after oxidation: top to bottom for oxidation at 800, 700, 600 °C, per pair. Top pattern per pair from mixed sample 150604, bottom pattern per pair form Ta_2AlC sample 150814-II.

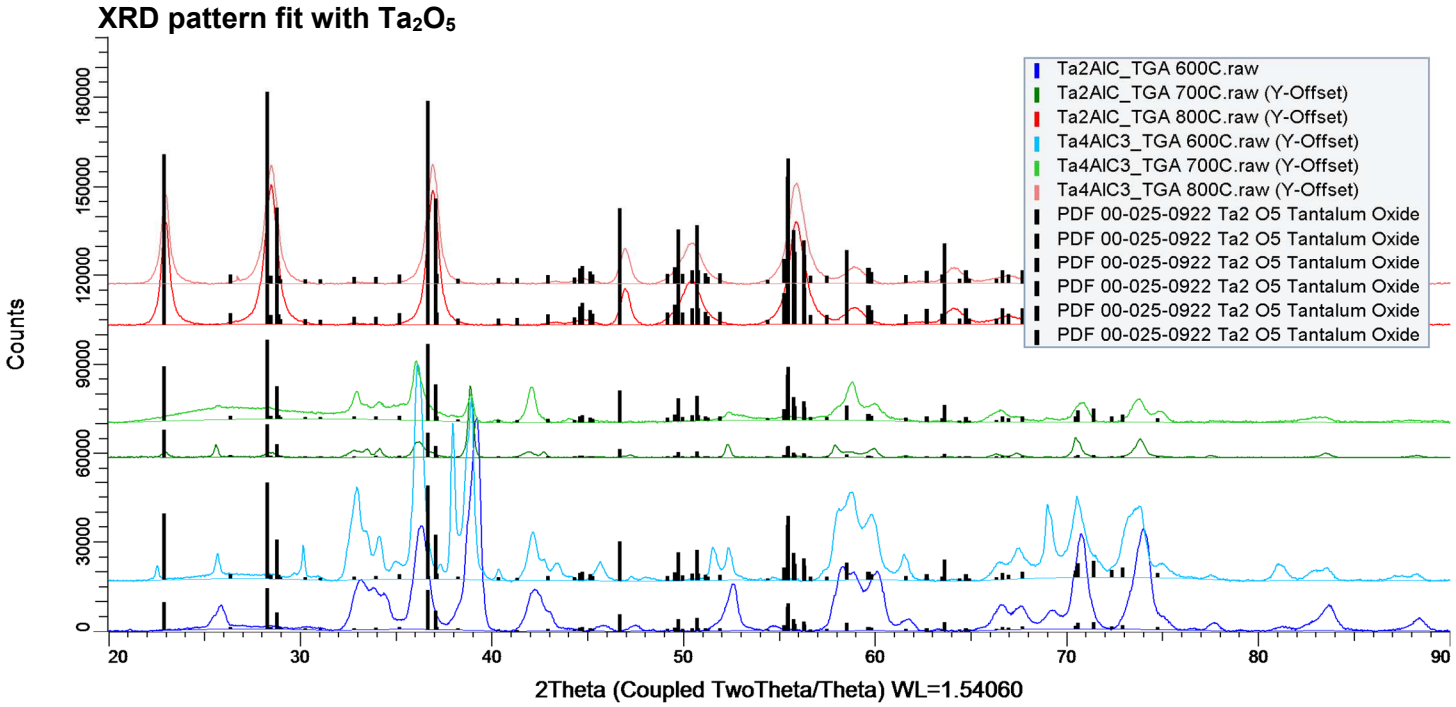

Figure 69: XRD patterns of all TGA samples after oxidation fitted with powder diffraction peaks of Ta_2O_5: top to bottom for oxidation at 800, 700, 600 °C, per pair. Top pattern per pair from mixed sample 150604, bottom pattern per pair form Ta2AlC sample 150814-II.

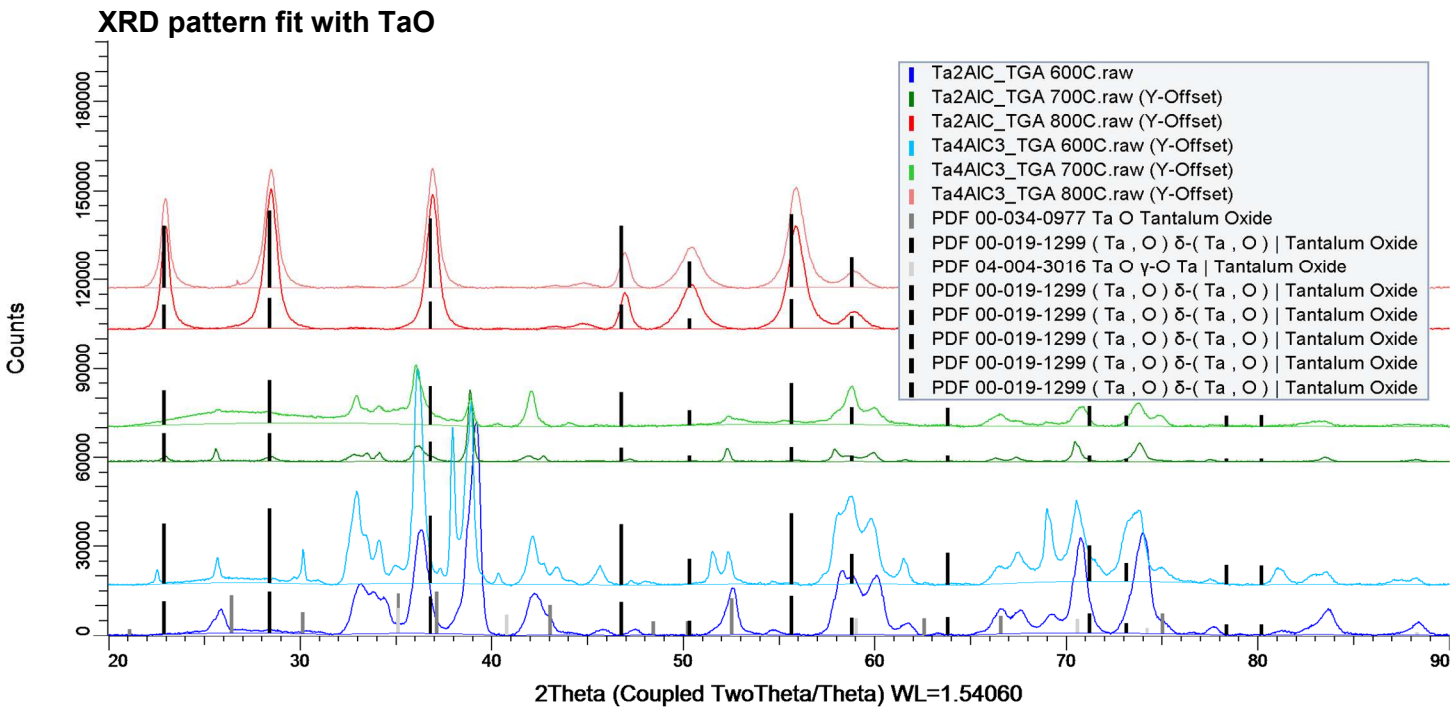

Figure 70: XRD patterns of all TGA samples after oxidation fitted with powder diffraction peaks of TaO: top to bottom for oxidation at 800, 700, 600 °C, per pair. Top pattern per pair from mixed sample 150604, bottom pattern per pair form Ta2AlC sample 150814-II.

Appendix 4 – Measured XPS spectra for oxidized dense bulk Ta_2AlC

Figure 71 shows the complete measured XPS spectrum – binding enerny in eV versus counts per second – for al three dense bulk Ta_2AlC samples isothermally oxidize at 600, 700, and 800 °C respectively. Figure 72 shows a close up of the Ta4f peak for all three spectra. The change of the Ta4f binding energy for different isothermal oxidation temperatures is clearly visible from Figure 72.

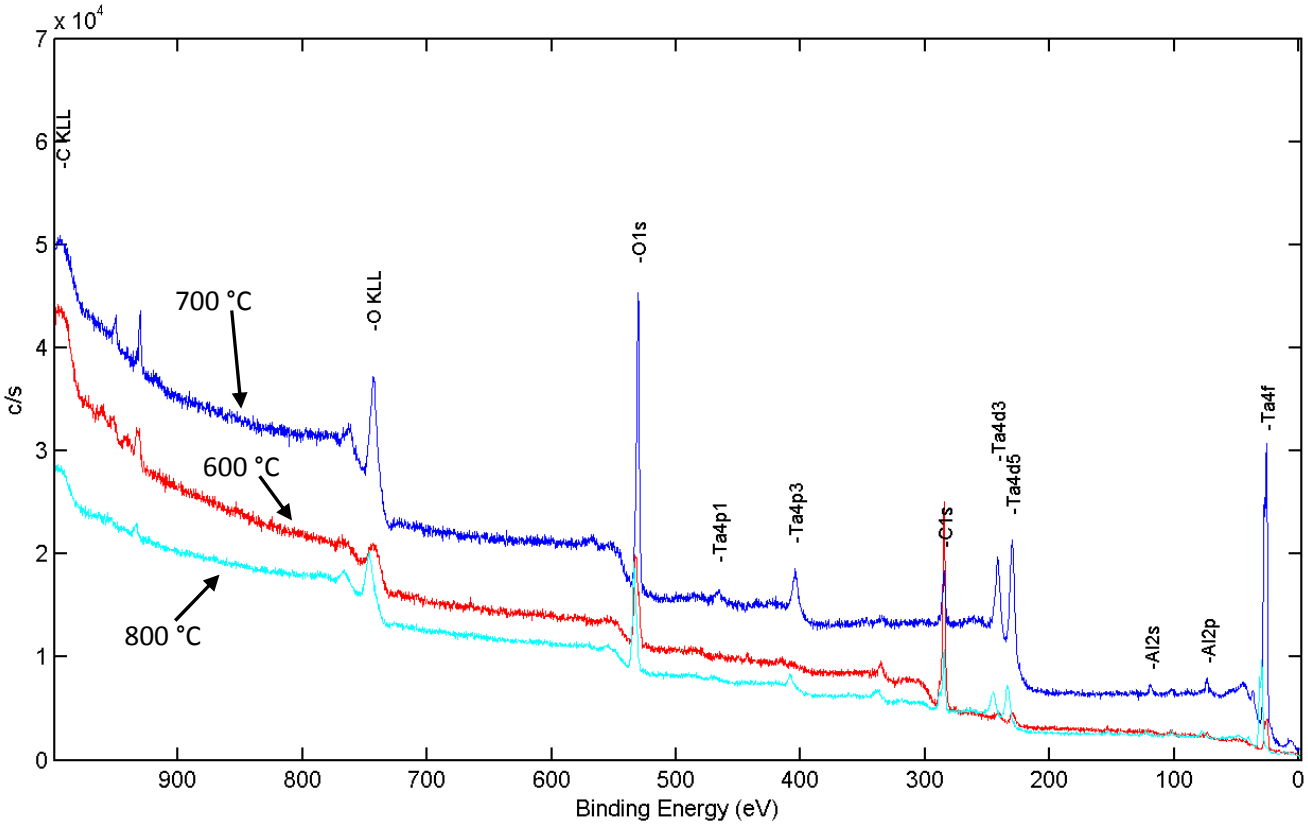

Figure 71: Binding energy (eV) versus counts per second, for measured XPS spectra (Mg Kα X-ray source of 1253.6 eV) of isothermally oxidized dense bulk Ta_2AlC at 600, 700, and 800 °C, respectively shown as red, blue, and turquoise and curve.

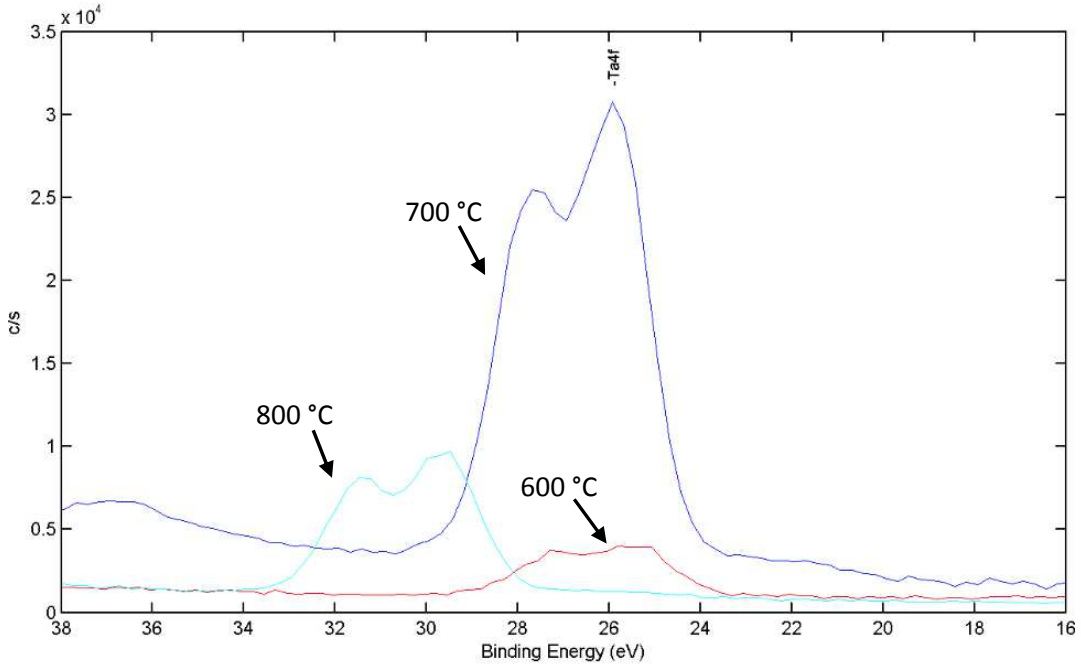

Figure 72: Binding energy (eV) versus counts per second, zoomed in at the two-component Ta4f peak (Mg Kα X-ray source of 1253.6 eV) of isothermally oxidized dense bulk Ta_2AlC at 600, 700, and 800 °C, respectively shown as red, blue, and turquoise and curve.

Appendix 5 – DTA curves of Ta_2AlC and mixed MAX phase powder

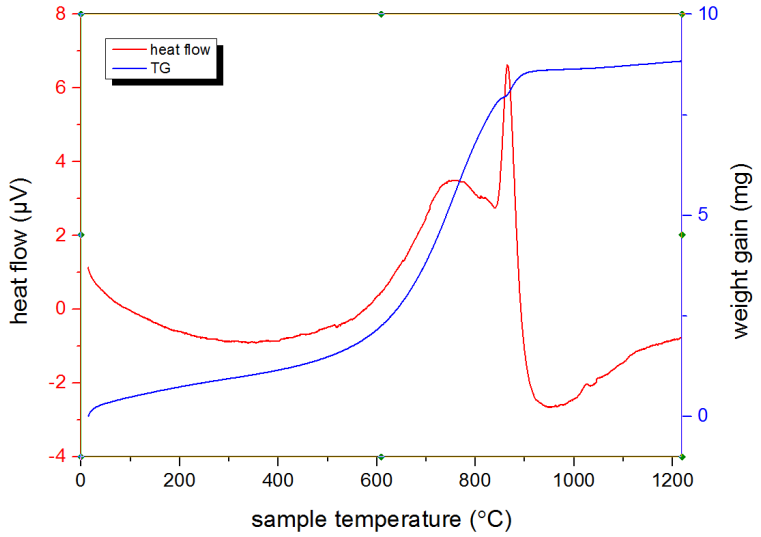

(a) Ta_2AlC

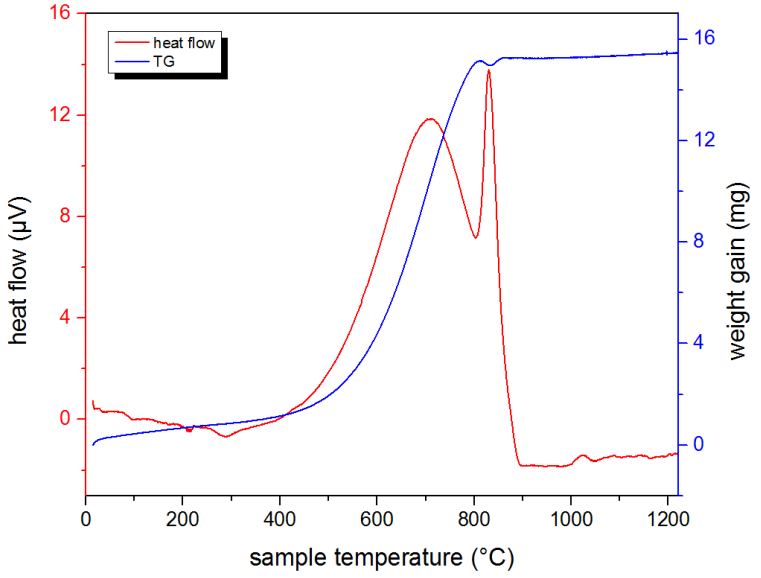

(b) mixed Ta_2AlC and Ta_4AlC_3

Figure 73: DTA curves of a) Ta_2AlC powder (30 mg), and b) mixed powder (60 mg), performed in artificial air with a heating rate of 5 °C/min.

Appendix 6 – DTA curves of Ta and TAC powder incl. CO_2 signal

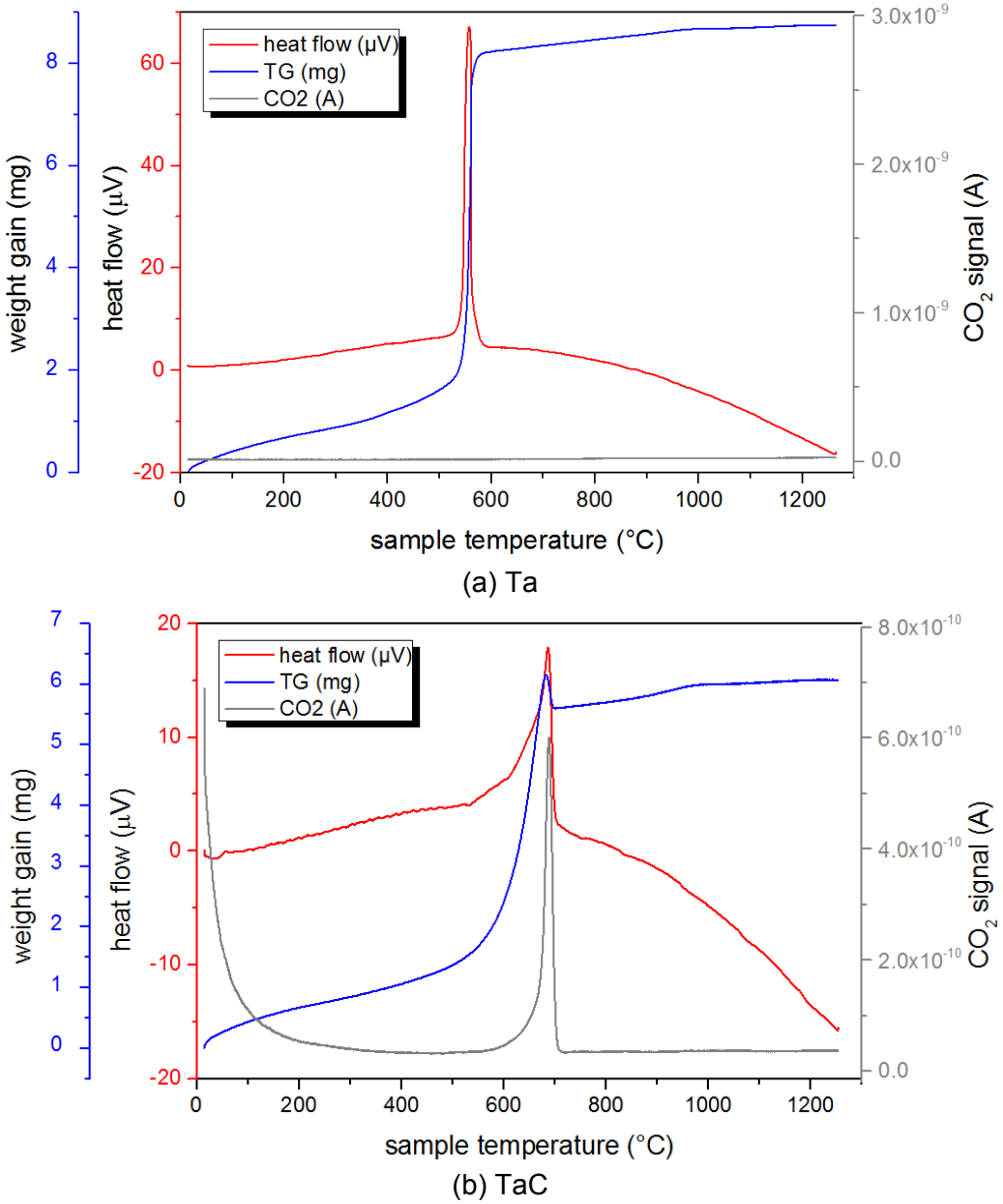

Figure 74: Heat flow and mass gain (TG) curves of 30 mg pure Ta and TaC powder heated from T_{room} until 1200 °C with 2 °C/min, combined with CO_2 signal (obtained with mass spectrometer) a) pure Ta powder, b) pure TaC powder.

Appendix 7 – Kissinger analysis for non-isothermal TaC oxidation, excluding the heating rate of 1 °C/min

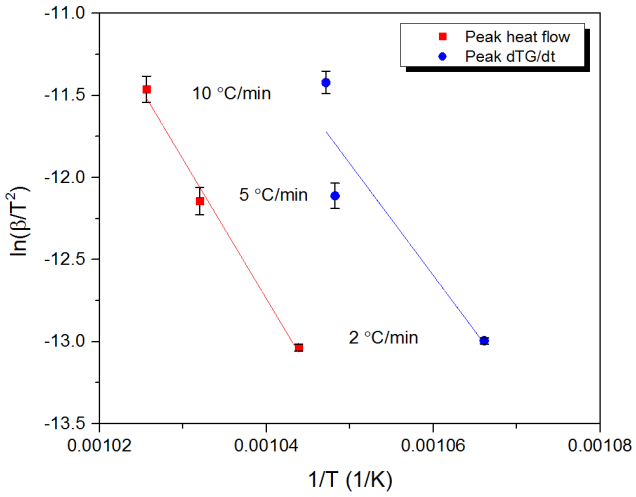

Figure 75: Kissinger points and linear fit from DTA data of TaC powder for the heating rates 2, 5, and 10 °C/min, calculated based on the temperature during heating at which the peak in heat flow and dTG/dt takes place (T_p).

Table 28: Activation energies as calculated from analysis of DTA data of TaC powder with the 95% confidence interval, excluding the Kissinger point corresponding to a heating rate of 1 °C/min

	E_a reaction 1 (kJ/mol)	95% confidence interval (kJ/mol)
TaC - heat flow peak temperature	-707.4	± 131.9
TaC - dTG/dt peak temperature	-566.4	± 471.9

Appendix 8 – Calculation of RVE upon oxidation of Ta-Al-C MAX phase

In section 2.3 the equations to calculate the relative volume expansion upon oxidation of MAX phases are given; for general oxidation, and in the case of selective A-element oxidation. After full conversion by oxidation of Ta-Al-C MAX (achieved by heating of Ta_2AlC DTA powder till 1200 °C), β-Ta_2O_5 and $TaAlO_4$ have been identified by XRD. For oxidation in the temperature range of 600 – 800 °C, various metastable oxides have been identified by XRD analysis, and analysis by EDS and X-ray microanalysis by EPMA show an oxide scale of varying composition and with a Al/Ta ratio that doesn't differ from the bulk MAX phase material. Based on these results, the RVE upon oxidation can be calculated for two extreme cases for Ta_2AlC and Ta_4AlC_3 respectively: 1) full conversion into Ta_2O_5, and 2) conversion into Ta_2O_5 and a maximum amount of $TaAlO_4$. Table 29 shows the corresponding equations to calculate the RVE for each case, and the calculated value of the RVE.

In order to calculate the RVE, the molar volume of all compounds shown in Table 29 has to be known. The molar volume is calculated by dividing the molar mass by the mass density. The result is shown in Table 30.

Table 29: Calculation of RVE upon oxidation of Ta_2AlC and Ta_4AlC_3 for conversion into 1) Ta_2O_5 and 2) into Ta_2O_5 and $TaAlO_4$

	RVE for conversion into Ta_2O_5	RVE for conversion into $TaAlO_4$
Ta_2AlC	$RVE = \frac{V_{Ta_2O_5}}{V_{Ta_2AlC}} \approx 1.54$	$RVE = \frac{V_{Ta_2O_5} + 2V_{AlTaO_4}}{2V_{Ta_2AlC}} = 2.00$
Ta_4AlC_3	$RVE = \frac{2V_{Ta_2O_5}}{V_{Ta_4AlC_3}} \approx 1.76$	$RVE = \frac{3V_{Ta_2O_5} + 2V_{AlTaO_4}}{2V_{Ta_4AlC_3}} = 2.02$

Table 30: overview of molar mass, mass density, and molar volume of relevant compounds for calculation of RVE upon oxidation

Compound	Molar mass M (g/mol)	Mass density ρ (g/cm^3)	Molar volume V_m (cm^3/mol)
Ta_2AlC	400.89	11.52 [26]	34.80
Ta_4AlC_3	786.81	12.92 [81]	60.90
Ta_2O_5	441.90	8.2 [123]	53.63
$TaAlO_4$	271.93	6.36 [124]	42.76

Bibliography

1. Zwaag, S., *Self healing materials: an alternative approach to 20 centuries of materials science*. 2008: Springer Science+ Business Media BV.
2. S. van der Zwaag, E.B., *Self Healing Materials - Pioneering research in the Netherlands*. 2015, Amsterdam: IOS Press.
3. Radovic, M. and M.W. Barsoum, *MAX phases: Bridging the gap between metals and ceramics.* American Ceramic Society Bulletin, 2013. **92**(3): p. 20-27.
4. Barsoum, M.W., *Introduction*, in *MAX Phases*. 2013, Wiley-VCH Verlag GmbH & Co. KGaA. p. 1-12.
5. Barsoum, M.W., *MAX Phases: Properties of Machinable Ternary Carbides and Nitrides*. 2013.
6. Farle, A.-S., et al., *A conceptual study into the potential of Mn+1AXn-phase ceramics for self-healing of crack damage.* Journal of the European Ceramic Society, 2015. **35**(1): p. 37-45.
7. Chen, X.X., et al., *A thermally re-mendable cross-linked polymeric material.* Science, 2002. **295**(5560): p. 1698-1702.
8. Sijbesma, R.P., et al., *Reversible polymers formed from self-complementary monomers using quadruple hydrogen bonding.* Science, 1997. **278**(5343): p. 1601-1604.
9. Jones, F.R., W. Zhang, and S.A. Hayes, *Thermally Induced Self Healing of Thermosetting Resins and Matrices in Smart Composites*, in *Self Healing Materials: An Alternative Approach to 20 Centuries of Materials Science*, S. van der Zwaag, Editor. 2007, Springer Netherlands: Dordrecht. p. 69-93.
10. Zhang, S.S., et al., *Self Healing of Creep Damage by Gold Precipitation in Iron Alloys.* Advanced Engineering Materials, 2015. **17**(5): p. 598-603.
11. S.M. He, S.Z., N.H. van Dijk *Self healing creep steel: copper as healing agent*, in *Self Healing Materials, Pioneering research in the Netherlands*, E.B. S. van der Zwaag, Editor. 2015, IOS Press: Amsterdam.
12. Sloof, W.G., *Self Healing in Coatings at High Temperatures*, in *Self Healing Materials: An Alternative Approach to 20 Centuries of Materials Science*, S. van der Zwaag, Editor. 2007, Springer Netherlands: Dordrecht. p. 309-321.
13. Ando, K., et al., *Crack-healing and mechanical behaviour of Al2O3/SiC composites at elevated temperature.* Fatigue & Fracture of Engineering Materials & Structures, 2004. **27**(7): p. 533-541.
14. W.G. Sloof, A.S.F., L. Shen, *Intrinsic autonomous crack healing in MAX phase ceramics*, in *Self Healing Materials - Pioneering research in the Netherlands*, E.B. S. van der Zwaag, Editor. 2015, IOS Press: Amsterdam.
15. Li, S.B., et al., *Multiple crack healing of a Ti2AlC ceramic.* Journal of the European Ceramic Society, 2012. **32**(8): p. 1813-1820.
16. Yang, H.J., Y.T. Pei, and J.T.M. De Hosson, *Oxide-scale growth on Cr2AlC ceramic and its consequence for self-healing.* Scripta Materialia, 2013. **69**(2): p. 203-206.
17. Eklund, P., et al., *The Mn + 1AXn phases? [Elektronisk resurs] : Materials science and thin-film processing*. 2010, Thin Solid Films.
18. Lane, N.J., et al., *Structure of a new bulk Ti5Al2C3 MAX phase produced by the topotactic transformation of Ti2AlC.* Journal of the European Ceramic Society, 2012. **32**(12): p. 3485-3491.
19. Barsoum, M.W. and T. El-Raghy, *The MAX phases: Unique new carbide and nitride materials.* American Scientist, 2001. **89**(4): p. 334.
20. Medvedeva, N.I., et al., *Electronic properties of Ti3SiC2-based solid solutions.* Physical Review B, 1998. **58**(24): p. 16042-16050.
21. Hug, G. and E. Fries, *Full-potential electronic structure of Ti2AlC and Ti2AlN.* Physical Review B, 2002. **65**(11).
22. Hug, G., M. Jaouen, and M.W. Barsoum, *X-ray absorption spectroscopy, EELS, and full-potential augmented plane wave study of the electronic structure of Ti2AlC, Ti2AlN, Nb2AlC, and (Ti0.5Nb0.5)(2)AlC.* Physical Review B, 2005. **71**(2).
23. Holm, B., R. Ahuja, and B. Johansson, *Ab initio calculations of the mechanical properties of Ti3SiC2.* Applied Physics Letters, 2001. **79**(10): p. 1450-1452.

24. Sun, Z.M., et al., *Structure and bulk modulus of M2AlC (M=Ti, V, and Cr).* Applied Physics Letters, 2003. **83**(5): p. 899-901.
25. Palmquist, J.P., et al., *M(n+1)AX(n) phases in the Ti-Si-C system studied by thin-film synthesis and ab initio calculations.* Physical Review B, 2004. **70**(16).
26. Sun, Z.M., et al., *Calculated elastic properties of M2AlC (M = Ti, V, Cr, Nb and Ta).* Solid State Communications, 2004. **129**(9): p. 589-592.
27. Dahlqvist, M., B. Alling, and J. Rosen, *Stability trends of MAX phases from first principles.* Physical Review B, 2010. **81**(22).
28. Barsoum, M.W., *Electronic, Optical, and Magnetic Properties*, in *MAX Phases*. 2013, Wiley-VCH Verlag GmbH & Co. KGaA. p. 155-185.
29. Barsoum, M.W., *Thermal Properties*, in *MAX Phases*. 2013, Wiley-VCH Verlag GmbH & Co. KGaA. p. 107-153.
30. Barsoum, M.W. and M. Radovic, *Elastic and mechanical properties of the MAX phases.* Annual review of materials research, 2011. **41**: p. 195-227.
31. Sun, Z., *Progress in research and development on MAX phases: a family of layered ternary compounds.* International Materials Reviews, 2011. **56**(3): p. 143-166.
32. Barsoum, M.W., *Mechanical Properties: Ambient Temperature*, in *MAX Phases*. 2013, Wiley-VCH Verlag GmbH & Co. KGaA. p. 307-361.
33. Barsoum, M.W., *Mechanical Properties: High Temperatures*, in *MAX Phases*. 2013, Wiley-VCH Verlag GmbH & Co. KGaA. p. 363-397.
34. Song, G.M., et al., *Oxidation-induced crack healing in Ti3AlC2 ceramics.* Scripta Materialia, 2008. **58**(1): p. 13-16.
35. Wang, X.H., et al., *Insights into high temperature oxidation of Al2O3-forming Ti3AlC2.* Corrosion Science, 2012. **58**: p. 95-103.
36. Song, G.M., et al., *Early stages of oxidation of Ti3AlC2 ceramics.* Materials Chemistry and Physics, 2008. **112**(3): p. 762-768.
37. Li, S.B., et al., *Oxidation and Crack Healing Behavior of a Fine-Grained Cr2AlC Ceramic.* Journal of the American Ceramic Society, 2013. **96**(3): p. 892-899.
38. Zhou, A., *2 - Methods of MAX-phase synthesis and densification – II A2 - Low, I.M*, in *Advances in Science and Technology of Mn+1axn Phases*. 2012, Woodhead Publishing. p. 21-46.
39. Qian, X.K., *1 - Methods of MAX-phase synthesis and densification – I A2 - Low, I.M*, in *Advances in Science and Technology of Mn+1axn Phases*. 2012, Woodhead Publishing. p. 1-19.
40. Pietzka, M.A. and J.C. Schuster, *Summary of constitutional data on the Aluminum-Carbon-Titanium system.* Journal of Phase Equilibria, 1994. **15**(4): p. 392-400.
41. Peng, C., et al., *A novel simple method to stably synthesize Ti3AlC2 powder with high purity.* Materials Science and Engineering: A, 2006. **428**(1–2): p. 54-58.
42. Sun, Z., S. Yang, and H. Hashimoto, *Ti3SiC2 powder synthesis.* Ceramics International, 2004. **30**(7): p. 1873-1877.
43. Li, H., et al., *Synthesis of Ti3SiC2 by pressureless sintering of the elemental powders in vacuum.* Materials Letters, 2004. **58**(11): p. 1741-1744.
44. Li, J.F., T. Matsuki, and R. Watanabe, *Mechanical-alloying-assisted synthesis of Ti3SiC2 powder.* Journal of the American Ceramic Society, 2002. **85**(4): p. 1004-1006.
45. Jin, S., et al., *Effect of Al addition on phase purity of Ti3Si(Al)C2 synthesized by mechanical alloying.* Journal of Materials Processing Tech., 2007. **182**(1-3): p. 445-449.
46. Ai, M.X., et al., *Synthesis of Ti3AlC2 powders using Sn as an additive.* Journal of the American Ceramic Society, 2006. **89**(3): p. 1114-1117.
47. Li, J.-F., T. Matsuki, and R. Watanabe, *Fabrication of highly dense Ti3SiC2 ceramics by pressureless sintering of mechanically alloyed elemental powders.* Journal of Materials Science, 2003. **38**(12): p. 2661-2666.
48. Lopacinski, M., J. Puszynski, and J. Lis, *Synthesis of ternary titanium aluminum carbides using self-propagating high-temperature synthesis technique.* Journal of the American Ceramic Society, 2001. **84**(12): p. 3051-3053.
49. Zhou, A., et al., *Preparation of Ti3AlC2 and Ti2AlC by self-propagating high-temperature synthesis.* Journal of Materials Science Letters, 2001. **20**(21): p. 1971-1973.
50. Liang, B., et al., *Synthesis of Ti2AlC by laser-induced self-propagating high-temperature sintering.* Journal of Alloys and Compounds, 2010. **501**(1): p. L1-L3.

51. Guo, J.M., et al., *Effects of carbon addition on combustion synthesis of Ti3AlC2 powders.* Acta Metallurgica Sinica, 2003. **39**(4): p. 409-413.
52. Ge, Z.B., et al., *Formation mechanism of ternary carbide Ti3AlC2 by combustion synthesis.* Journal of Inorganic Materials, 2003. **18**(2): p. 427-432.
53. Lis, J., et al., *TI3SIC-BASED MATERIALS PREPARED BY HIP-SHS TECHNIQUES.* Materials Letters, 1995. **22**(3-4): p. 163-168.
54. Yeh, C.L. and Y.G. Shen, *Effects of TiC addition on formation of Ti3SiC2 by self-propagating high-temperature synthesis.* Journal of Alloys and Compounds, 2008. **458**(1–2): p. 286-291.
55. Pampuch, R., et al., *Solid combustion synthesis of Ti3SiC2.* Journal of the European Ceramic Society, 1989. **5**(5): p. 283-287.
56. Gauthier, V., et al., *Self-propagating high-temperature synthesis of Ti3SiC2: Study of the reaction mechanisms by time-resolved X-ray diffraction and infrared thermography.* Journal of the American Ceramic Society, 2006. **89**(9): p. 2899-2907.
57. Riley, D.P., E.H. Kisi, and T.C. Hansen, *Self-Propagating High-Temperature Synthesis of Ti3SiC2: II. Kinetics of Ultra-High-Speed Reactions from In Situ Neutron Diffraction.* Journal of the American Ceramic Society, 2008. **91**(10): p. 3207-3210.
58. Huang, T.Y. and C.C. Chen, *Ternary ceramics Ti3SiC2: combustion synthesis and the reaction mechanism*, in *Pricm 5: The Fifth Pacific Rim International Conference on Advanced Materials and Processing, Pts 1-5*, Z.Y. Zhong, et al., Editors. 2005, Trans Tech Publications Ltd: Zurich-Uetikon. p. 1609-1614.
59. Barsoum, M.W. and T. ElRaghy, *Synthesis and characterization of a remarkable ceramic: Ti3SiC2.* Journal of the American Ceramic Society, 1996. **79**(7): p. 1953-1956.
60. El-Raghy, T., et al., *Processing and mechanical properties of Ti3SiC2: II, effect of grain size and deformation temperature.* Journal of the American Ceramic Society, 1999. **82**(10): p. 2855-2860.
61. Li, J.-F., F. Sato, and R. Watanabe, *Synthesis of Ti3SiC2 polycrystals by hot-isostatic pressing of the elemental powders.* Journal of Materials Science Letters, 1999. **18**(19): p. 1595-1597.
62. Ertuğ, M.O., et al. *2.CERAMIC MATRIX COMPOSITE MATERIALS*. 2014 [cited 2015 14 Jan]; Available from: http://kansu.tripod.com/me451/2.html.
63. Jiaoqun, Z. and M. Bingchu, *Effect of Aluminum on Synthesis of Ti3SiC2 by Spark Plasma Sintering (SPS) from Elemental Powders.* Journal of Materials Synthesis and Processing, 2002. **10**(6): p. 353-358.
64. Khoptiar, Y., I. Gotman, and E.Y. Gutmanas, *Pressure-assisted combustion synthesis of dense layered Ti3AlC2 and its mechanical properties.* Journal of the American Ceramic Society, 2005. **88**(1): p. 28-33.
65. Bai, Y.L., et al., *Rapid synthesis of bulk Ti2AlC by self-propagating high temperature combustion synthesis with a pseudo-hot isostatic pressing process.* Journal of Materials Research, 2009. **24**(8): p. 2528-2535.
66. Hu, C., et al., *Microstructure and properties of bulk Ta2AlC ceramic synthesized by an in situ reaction/hot pressing method.* Journal of the European Ceramic Society, 2008. **28**(8): p. 1679-1685.
67. Xiang, H., et al., *Prediction of superconductivity of Ta2AlC: in situ Raman spectrometry and density functional investigations.* Journal of Raman Spectroscopy, 2014. **45**(2): p. 202-207.
68. Yeh, C.L. and Y.G. Shen, *Effects of Al content on formation of Ta2AlC by self-propagating high-temperature synthesis.* Journal of Alloys and Compounds, 2009. **482**(1–2): p. 219-223.
69. Lin, Z., et al., *Microstructures and Theoretical Bulk Modulus of Layered Ternary Tantalum Aluminum Carbides.* Journal of the American Ceramic Society, 2006. **89**(12): p. 3765-3769.
70. Qian, X., et al., *First-principle study of structural and electronic properties of ternary layered Ta2AlC.* Journal of Physics and Chemistry of Solids, 2011. **72**(8): p. 954-956.
71. Lane, N.J., et al., *First-order Raman scattering of the MAX phases Ta4AlC3, Nb4AlC3, Ti4AlN3, and Ta2AlC.* Journal of Raman Spectroscopy, 2012. **43**(7): p. 954-958.
72. Gupta, S., et al., *Ta2AlC and Cr2AlC Ag-based composites—New solid lubricant materials for use over a wide temperature range against Ni-based superalloys and alumina.* Wear, 2007. **262**(11–12): p. 1479-1489.
73. Leaffer, O.D., et al., *On Raman scattering from selected M2AC compounds.* Journal of Materials Research, 2007. **22**(10): p. 2651-2654.

74. Drulis, M.K., et al., *On the heat capacities of Ta2AlC, Ti2SC, and Cr2GeC.* Journal of Applied Physics, 2008. **104**(2): p. -.
75. Gupta, S., et al., *Tribological behavior of select MAX phases against Al2O3 at elevated temperatures.* Wear, 2008. **265**(3-4): p. 560-565.
76. Hoffman, E.N., et al., *Micro and mesoporosity of carbon derived from ternary and binary metal carbides.* Microporous and Mesoporous Materials, 2008. **112**(1–3): p. 526-532.
77. Sun, W., W. Luo, and R. Ahuja, *Role of correlation and relativistic effects in MAX phases.* Journal of Materials Science, 2012. **47**(21): p. 7615-7620.
78. Yeh, C.L. and E.W. Liu, *Combustion synthesis of tantalum carbides TaC and Ta2C.* Journal of Alloys and Compounds, 2006. **415**(1-2): p. 66-72.
79. 3-ONE-2. *3-ONE-2 Home*. 2006 [cited 2015 15 Jan]; Available from: http://www.3one2.com/main.html.
80. Lin, Z.J., et al., *Microstructures and theoretical bulk modulus of layered ternary tantalum aluminum carbides.* Journal of the American Ceramic Society, 2006. **89**(12): p. 3765-3769.
81. Etzkorn, J., M. Ade, and H. Hillebrecht, *Ta3AlC2 and Ta4AlC3 − Single-Crystal Investigations of Two New Ternary Carbides of Tantalum Synthesized by the Molten Metal Technique.* Inorganic Chemistry, 2007. **46**(4): p. 1410-1418.
82. Ramzan, M., S. Lebègue, and R. Ahuja, *Hybrid exchange-correlation functional study of the structural, electronic, and mechanical properties of the MAX phases.* Applied Physics Letters, 2011. **98**(2): p. -.
83. Hu, C., et al., *Physical and mechanical properties of bulk Ta4AlC3 ceramic prepared by an in situ reaction synthesis/hot-pressing method.* Journal of the American Ceramic Society, 2007. **90**(8): p. 2542-2548.
84. Gupta, S., D. Filimonov, and M.W. Barsoum, *Isothermal Oxidation of Ta2AlC in Air.* Journal of the American Ceramic Society, 2006. **89**(9): p. 2974-2976.
85. Garg, S.P., et al., *The O-Ta (Oxygen-Tantalum) system.* Journal of Phase Equilibria, 1996. **17**(1): p. 63-77.
86. Norman, N., P. Kofstad, and O.J. Krudtaa, *Metallic oxide phases of niobium and tantalum II. Metallographic studies.* Journal of the Less Common Metals, 1962. **4**(2): p. 124-137.
87. Kofstad, P. and O.J. Krudtaa, *High temperature metallographic microscope studies of the initial oxidation of tantalum.* Journal of the Less Common Metals, 1963. **5**(6): p. 477-492.
88. Kofstad, P., *The Oxidation Behavior of Tantalum at 700°–1000°C.* Journal of The Electrochemical Society, 1963. **110**(6): p. 491-501.
89. Kofstad, P., *Studies of the oxidation of tantalum at 1000°–1300° C.* Journal of the Less Common Metals, 1963. **5**(2): p. 158-170.
90. Stringer, J., *Void formation during the oxidation of tantalum.* Journal of the Less Common Metals, 1966. **11**(2): p. 111-118.
91. Voitovich, V.B., et al., *High-temperature oxidation of tantalum of different purity.* Oxidation of Metals. **43**(5): p. 509-526.
92. Haycock, E.W., *Transitions from Parabolic to Linear Kinetics in Scaling of Metals.* Journal of The Electrochemical Society, 1959. **106**(9): p. 771-775.
93. Pawel, R.E., J.V. Cathcart, and J.J. Campbell, *Stress Generation in Tantalum During Oxidation.* Journal of The Electrochemical Society, 1963. **110**(6): p. 551-557.
94. DesmaisonBrut, M., N. Alexandre, and J. Desmaison, *Comparison of the oxidation behaviour of two dense hot isostatically pressed tantalum carbide (TaC and Ta2C) materials.* Journal of the European Ceramic Society, 1997. **17**(11): p. 1325-1334.
95. Guillon, O., et al., *Field-Assisted Sintering Technology/Spark Plasma Sintering: Mechanisms, Materials, and Technology Developments.* Advanced Engineering Materials, 2014. **16**(7): p. 830-849.
96. University, T.O. *PHYS 7.1: The atomic basis of matter*. 1996 [cited 2016; Available from: http://www.met.reading.ac.uk/pplato2/h-flap/phys7_1.html.
97. Nanoscience. *Sample-Electron Interaction*. 2016 [cited 2016; Available from: http://www.nanoscience.com/technology/sem-technology/sample-electron-interaction/.
98. International, A., *Standard Test Method for Microindentation Hardness of Materials*. 2016, ASTM International.

99. Institute, T.W. *Hardness Testing Part 1*. 2016 [cited 2016; Available from: http://www.twi-global.com/technical-knowledge/job-knowledge/hardness-testing-part-1-074/.
100. Kissinger, H.E., *VARIATION OF PEAK TEMPERATURE WITH HEATING RATE IN DIFFERENTIAL THERMAL ANALYSIS.* Journal of Research of the National Bureau of Standards, 1956. **57**(4): p. 217-221.
101. Instruments, M. *Mastersizer 3000*. 2016 [cited 2016; Available from: http://www.malvern.com/en/products/product-range/mastersizer-range/mastersizer-3000/default.aspx?gclid=CIHb39r5sc0CFVIYGwodOWwDFA.
102. Wendlandt, W.W., *Thermal methods of analysis*. 1974, New York: Wiley-Interscience.
103. Anasori, B., et al., *On the oxidation of Ti2GeC in air.* Journal of Alloys and Compounds, 2013. **580**: p. 550-557.
104. Basu, S., et al., *Long-Term Oxidation of Ti2AlC in Air and Water Vapor at 1000-1300 degrees C Temperature Range (vol 159, pg C90, 2012).* Journal of the Electrochemical Society, 2012. **159**(5): p. S9-S9.
105. Xu, C. and W. Gao, *Pilling-Bedworth ratio for oxidation of alloys.* Material Research Innovations, 2000. **3**(4): p. 231-235.
106. Farle, A.M.e.a., *Method to determine fracture toughness and strength with a controlled crack path of semi-brittle metallo-ceramics.* Engineering Fracture Mechanics, 2016 to be published.
107. Clark, B.M., et al., *Spark Plasma Sintering of Neodymium Titanate Pyrochlore for Advanced Ceramic Waste Forms*, in *Advances in Materials Science for Environmental and Energy Technologies III*. 2014, John Wiley & Sons, Inc. p. 127-135.
108. Duan, X., et al., *Synthesis of high-purity, isotropic or textured Cr2AlC bulk ceramics by spark plasma sintering of pressure-less sintered powders.* Journal of the European Ceramic Society, 2015. **35**(5): p. 1393-1400.
109. Sun, Z., et al., *Synthesis of the MAX Phases by Pulse Discharge Sintering.* International Journal of Applied Ceramic Technology, 2010. **7**(6): p. 704-718.
110. Ghosh, N.C. and S.P. Harimkar, *3 - Consolidation and synthesis of MAX phases by Spark Plasma Sintering (SPS): a review*, in *Advances in Science and Technology of Mn+1axn Phases*, I.M. Low, Editor. 2012, Woodhead Publishing. p. 47-80.
111. Anderson Materials Evaluation, I. *SEM Illustrative Example: Secondary Electron and Backscatter Electron Images*. 2016 [cited 2016 10 May]; Available from: http://www.andersonmaterials.com/sem/sem-secondary-backscatter-images.html#.
112. F. Izumi, H.K., *A new modification of tantalum(V) oxide.* J. Less-Common Met. , 1979. **63**(2): p. 305-307.
113. Low, P.I.M., *Thermal Decomposition of MAX Phases*, A. Materials, Editor. 2013, AZoM.com.
114. Okamoto, H., *Al-Ta (Aluminum-Tantalum).* Journal of Phase Equilibria and Diffusion, 2010. **31**(6): p. 578-579.
115. Sina, H., S. Iyengar, and S. Lidin, *Reaction behavior and evolution of phases during the sintering of Ta–Al powder mixtures.* Journal of Alloys and Compounds, 2016. **654**: p. 103-111.
116. Condron, C.L., et al., *A new look at bonding in trialuminides: Reinvestigation of TaAl3.* Inorganic Chemistry, 2003. **42**(25): p. 8371-8376.
117. Huizenga, R., *Minimum layer thickness to be measured with XRD for dense bulk Ta-Al-C MAX phase samples after isothermal oxidation, as discussed in personal e-mail communication*. 2016.
118. Moulder, J.F. and J. Chastain, *Handbook of X-ray Photoelectron Spectroscopy: A Reference Book of Standard Spectra for Identification and Interpretation of XPS Data*. 1992: Physical Electronics Division, Perkin-Elmer Corporation.
119. Anzel, I., *High temperature oxidation of metals and alloys.* METALURGIJA - JOURNAL OF METALLURGY, 2000: p. 325-336.
120. Purdue, U., C. Thermophysical Properties Research, and Y.S. Touloukian, *Thermophysical properties of matter; [the TPRC data series; a comprehensive compilation of data*. 1970, New York: IFI/Plenum.
121. Graham, D.W. and D.P. Stinton, *DEVELOPMENT OF TANTALUM PENTOXIDE COATINGS BY CHEMICAL-VAPOR-DEPOSITION.* Journal of the American Ceramic Society, 1994. **77**(9): p. 2298-2304.
122. Kissinger, H.E., *Reaction Kinetics in Differential Thermal Analysis.* Analytical Chemistry, 1957. **29**(11): p. 1702-1706.

123. Aleshina, L.A. and S.V. Loginova, *Rietveld analysis of X-ray diffraction pattern from β-Ta2O5 oxide.* Crystallography Reports, 2002. **47**(3): p. 415-419.
124. Whiston, C.D. and A.J. Smith, *Double oxides containing niobium or tantalum. V. Systems containing a Group III element.* Acta Crystallographica Section B, 1978. **34**(5): p. 1454-1456.

List of Figures

List of Tables